Characterization of organic iron and cobalt ligands in the subtropical North Pacific

Jiwoon Park

A dissertation

submitted in partial fulfillment of the

requirements for the degree of

Doctor of Philosophy

University of Washington

2022

Reading Committee:

Randelle M. Bundy, Chair

Anitra E. Ingalls

Jodi N. Young

Program Authorized to Offer Degree:

Oceanography

University of Washington

Abstract

Characterization of organic iron and cobalt ligands in the subtropical North Pacific

Jiwoon Park

Chair of the Supervisory Committee:
Randelle M. Bundy
School of Oceanography

Trace metals are essential to the growth of marine organisms, but they exist in very low concentrations in the ocean, and are mostly complexed to diverse suites of organic ligands. While these metal-binding ligands directly impact metal speciation, reactivity, and bioavailability, the distributions and cycling of these ligands still remains relatively unclear. Recently, direct molecular characterization of individual ligands became possible through developments in liquid chromatography and mass spectrometry tools. My dissertation uses liquid-chromatography mass-spectrometry (LC-MS) techniques to characterize metal-binding organic ligands in seawater in order to understand how these ligands affect the biogeochemical cycles of trace metals and impact microbial community structure. I quantified and characterized siderophores, a class of strong iron-binding ligands, in the subtropical North Pacific. Combining of this data with metagenomes and metatranscriptomes analyses provided additional insight on

how different siderophores are being actively produced and consumed by distinct microbial groups. I also explored the identity of cobalt binding ligands, whose sources, sinks and chemical structures are largely unknown. Despite the widespread assumption that cobalt ligands are related to cyanocobalamin and its degradation products, it may be possible that there are additional unknown ligands that can bind cobalt. Overall, this dissertation expands the availability of organic iron- and cobalt-binding ligand data in the marine environment, and presents examples of the interplay between the distribution and speciation of trace metals and marine microbial communities.

TABLE OF CONTENTS

LIST OF FIGURES

LIST OF TABLES

ACKNOWLEDGEMENTS

This work would not have been possible without the expertise and support of many mentors, colleagues, friends and family. I cannot express enough gratitude to my advisor, Randie Bundy, whose guidance, enthusiasm, and patience carried me through the past years. She opened the door to so many amazing opportunities and experiences that have been foundational to my development as a scientist, encouraged me to go further than I thought I could go, and showed me how to be a good scientist, mentor and person. I am also deeply grateful to my committee, Anitra Ingalls, Jodi Young, Joe Resing and Brook Nunn for all their expertise, professional advice and continued encouragement. Each and all of them tirelessly reminded me that they were always on my side and that they truly believed I could get through my graduate journey. I also thank Gisela Winckler, my first mentor in oceanography and my first role model– without her I would not have become an oceanographer.

The Bundy lab members are a brilliant, wonderful group of people to work with. Thanks to Colleen Hoffman for keeping everything organized and always giving out advice, Katherine Heal for teaching me so much about the LC and staying positive and focused, Travis Mellett, Koko Kunde and Angel Ruacho for always being down to troubleshoot instruments and providing great advice. Laura Moore has been an incredible officemate that brought so much energy to the lab and cheered me up on my bad days by sharing cat photos and going on ice cream dates. I am grateful for all their knowledge and support provided at every turn.

I also thank my former advisor, Julian Sachs, and former labmates, Matthew Wolhowe and Becci Danford. Ashley Maloney's enthusiasm toward everything in science and life has always been inspiring. Tess Carlson has been an extraordinary friend, always full of bright energy and determination, and gave great pep talks.

The oceanography graduate student community is a remarkable group of people who made the graduate school experience so much better than I could have ever imagined. The wonderful group of female chemical oceanographers, Angie Boysen, Marta Wolfshorndl, Megan Duffy, Susanna Michael and Elisa Bonnin, has been a constant source of inspiration and joy. Thanks to my fellow cohorts and the oceanography community, including Claire, Theresa, Robert, Zac, Hannah D, Hannah G, Brendan, Erik, David, Ryan, Shirley, Isaiah and Sasha, for pushing me to work hard and helping me survive the stress of graduate school.

The UW Engage, especially the workshop committee, has been a really fun group to work with, and changed my attitude toward talking about and sharing my science. Thanks to my Seattle and out-of-Seattle friends for constantly cheering me on, sharing their wisdom and reminding me to take a break from work.

Finally, I am beyond grateful to my family for their unwavering support, encouragement and understanding. Yeji Park is the best sister one could ask for. Thank you for being my best friend, for sharing so many experiences together since college and continuously looking out for new adventures. Grandma, I am so lucky to have someone who would always smile at me and say the most heartwarming words. Mom and dad, thank you for always trusting in my judgment and constantly telling me I make you proud, and for always being there in times of need, joy and tears. I am only here because of you.

Chapter 1. INTRODUCTION

Microorganisms in the ocean play a crucial role in sustaining life on Earth. Even though ocean phytoplankton only make up ~ 0.2 % of primary producer biomass, they annually produce 100 billion tons of carbon, equivalent to roughly half of the global net primary productivity, and up to 70 % of the oxygen in the Earth's atmosphere (Field et al. 1998; Sekerci and Petrovskii 2015). Most of this organic carbon forms the base of the marine food web and feeds other organisms, while <10 % of it is exported out of the surface ocean (Siegel et al. 2014). A fraction of the exported carbon is respired by heterotrophic bacteria and archaea at depth into carbon dioxide and returns to the atmosphere, while the remaining fraction gets removed and remains sequestered from the atmosphere on the timescale of thousands of years (Arístegui et al. 2009). As marine microbes require nutrients other than carbon to keep up with these processes, nutrient inventories in the ocean can control the fluxes of carbon in and out of the ocean, which have important implications for the Earth's climate. In this dissertation, I focus on a subset of trace metal micronutrients that can affect marine productivity and community composition.

1.1 IMPORTANCE OF TRACE METALS AND TRACE METAL-BINDING LIGANDS IN THE OCEAN

Trace metals such as iron, cobalt, manganese, nickel, copper and zinc are essential for marine life (Sunda 1989; Morel and Price 2003; Twining and Baines 2013; Morel et al. 2014). These metals can have multiple oxidation states, which makes them able to participate in major biological processes that involve redox reactions as electron transporters. Photosynthesis, respiration, nitrate and nitrite assimilation, nitrogen fixation, chlorophyll synthesis, and

dismutation of superoxides are just a few examples of the key processes that require trace metals (Sunda 1989; Raven et al. 1999; Tortell et al. 1999; Morel and Price 2003; Wolfe-Simon et al. 2005; Twining and Baines 2013). However, most trace metals exist in nanomolar to picomolar concentrations in seawater, as they have very low solubility in oxygenated seawater and tend to precipitate out from the water columns as oxides. As these concentrations are often far below what is required for optimal phytoplankton growth, trace metals such as iron, cobalt and zinc have been repeatedly found to be limiting nutrients in many areas of the ocean, particularly the high-nutrient low-chlorophyll areas (Boyd et al. 2007; Moore et al. 2013). Consequently, these bioactive metals can significantly impact primary productivity and export, and ocean nutrient cycles (Moore et al. 2004; Morel et al. 2014).

Most trace metals in seawater are complexed to organic ligands (> 99 % for iron and copper, > 98 % for zinc and > 90 % for cobalt) (Bruland and Lohan 2003). These ligands play a key role in controlling trace metal distributions in the ocean by preventing metals from scavenging and precipitation (Johnson et al. 1997). Furthermore, different metal-binding affinity or chemical lability of these ligands also influence metal bioavailability to microorganisms (Vraspir and Butler 2009). As the importance of ligands has become widely recognized, global biogeochemical models started to include iron-binding ligands as model parameters, initially as a uniform pool across the global ocean, but more recently as an explicitly modeled dynamic pool with variable concentrations across the global ocean (Tagliabue et al. 2016). There have also been increasing efforts to account for organic ligands that complex to other bioactive metals in these models, such as cobalt and copper (Tagliabue et al. 2018; Richon and Tagliabue 2019), but these could further benefit from a better representation of ligand cycling. Improvement in these biogeochemical model performances could provide valuable insight on how future climate

changes may influence metal and carbon cycling. However, accounting for ligand cycling in models may be limited by our current knowledge on the sources, sinks and chemical identities of metal-binding ligands.

1.2 CHARACTERIZATION OF ORGANIC METAL-BINDING LIGANDS

There has been increasing efforts to understand the chemical composition of metal-binding ligands, but identifying the individual ligands that exist in low concentrations from the salt and complex dissolved organic matter matrices of seawater is a formidable task. Initial characterization of organic ligands has thus focused on a broad classification of ligands into different "classes" based on their binding affinity to metals. This was largely achieved by the application of electrochemical methods, in particular the competitive ligand exchange-adsorptive cathodic stripping voltammetry (CLE-ACSV). With this method, concentrations of natural ligands in seawater can be determined by adding known concentrations of well-characterized ligands and making them compete with natural ligands bound to individual metals (van den Berg 1989). More recently, developments in liquid chromatography and electrospray ionization mass spectrometry (ESI-MS) have allowed the isolation, separation and chemical characterization of individual metal-binding ligands (Mawji et al. 2008; Velasquez et al. 2016; Boiteau et al. 2016b; a; Bundy et al. 2018; Boiteau et al. 2019).

1.2.1 *Iron-binding ligands*

As iron is a primary limiting nutrient in many areas of the ocean (Boyd et al. 2007), iron-binding ligands have naturally received lots of attention in order to better understand the oceanic iron cycling. Over 99.9 % of dissolved iron is complexed to organic ligands, which are classified

into different classes based on their binding affinity to iron (strong ligands denoted as L_1 and weaker ligands denoted as L_2 and below) (Gledhill and van den Berg 1994; Rue and Bruland 1995; Wu and Luther 1995; Gledhill and Buck 2012; Buck et al. 2012; Abualhaija et al. 2015; Bundy et al. 2015). The highest iron-binding ligand concentrations are most often associated with maximum chlorophyll (Gledhill and Buck 2012), which suggests that these ligands are of a biological origin, but high iron-binding ligand concentrations are also found in coastal waters, river plumes and benthic boundary layers, which may also indicate terrestrial or riverine sources (Buck et al. 2007; Laglera and van den Berg 2009; Bundy et al. 2014; Boiteau et al. 2019).

Siderophores are thought to comprise a part of the strong L_1 ligand pool, as their binding strength to iron is very similar to those of L_1 ligands in natural seawater. Siderophores are low molecular weight molecules produced by bacteria and fungi to facilitate iron uptake (Neilands 1981). Production of siderophores and uptake of iron-siderophore complexes are thought to be regulated by the ferric uptake regulator (Fur) protein, which controls the transcription of iron-related genes when extracellular iron concentrations are low (Bagg and Neilands 1987). While most of the knowledge on the chemical structure and biological role of siderophores initially came from controlled laboratory cultures, recently siderophores have been directly isolated and identified from different areas of the ocean, including the subtropical North Atlantic, subtropical and tropical South Pacific, and the California Current system (Mawji et al. 2008; Velasquez et al. 2016; Boiteau et al. 2016a; Bundy et al. 2018; Boiteau et al. 2019). However, the majority of these studies focused on surface waters, and only four profiles of siderophores have been published thus far (Bundy et al. 2018; Boiteau et al. 2019).

1.2.2 *Cobalt-binding ligands*

While cobalt is also an important micronutrient utilized during photosynthesis and DNA and amino acid synthesis (Yee and Morel 1996; Allen 2012), the sources, sinks and chemical identity of cobalt-binding ligands are not as well understood as iron-binding ligands. Electrochemical analyses from different areas of the ocean show that 60-99 % of dissolved cobalt in seawater is complexed to very strong organic ligands (Ellwood and van den Berg 2001; Saito and Moffett 2001; Bown et al. 2012, p. 20; Hawco et al. 2016; Bundy et al. 2020). Similar to iron-binding ligands, these ligands may also have a biological origin, as excess cobalt-binding ligand concentrations have been found in the chlorophyll maximum (Saito and Moffett 2001). Since the binding strength of these ligands to cobalt is very similar to that of cobalamins (vitamin B_{12}) and cobalamin analogs, it has been assumed that cobalt ligands may be related to cobalamins (Ellwood and van den Berg 2001; Saito et al. 2002), but no direct characterization of the cobalt-binding ligand pool has been made to date.

1.3 CHAPTER OVERVIEW

My master's work in Chapter 4 was focused on improving our understanding of the climate system by reconstructing past hydrological records. A close examination of the relationship between hydrogen and carbon isotopes of greenhouse-grown mangrove leaf lipids and salinity suggested that in order to utilize the stable hydrogen and carbon isotopic composition of mangrove lipids (δ^2H_{lipid} and $\delta^{13}C_{lipid}$) as a paleoprecipitation proxy, future lab-based calibration efforts should further focus on the relationship between $\delta^{13}C_{lipid}$ and salinity.

My PhD work uses mass spectrometry coupled to liquid chromatography to characterize parts of the organic metal-binding ligand pool in the North Pacific to understand how ligands and

microbial communities may be interacting with each other and influence trace metal cycling. In Chapter 2, I found diverse types of siderophores in a meridional transect in the North Pacific that span across the iron-replete subtropical gyre to the relatively high-iron transition zone. Integration of metagenomes and metatranscriptomes provides a deeper insight into which microbes may be producing and utilizing siderophores for iron uptake and highlights the roles of siderophores as an important component of the iron binding ligand pool. In Chapter 3, I attempted to identify cobalt binding ligands in the same North Pacific transect. Pairing cobalt ligand data with cobalamin cellular quotas and cobalamin uptake or synthesis transcripts, I found that the cobalt ligand pool in the North Pacific surface waters consists of highly heterogeneous ligands that may not be necessarily related to cobalamin-related compounds. In summary, these chapters expand the current dataset of iron and cobalt ligands in seawater and examine the biological feedback between iron and cobalt ligand distributions and microbial communities.

Chapter 2. SIDEROPHORE PRODUCTION AND UTILIZATION BY MARINE BACTERIA IN THE NORTH PACIFIC

* This chapter is an edited version of the submitted publication: Park, J., Durham, B.P., Key, R.S., Groussman, R.D., Pinedo-Gonzalez, P., Hawco, N.J., John, S.G., Carlson, M.C.G., Lindell, D., Juranek, L.W., Ferrón, S., Ribalet, F., Armbrust, E.V., Ingalls, A.E. & Bundy, R.M. Siderophore production and utilization by microbes in the North Pacific Ocean. Submitted to Limnology and Oceanography and published as a preprint on bioRxiv (https://doi.org/10.1101/2022.02.26.482025)

2.1 ABSTRACT

Siderophores are strong iron-binding molecules produced and utilized by microbes to acquire the limiting nutrient iron (Fe) from their surroundings. Despite their importance as a component of the iron-binding ligand pool in seawater, data on the distribution of siderophores and the microbes that use them are limited. Here we measured the concentrations and types of dissolved siderophores during two cruises in April 2016 and June 2017 that transited from the iron-replete, low-macronutrient North Pacific Subtropical Gyre (NPSG) through the North Pacific Transition Zone (NPTZ) to the iron-deplete, high-macronutrient North Pacific Subarctic Frontal Zone (SAFZ). Surface siderophore concentrations in 2017 were higher in the NPTZ (4.0-13.9 pM) than the SAFZ (1.2-5.1 pM), which may be partly attributed to stimulated siderophore production by environmental factors such as dust-derived iron concentrations (up to 0.51 nM). Multiple types of siderophores were identified on both cruises, including ferrioxamines, amphibactins and iron-free forms of photoreactive siderophores, which suggest active production and use of diverse siderophores across latitude and depth. Additionally, the widespread genetic potential for siderophore biosynthesis and uptake across latitude and the variability in the

taxonomic composition of bacterial communities that transcribe putative ferrioxamine, amphibactin and salmochelin transporter genes at different latitudes suggest that particular microbes actively produce and use siderophores, altering siderophore distributions and the bioavailability of iron across the North Pacific.

2.2 INTRODUCTION

Iron (Fe) is an essential nutrient for ocean life, but due to its low solubility in seawater, it often exists in concentrations far below the levels required for sustaining phytoplankton growth in over a third of open ocean surface waters (Johnson et al. 1997; Liu and Millero 2002; Moore et al. 2013). More than 99% of the dissolved iron in the ocean is bound to organic ligands, as complexation of iron to organic ligands can increase the solubility of iron by orders of magnitude and prevent precipitation and scavenging (Gledhill and van den Berg 1994; Hunter and Boyd 2007; Gledhill and Buck 2012). In addition to increasing iron solubility, these organic ligands also affect the bioavailability of iron to phytoplankton and bacteria, playing a critical role in the ocean iron and other biogeochemical cycles (Hassler et al. 2012; Shaked et al. 2020).

Although the importance of iron-binding ligands to iron speciation and distributions in the ocean has been well recognized, the identity of these ligands, their sources and the conditions in which they are produced remain unclear (Tagliabue et al. 2017). Iron-binding ligands in seawater have been most commonly measured by competitive ligand exchange-adsorptive cathodic stripping voltammetry (CLE-ACSV) (Gledhill and van den Berg 1994; Buck et al. 2012; Bundy et al. 2015). This electrochemical method groups ligands into classes operationally defined by their binding affinity for iron, with the L_1 class being the strongest iron-binding ligands and L_2 and below being progressively weaker ligands (Hunter and Boyd 2007; Gledhill and Buck 2012;

Bundy et al. 2015). As the concentration of the L_1 ligand class is closely correlated to dissolved iron throughout the global ocean (Gledhill and Buck 2012; Buck et al. 2015, 2018), it is currently the main class of ligands represented in biogeochemical models of the iron cycle (Tagliabue et al. 2017). CLE-ACSV does not provide any information on the chemical structures of different ligands across classes, but combining these method with mass spectrometry allows direct characterization of individual ligand structures at the molecular level (Mawji et al. 2008; Boiteau et al. 2016a; Bundy et al. 2018). The similarities between the iron binding strength of L_1 class ligands and that of siderophores suggest that a part of the L_1 ligand pool may be made up of siderophores (Witter et al. 2000; Vraspir and Butler 2009).

Siderophores are low molecular weight, strong iron-binding molecules produced by microbes (Neilands 1981). More than 500 siderophores have been identified and isolated to date, mostly from bacteria and fungi cultures (Sandy and Butler 2009; Hider and Kong 2010), Siderophores are synthesized inside cells by either the non-ribosomal peptide synthetase (NRPS) pathway or the NRPS-independent siderophore (NIS) synthetase pathway and are secreted to the environment (Gulick 2017; Carroll and Moore 2018). Gram-negative bacteria use a combination of TonB-dependent outer membrane receptors (TBDT) and ATP-binding cassette (ABC) transporters to transport iron-bound siderophores through the outer membrane into the periplasm and the cytoplasm, where iron gets reduced from Fe(III) to Fe(II) and released from siderophores (Krewulak and Vogel 2008; Schalk and Guillon 2013). The ability to synthesize and transport siderophores varies widely between microbes: some microbes can produce one or more siderophores, while some cannot produce siderophores themselves but possess the siderophore uptake machinery to use exogenous siderophore-bound iron, and some cannot produce or utilize siderophores (Sandy and Butler 2009; Gledhill and Buck 2012; Kramer et al. 2020). Siderophore

production benefits its producers by decreasing the amount of available iron to other microbes that lack the ability to acquire siderophore-bound iron (Kramer et al. 2020). In addition, as siderophores can solubilize particulate iron to increase the amount of dissolved iron, they can alter the pool of bioavailable iron in the marine environment and shape the microbial community structure and composition (Kraemer et al. 2005; Kügler et al. 2020).

Multiple studies to date have measured picomolar concentrations of siderophores in surface and mesopelagic ocean waters (0-1,500 m) (Boiteau et al. 2016a, 2019; Bundy et al. 2018). In these studies, characterized iron-siderophore complexes accounted for 0.2-10% of the total dissolved iron pool, which suggests that siderophores can play a significant role in ocean iron cycling. Indeed, the prevalence of siderophore-based iron acquisition in the ocean has been demonstrated by genomic and transcriptomic surveys of marine communities. For instance, TonB-dependent outer membrane receptors involved in siderophore uptake were widespread among prokaryotes in the Global Ocean Survey (GOS) metagenomes (Hopkinson and Barbeau 2012; Toulza et al. 2012; Tang et al. 2012). In addition, siderophore uptake transcripts in the Southern Ocean were mostly derived from prokaryotes, particularly Gammaproteobactera and FCB groups, which suggest that prokaryotes may prefer the siderophore-mediated iron uptake pathway to ferrous and ferric iron transport pathways (Debeljak et al. 2019). Siderophore biosynthesis genes were detected less frequently and at a lower abundance from the GOS metagenomes than siderophore uptake genes, potentially because fewer siderophore synthesis genes were characterized and included in the search databases, or because most microbes cannot afford the expensive cost of siderophore production (Hopkinson and Barbeau 2012; Toulza et al. 2012). The combination of environmental genomic and transcriptomic surveys for siderophore biosynthesis and uptake genes can give insights into the potential for siderophore biosynthesis or

uptake, and further provide evidence for active production and cycling of siderophores in seawater. However, to our knowledge, no study to date has paired a genomics- and transcriptomics-based approach with chemical measurements of siderophore concentrations and distributions.

To examine possible chemical and biological controls of siderophore distributions, we measured dissolved siderophore concentrations across a basin-scale meridional transect at 158°W, from 23.5°N to 41.4°N in the North Pacific Ocean during two cruises in 2016 and 2017. In order to evaluate the impact of microbial activity on siderophore distribution, we searched for a comprehensive set of siderophore synthesis and uptake genes across both cruise transects, then further looked at transcription of transporter genes for three specific siderophores.

2.3 METHODS

2.3.1 *Seawater Collection*

Samples were collected during the Gradients 1 cruise (KOK1606) on the R/V *Ka'imikai-O-Kanaloa* from April 19 to May 3, 2016 and the Gradients 2 cruise (MGL1704) on the R/V *Marcus G. Langseth* from May 27 to June 13, 2017. The two cruises collected samples along 158°W, from approximately 23.5°N to 37.3°N and 25.8°N to 41.4°N respectively. Seawater samples for dissolved siderophore analyses were collected using Niskin-X bottles with external Teflon-coated springs (General Oceanics) mounted on a trace metal-clean rosette and a non-metallic line. Collection depths were pre-programmed to the autofire module (Seabird Scientific) and sample bottles were closed on the upcast while the rosette was moving through the water (~ 20-30 m min^{-1}). Niskin-X bottles were placed in a HEPA-filtered clean space on board the ship

prior to sub-sampling. Surface samples (~ 5 m) were collected from a towed trace metal-clean "fish" (Vink et al. 2000) and sample bottles were filled inside a HEPA-filtered clean space.

Sea surface temperature and salinity were measured from thermosalinograph systems aboard each research vessel. Sample collection and analysis for nitrate plus nitrite (N+N), soluble reactive phosphorus (SRP), particulate organic carbon (POC) concentrations and O_2/Ar-derived estimates of net community production (NCP) are described in Juranek et al. (2020).

Discrete samples for bacterial cell abundances measurements by flow cytometry were collected from surface water (~ 5 m depth), fixed with glutaraldehyde (0.25% final concentration) and analyzed with a BD Influx cell sorter equipped with a 488 nm laser. Data collection was triggered by forward light scatter (10% neutral density). Total bacteria counts were obtained by staining the sample with SYBR Green I (0.01% final concentrations) for 20 minutes in the dark and detecting emission at 530 nm (40 nm bandpass). *Prochlorococcus* cell counts were determined on unstained samples based on forward scatter and chlorophyll fluorescence emission at 692 nm (40 nm bandpass). Heterotrophic bacteria abundance was calculated by subtracting *Prochlorococcus* counts from the total bacteria count (Marie et al. 1999).

2.3.2 *Metagenomic and Metatranscriptomic Sampling and Processing*

During both cruises, seawater samples for metagenomes and metatranscriptomes were collected either from the flow-through system or from a CTD rosette at 15 m depth. In each instance, 6-10 liters of seawater were passed through a nitex pre-filter (200 μm mesh for Gradients 1 and 100 μm mesh for Gradients 2) followed by sequential filtration through a 3 μm and a 0.2 μm polycarbonate filters using a peristaltic pump. This collection scheme yielded two

size classes (0.2-3 µm and 3-100 or 200 µm). In this study, we focused on the 0.2-3 µm size fraction that includes "free-living" bacterial communities. Filters were frozen in liquid nitrogen and stored at -80°C until further processing.

Samples from the 0.2-3 µm size fraction were used to construct sequencing libraries. To generate quantitative read inventories, internal standards of *T. thermus* genomic DNA for metagenomes and a set of 14 synthetic internal mRNA standards for metatranscriptomes (Satinsky et al. 2013; Durham et al. 2019) that included eight standards synthesized with polyA tails to mimic eukaryotic mRNA and six without polyA tails to mimic prokaryotic mRNAs were added in known concentrations prior to nucleic acid extraction. The number of sequenced reads recovered from the internal standards was used to calculate a normalization factor for each sample as previously described, and we used only the prokaryotic mRNA standards in our analysis (Satinsky et al. 2013). DNA was extracted using phenol:chloroform following enzymatic cell lysis (Boström et al. 2004). DNA was fragmented to ~ 600 bp and used to construct Nextera DNA Flex libraries. Total RNA was extracted using the ToTALLY RNA kit (Invitrogen) for Gradients 1 samples and the Direct-zol RNA MiniPrep kit (Zymo Research) for Gradients 2 samples, and processed as described previously (Durham et al. 2019). Briefly, RNA extracts were treated with DNase, and rRNAs were removed using Illumina's Bacteria and Yeast Ribo-Zero rRNA Removal Kits. The rRNA-depleted RNA was cleaned using the Zymo RNA Clean and Concentrator Kit. Purified, depleted RNA was then sheared to ~ 225 bp fragments and used to construct TruSeq cDNA libraries according to the Illumina TruSeq® RNA Sample Preparation v2 Guide. Metagenomic and metatranscriptomic libraries were sequenced with the Illumina NovaSeq 6000 sequencing platform using the S4 flow cell with paired-end (2 × 150) chemistry.

2.3.3 *Dissolved iron analysis*

Surface seawater samples for dissolved trace metals were filtered through 0.2 µm Supor membrane filters (Pall), and the filtrates were stored in 50 mL acid-cleaned polypropylene centrifuge tubes (VWR). Samples were analyzed after off-line preconcentration onto Nobias PA1 chelating resin at pH ~ 6.5 using the seaFAST-pico system (Lagerström et al. 2013). Samples were eluted in 10% nitric acid (Optima, Fisher Scientific) and analyzed on a Thermo Fisher Element 2 High Resolution ICP-MS using the isotope dilution method (Pinedo-González et al. 2020). The accuracy of measured dissolved iron concentrations was evaluated by referencing to consensus values of a seawater reference standard (GEOTRACES GS) and are reported elsewhere (Gradoville et al. 2020; Pinedo-González et al. 2020).

2.3.4 *Dissolved siderophore sample collection and analysis*

Ten to twenty liters of 0.2 µm filtered (Acropak 200; Pall Corporation) seawater were collected from stations between 23.5°N and 37.5°N (Gradients 1) or between 29.5°N and 41.4°N (Gradients 2) from multiple depths between the surface and 400 m. The filtered seawater was pumped continuously at a flow rate of 18 mL/min through a Bond Elut column (1 g ENV, 6 mL, Agilent Technologies) that had been previously cleaned with two column volumes of pH 2 Milli-Q water and two column volumes of Milli-Q water, and activated with two column volumes of trace metal clean methanol (Fisher Scientific Optima or distilled methanol). After the sample solid phase extraction was completed, columns were washed with 12 mL of Milli-Q water and stored at -20°C for later analyses.

Prior to analysis in the laboratory, the Bond Elut columns were thawed, rinsed with two column volumes of Milli-Q water and eluted using 13 mL of optima or distilled methanol. The

eluents were dried down using a vacuum concentrator with a refrigerated vapor trap (Thermo Scientific) over 4 to 5 hours, brought up to final volumes of 500 µL using Milli-Q water and stored in 2 mL low density polyethylene vials. Multiple method blanks were prepared along with samples to ensure that the samples were not contaminated during extraction. All samples were analyzed using liquid chromatography coupled to inductively coupled plasma mass spectrometry (LC-ICP-MS) and to electrospray ionization mass spectrometry (LC-ESI-MS). For each analysis, 50 µL aliquots of each sample were spiked with 10 µL of 50 µM cyanocobalamin as an internal standard and were analyzed on a Dionex Ultimate 3000 liquid chromatography system with a polyetheretherketone (PEEK) ZORBAX-SB C18 column (4.2 x 150 mm, 3 µm, Agilent Technologies). Samples were separated using a flow rate of 50 µL/min at 30°C and a 20 minute gradient from 95% solvent A (Milli-Q water with 5 mM ammonium formate) and 5% solvent B (trace metal clean methanol with 5 mM ammonium formate) to 90% solvent B, followed by a 10 minute isocratic step of 90% solvent B, then a 5 minute gradient from 90% to 95% solvent B, an isocratic 5 minute step at 95% solvent B, and a 15 minute conditioning step at 5% B prior to injecting the next sample. The same chromatography scheme was used both for the LC-ICP-MS and the LC-ESI-MS analyses (Boiteau et al. 2016a; Bundy et al. 2018).

Samples were introduced from the LC to the ICP-MS (iCAP-RQ; Thermo Scientific) equipped with platinum sample and skimmer cones at a flow rate of 50 µL/min via a PFA-ST nebulizer (Elemental Scientific) and a spray chamber at 2.7°C. A 10% oxygen flow was added to the sample gas to prevent deposition of organic materials on the sampler and skimmer cones. Measurements were made in kinetic energy discrimination (KED) mode with a helium collision gas at a flow rate of 3.8-4.0 mL/min. ^{56}Fe peaks were identified using in-house R scripts

(Boiteau et al. 2016a; Bundy et al. 2018), and siderophore concentrations were calculated from calibration curves of ferrioxamine E (Boiteau et al. 2016a; Bundy et al. 2018).

To identify siderophores structurally, samples were further analyzed with an Orbitrap (Q-Exactive HF; Thermo Scientific) with the following instrument settings: 3.5 kV spray voltage, 320°C capillary temperature, 16 sheath gas, 3 auxiliary gas and 1 sweep gas (arbitrary units), 90°C auxiliary gas heater temperature and S-lens RF level 65. MS^1 scans were collected in full positive mode with 120,000 mass resolution, 200-2000 m/z mass range, $1e^6$ AGC target, and 100 ms maximum injection time. MS^2 scans were collected in data-dependent MS^2 (dd-MS^2) mode with 30,000 mass resolution, 1.0 m/z isolation window, $2e^4$ AGC target, 100 ms maximum injection time and 35% collision energy, and used an inclusion list containing known masses of ~ 300 siderophores. Raw data files were converted to mzXML formats using MSConvert (Proteowizard) and processed via in house R scripts using the XCMS package (Boiteau et al. 2016; Bundy et al. 2018). Cyanocobalamin peaks (m/z = 678.234) in each extracted ion chromatogram were aligned to ^{59}Co peaks in each ICP-MS chromatogram to account for differences in retention times. Siderophores were identified using exact masses of known siderophore compounds from MS^1 (± 0.005Da), then further identified by MS^2 fragmentation patterns when possible.

A confidence level was assigned to each mass feature based on the putative identification of each siderophore. The confidence levels were modelled after those used in metabolite identification (Sumner et al. 2007) (Supp. Table 1). Level 1 is the highest level of confidence, for which MS^2 spectra of our samples were matched to spectra from other publications (10 compounds). MS^2 spectra were not obtained on all samples, so we matched exact masses (± 0.005Da) and retention time (± 0.5 minutes) from samples with MS^2 data to identify compounds

in samples with no MS^2 data, and annotated those compounds as level 2 (12 compounds). Compounds that had MS^2 spectra matching in silico MS^2 spectra (CFM-ID and MetFrag) were annotated as level 3 (4 compounds) (Ruttkies et al. 2016; Djoumbou-Feunang et al. 2019). Lastly, compounds were annotated as level 4 if they were identified as a putative siderophore based on MS^1 but there was no MS^2 spectra available for comparison, or if the obtained MS^2 spectra did not agree with the in silico predicted MS^2 spectra (59 compounds).

2.3.5 *Metagenomes and Metatranscriptomes analyses*

Sequence reads from metagenomes were quality controlled using BBDuk v38.22 with the settings ktrim=r, k=23, mink=8, hdist=1, qtrim=rl, trimq=20, minlen=50, tpe, maq=10. Reads were then assembled into contigs de novo using SPAdes v3.13.1 using the --meta flag with kmer lengths of 33, 55 and 77. Metagenomes were analyzed using FeGenie, a tool that identifies potential iron metabolism related genes, with FeGenie's HMM library for siderophore biosynthesis and transport genes (Garber et al. 2020). Gene abundances in copies per liter of seawater were obtained by normalizing the sequence reads to that of the internal standard. Furthermore, taxonomy was assigned to sequences identified to be significantly similar to siderophore biosynthesis and transport gene sequences using Kaiju and the MARMICRODB database (Menzel et al. 2016; Hogle 2019).

Raw Illumina metatranscriptome data was quality controlled with trimmomatic v0.36 (Bolger et al. 2014) using the parameters MAXINFO:135:0.5, LEADING:3, TRAILING:3, MINLEN:60, and AVGQUAL:20, and matching read pairs were merged using flash v1.2.11 (Magoc and Salzberg 2011) with parameters -r 150 -f 250 -s 25. FASTQ files were converted to FASTA and translated with seqret and transeq vEMBOSS:6.6.0.0 (Rice et al. 2000) using standard genetic

code. Potential coding frames with > 40 uninterrupted amino acids were retained for further analysis.

We searched for translated reads corresponding to outer membrane transporters of three siderophores – ferrioxamine (FoxA and DesA), amphibactin (FhuA), and salmochelin (FepA and IroN). Full-length, experimentally verified protein sequences from reference genomes (Supp. Table 2) were used as queries to identify putative orthologs in translated protein sequences from marine microbial genomes and transcriptome assemblies compiled in a custom marine reference database (Coesel et al. 2021) using BLASTp v2.2.31. Genomes and transcriptomes used in this database were derived from Joint Genome Institute (JGI), National Center for Biotechnology Information (NCBI), and the Marine Microbial Eukaryote Transcriptome Sequence Project (MMETSP) (Keeling et al. 2014). A complete list is available in Coesel et al. (2021). Marine sequences retrieved from the BLASTp search were clustered using usearch (Edgar 2010) and aligned using MAFFT v7 with the E-ISN-I algorithm (Katoh and Standley, 2013). The alignment was trimmed using trimAl v1.2 using –gt .05 –resoverlap 0.5 –seqoverlap 50 options (Capella-Gutierrez et al. 2009). The trimmed alignment file was converted to PHYLIP format, and the best-fit amino acid substitution matrix, among-site rate heterogeneity model, and observed amino acid frequency were determined using ProtTest 3 software (Darriba et al. 2011). A maximum-likelihood phylogenetic reference tree was built using RAxML v8 (Stamatakis 2014), and only those sequences that clustered with experimentally verified enzymes were considered putative homologs. These phylogenetic reference trees served as scaffolds to recruit translated environmental metatranscriptomic reads. An HMM profile was constructed from each reference alignment using hmmbuild, followed by transcript identification and alignment to the reference using hmmsearch (parameters: -T 40 –incT 40) and hmmalign, respectively, with the HMMER

package v2.1 (Eddy 2011). NCBI taxonomy was assigned to each environmental sequence using pplacer v1.1.alpha19-0-g807f6f3 (Matsen et al. 2010) based on the read placement with the best maximum likelihood score to the reference tree (parameters: --keep-at-most 1 –max-pend 0.7). Read counts were normalized by recovery of internal mRNA standards to estimate transcript abundance in total transcripts per liter. Due to the high similarity between ferrioxamine, amphibactin, and ferrichrome transporter sequences (28-55%) and between salmochelin and enterobactin transporter sequences (40-92%), each group of transporter homologs was combined to construct a single reference tree (Supplementary Figure 2.1; Supplementary Table 2.1). For the combined ferrioxamine-amphibactin-ferrichrome transporters, we report sequences most closely related to the experimentally verified sequences separately from those more distantly related (Supplementary Figure 2.1; Supplementary Table 2.1). Read counts from triplicate samples were averaged at each latitude. To determine if the mean read counts for each taxonomic group were significantly different between latitudes, a one-way ANOVA and a post hoc Tukey multiple comparison test was applied.

2.4 RESULTS

2.4.1 *Environmental characteristics of the North Pacific Transition Zone and surrounding waters*

The two cruises crossed three distinct regions of the North Pacific Ocean: the North Pacific Subtropical Gyre (NPSG), the North Pacific Transition Zone (NPTZ), and the North Pacific Subarctic Frontal Zone (SAFZ) (Figure 2.1A). The NPTZ has previously been defined based on latitudinal gradients of physical and biological features (Roden 1991; Polovina et al. 2001). The southern boundary of the NPTZ, or the North Pacific subtropical front, generally corresponds to

the 34.8 isohaline and the 18°C isotherm (Roden 1991). The transition zone chlorophyll front (TZCF) is a dynamic feature between the NPSG and the subarctic gyre, and is operationally defined by surface chlorophyll-*a* concentrations of 0.2 mg/m^3 (Polovina et al. 2001). The TZCF does not always coincide with the physical definition of the NPTZ, as it migrates seasonally by ~10 degrees in latitude, due to strong seasonal gradients in nutrients, light and shifts in phytoplankton composition (Follett et al. 2021).

In both cruise transects, we observed decreases in sea surface temperature and salinity as we transited northward (Figure 2.1B-C). The second derivative of surface salinity was used to determine the position of the North Pacific subtropical front, which was 30.7°N in April 2016 and 32.8°N in June 2017 (Gradoville et al. 2020; Follett et al. 2021). In addition, the subarctic salinity front was only crossed in June 2017, and this front was located at 38.0°N based on the 33.8 isohaline (Roden 1991; Gradoville et al. 2020). These frontal locations will be used in the remainder of this work when discussing the NPSG, the NPTZ, and the SAFZ (Figure 2.1).

Strong latitudinal trends in surface nutrient inventories were observed in both cruises, with N+N and SRP concentrations both increasing across the NPSG to NPTZ or SAFZ by up to tenfold (Juranek et al. 2020) (Figure 2.1D-E). Along with changes in nutrients, latitudinal changes in productivity and biomass were also observed. Both particulate organic carbon (POC) and O_2/Ar-derived net community production (NCP) sharply increased across the TZCF, which was located at 33.0°N in April 2016 and 36.2°N in June 2017, and reached a maximum at the northern-most stations (Juranek et al. 2020) (Figure 2.1F-G). Heterotrophic bacterial cell abundances at the surface also increased with latitude by tenfold across both transects (H).

Surface dissolved iron concentrations showed different latitudinal trends between the two years (Figure 2.2A). In April 2016, surface dissolved iron concentrations were highest in the

NPSG (0.13-0.31 nM) and generally decreased with increasing latitude, whereas in June 2017, surface dissolved iron concentrations were highest in the NPTZ (0.20-0.51 nM) (Pinedo-González et al. 2020). The peak in dissolved iron concentrations at 35°N in June 2017 was interpreted to be due to atmospheric deposition of anthropogenic aerosols from Asia, based on the isotopic composition of dissolved iron and lead (Pinedo-González et al. 2020). The difference in iron distributions between the two cruises was likely caused by the seasonal supply of aerosol-derived iron to the North Pacific Ocean, as depth-averaged satellite observations of aerosol optical depth (AOD) show higher aerosol concentrations over the region of our cruise transect in spring to early summer (March-July; Supplementary Figure 2.2).

2.4.2 *Siderophore distributions in the North Pacific*

Dissolved siderophore concentrations in surface waters (0-25 m) differed between the April 2016 and June 2017 transects (Figure 2.2B). In April 2016, surface siderophore concentrations (1.4 ± 1.3 pM) were relatively uniform across the transect, with no statistically significant difference between the NPSG (1.4 ± 1.0 pM) and the NPTZ (1.4 ± 1.7 pM) (Mann-Whitney U test, $p = 1$). In contrast, surface siderophore concentrations in June 2017 were higher and more variable than in 2016, with average concentrations of 14.3 ± 25.9 pM. In addition, siderophore concentrations in the NPTZ (9.3 ± 4.1 pM) were higher than concentrations in the SAFZ (3.0 ± 1.7 pM) (Mann-Whitney U test, $p = 0.06$).

Siderophore concentrations below the surface (25-400 m) were not significantly different from surface concentrations in either 2016 or 2017 (Mann-Whitney U test, p = 0.46 and 0.11 respectively), nor significantly different between the NPSG (1.4 ± 1.6 pM) than in the NPTZ (0.7

± 0.7 pM) in April 2016 or between the NPTZ (12.8 ± 23.5 pM) and SAFZ (3.3 ± 3.1 pM) in June 2017 (Mann-Whitney U test, $p = 0.35$ and 0.13) (Figure 2.3B).

2.4.3 *Siderophore identities in the North Pacific*

Among the siderophores we identified with high confidence (levels 1-3) in April 2016 (9 siderophores) and June 2017 (11 siderophores), ferrioxamines were the most common type of siderophore detected and were found in samples from Gradients 1 (Figure 2.4) and Gradients 2 (Figure 2.5). Ferrioxamine E and G1 were detected in both years (Figure 2.4A-B, Figure 2.5A-B), whereas ferrioxamine B was only detected in April 2016 (Figure 2.4C). Most ferrioxamines were complexed to iron, however in 2 out of 37 ferrioxamine identifications, both iron-bound and apo- (iron-free) ferrioxamine E were detected, with concentrations of apo-ferrioxamine E approximately a tenth of iron-bound ferrioxamine E. Different types of ferrioxamines were found across all depths in both the NPSG and the NPTZ, but not in the SAFZ. In addition, multiple types of ferrioxamines were often detected concurrently in a single location. We also detected a suite of amphibactins (D, E, H, T) complexed to iron in June 2017, and these were mostly found in the NPSG and the southern part of the NPTZ (~35°N), except amphibactin E, which was found across the full range of NPTZ (Figure 2.5C-F).

In addition to ferrioxamines and amphibactins, we also detected several photoreactive siderophores in their iron-free forms, based on their MS^1 and MS^2 fragmentation data with confidence levels 1-3. Apo forms of synechobactin c12 and c13 were detected consistently across the cruise transects in April 2016 and June 2017, respectively (Figure 2.4E, Figure 2.5H), and were mostly confined to surface waters (0-150 m). Iron-free petrobactin, another photolabile siderophore, was detected in April 2016, at depths between 100-400 m (Figure 2.4D). North of

the subarctic salinity front in June 2017, we also found apo forms of schizokinen (Figure 2.5G), another siderophore that may be photoreactive given the α-hydroxy-carboxylic acid group in its structure, although its photoreactivity has not yet been confirmed (Årstøl and Hohmann-Marriott 2019).

In addition, we detected multiple siderophores not previously detected in the marine environment. Apo forms of heterobactin B were found in north of the subarctic salinity front in 2017 (Figure 2.5I). We also found a suite of siderophores known to be produced by marine or terrestrial fungi, including coprogen, 2-N-methylcoprogen and rhizoferrin, sporadically distributed across the transect.

2.4.4 *Connecting genomes and transcriptomes to siderophore measurements*

We used FeGenie (Garber et al. 2020) to search for siderophore transport and synthesis genes in metagenomic datasets collected from surface waters in both cruises. Siderophore transport genes were detected at abundances of 0.80 ± 0.37 million copies L^{-1} and 1.74 ± 1.00 million copies L^{-1} from the 2016 and 2017 cruises, respectively (Figure 2.6A). Out of 82 gene families that are classified as siderophore transport-related in the FeGenie library, we identified 26 gene families from both transects. The ExbB and ExbD gene families (part of the TonB-ExbB-ExbD siderophore transport system) were the most abundant (Figure 2.6B). Siderophore biosynthesis genes were approximately an order of magnitude less abundant than the siderophore transporter genes (0.11 ± 0.06 and 0.21 ± 0.14 million copies L^{-1} for Gradients 1 and 2, respectively) (Figure 2.6A). Out of 95 siderophore synthesis gene families included in the FeGenie library, 35 siderophore synthesis gene families belonging to 7 biosynthetic pathways were identified from the two cruises, with VabA, VabE and VabF families most frequently detected (Figure 2.6C).

While both siderophore synthesis and transport gene abundances increased with latitude ($p < 0.05$, R^2 ranging from 0.15 to 0.24), no individual siderophore transport or synthesis gene families were found to be clustered at specific latitudes (Supplementary Figure 2.5). Siderophore transport genes primarily came from Gammaproteobacteria (47%), Alphaproteobacteria (20%) and Flavobacteria (10%) while siderophore synthesis genes mostly came from Gammaproteobacteria (50%) and Alphaproteobacteria (20%) (Supplementary Table 2.3).

To examine which taxa may be actively cycling siderophores along the cruise transects, we analyzed the transcript abudances for homologs of three outer membrane siderophore transporters – ferrioxamine and amphibactin (foxA, desA, fhuA) and salmochelin (fepA, iroN). These outer membrane transporters were chosen as these compounds were detected during both cruises, and outer membrane transporters for these siderophores have been characterized in multiple gammaproteobacterial species. We note that transporter homologs identified in marine microbial reference organisms for ferrioxamine, amphibactin, and ferrichrome, or for salmochelin and enterobactin, could not be distinguished from one another due to their high sequence similarity (Supplementary Figure 2.1; Supplementary Table 2.1). Therefore, here we report a combined transcript abundance for the transporter homologs, though we also separated transcript inventories for the ferrioxamine-amphibactin-ferrichrome transporter signal based on phylogeny with experimentally verified sequences (Supplementary Figure 2.3).

The siderophore transporter homologs were transcribed by taxa belonging predominantly to Alpha- and Gamma-proteobacteria (Figure 2.6B). From both cruises, the alphaproteobacterial Roseobacter group (10-13 %) and gammaproteobacterial order Vibrionales (20-30 %) contributed most to the total expression of ferrioxamine- amphibactin-ferrichrome transporter transcripts. Mean transcript abundances of ferrioxamine-amphibactin-ferrichrome for transcript

homologs differed significantly (one-way ANOVA and post hoc Tukey test) between Roseobacter at 36.6°N in 2016 and Altermonadales at 29.6°N in 2017 and other latitudes (Figure 2.6B) ($p < 0.01$). The gammaproteobacterial order Oceanospiralles (29-100 %) was the major contributor to total salmochelin-enterobactin transporter transcript abundances (Figure 2.6B).

2.5 DISCUSSION

2.5.1 *Siderophore distributions in the North Pacific*

Our dataset greatly expands currently available measurements of dissolved siderophore in the ocean, as previous works have been confined to few depth profiles or have focused on surface waters. We found that dissolved siderophores were widely distributed throughout the North Pacific, both in surface waters and throughout the upper mesopelagic (down to 400m), with concentrations comparable to those from earlier studies (0.3-20 pM) (Boiteau et al. 2016a; Bundy et al. 2018; Boiteau et al. 2019). Two data points at 29.8°N, 16.5 m depth and 37°N, 100 m depth had unusually high concentrations (95.2 pM and 77.7 pM respectively). As all of our dissolved siderophore concentrations are likely representative of a snapshot in time and space, we may have sampled a water mass with a cluster of siderophore-producing microbes or with recently accumulated siderophores from cell death. Excluding these two points, dissolved siderophores accounted for 2.4 ± 5.4 % (or 0-30%) of the total dissolved iron pool across the North Pacific, suggesting that siderophores are an important component of the iron-binding ligand pool.

Elevated surface siderophore concentrations in the NPTZ in June 2017 may have been caused by higher siderophore production in this area. While a direct correlation between surface siderophore concentrations and heterotrophic bacteria abundance has been observed previously

(Mawji et al. 2008), we did not find a strong correlation between surface siderophore concentrations and phytoplankton or bacterial biomass (including POC and heterotrophic bacteria cell abundances) or NCP (Figure 2.1F-H, Figure 2.2B). However, high siderophore concentrations in the NPTZ in June 2017 coincided with a large input of anthropogenic dust to this region (Pinedo-González et al. 2020), and it may be that this external dust input triggered the observed siderophore production. While only a small fraction of dust deposited in the ocean dissolves (approximately 2% but highly variable; Baker and Croot 2010), siderophores can significantly increase the solubility of iron-bearing minerals in dust, such as iron oxides and clay minerals, so that Fe(III) from minerals are released and become available for microbial uptake (Kraemer et al. 2005; Parrello et al. 2016). A previous study in the Mediterranean Sea found a positive relationship between the fraction of iron released from dust particles and iron-binding ligand concentrations, with highest dust-derived iron and ligand concentrations in May and June and relative to other months (Wagener et al. 2008). Transient supply of excess iron can result in rapid production and release of siderophores over timescales of days, in order to relieve bacteria from the metabolically costly process of producing siderophores under iron stress (Adly et al. 2015). Therefore, high aeolian dust supply to the North Pacific may have stimulated the microbial communities to increase siderophore production to mobilize and opportunistically take up iron. However, since the dissolved siderophore pool size depends both on siderophore production and release and on siderophore losses through uptake and degradation, different siderophore loss terms across our study sites are likely also contributing to the observed siderophore concentrations. Estimates of the total siderophore pool size (including the particulate intracellular siderophore pool) or metabolic fluxes of siderophore secretion and uptake are

necessary to fully understand how the observed siderophore distribution patterns are being shaped by microbes.

To explore possible environmental drivers of siderophore distributions, including dissolved iron distributions, we also performed a logistic regression analysis using multiple environmental variables to see if any of the variables could successfully predict siderophore distribution. The regression results suggested that latitude was the most effective predictor of siderophore presence, which suggests that siderophore distributions are likely controlled by a combination of physical, chemical and biological factors (see Supplemental Information).

Siderophores were also detected below the surface ocean from both years, despite decreased heterotrophic bacterial abundances and increased dissolved iron concentrations with depth (Supplementary Figure 2.4; Figure 2.3A). In the upper mesopelagic waters (150-400m), siderophores make up 0.7 ± 0.8 % (or 0-3%) of the total dissolved iron pool. However, previous work found that heterotrophic bacteria from 150 m depth produced siderophores upon addition of *in-situ* sinking particles, suggesting that bacteria are using iron in the sinking particles during regeneration by actively producing and cycling siderophores below the euphotic zone (Bundy et al. 2018). Therefore, while the dissolved siderophore pool size is smaller in the upper mesopelagic relative to the surface waters by up to an order of magnitude, heterotrophic bacteria at depth may be more actively cycling siderophores.

2.5.2 *Siderophore identities in the North Pacific*

Overall, we observed a wide variety of siderophores with little compositional overlap between the cruises. Ferrioxamines – one of the most commonly detected siderophores in seawater to date – were the only siderophores that were detected on both cruises and in both the

NPSG and NPTZ, regions with relatively high iron compared to the SAFZ (Figure 2.4A-C, Figure 2.5A-B). These observations generally agree with previously known distributions of ferrioxamines in iron-replete waters, such as coastal upwelling systems in Southern California and Peru, subtropical North Pacific, and the mid-latitude North Atlantic (Mawji et al. 2008; Boiteau et al. 2016a, 2019). The abundances of ferrioxamines in iron-rich waters have been attributed to their extremely strong affinities to iron, which allows bacteria that can utilize ferrioxamines to efficiently compete for iron from dust or sedimentary sources (Mawji et al. 2008; Bundy et al. 2018; Boiteau et al. 2019).

Amphibactins are hydroxamate siderophores with amphiphilic tails that are also frequently detected in seawater, and were found in the NPSG and the southern part of the NPTZ (~35°N) in June 2017 (Figure 2.5C-F). Earlier studies detected amphibactins mostly in iron-limited waters such as the eastern tropical Pacific and offshore of the California Current System (Boiteau et al. 2016a, 2019). In particular, Boiteau et al. (2016a) observed a marked shift from ferrioxamines in the high iron coastal region to amphibactins in the equatorial Pacific HNLC and hypothesized that amphiphilic siderophores, which can partition into the cell membrane, were favored in the HNLC to minimize diffusive losses of the siderophore in this iron-limited region. However, as amphibactins have also been observed in the NPSG (Bundy et al. 2018), their distributions may be driven not only by dissolved iron concentrations, but also by the distribution of various amphibactin-producing and consuming bacterial taxa, including many strains of *Vibrio,* the hydrocarbon-degrading *Alcanivorax* and nitrogen-fixing *Azotobacter* (Martinez et al. 2003; Kem et al. 2014; Zhang et al. 2019).

In addition to iron-bound ferrioxamines and amphibactins, we detected and identified several photoreactive siderophores in the iron-free form. These siderophores are not routinely detected

due to a previous focus on iron-bound compounds. Iron-free forms of synechobactin and schizokinen were found primarily in surface waters (0-200 m) (Figure 2.4E, Figure 2.5G-H). As known producers of synechobactin and schizokinen include *Synechococcus* and *Anabaena* species, and as iron-synechobactin complexes can break down within a few hours when exposed to natural sunlight (Årstøl and Hohmann-Marriott 2019), the presence of synechobactins and schizokinen in surface waters implies active production of photoreactive siderophores in the surface ocean. In contrast, the iron-free form of petrobactin was only detected below the surface ocean (100-400 m). The absence of iron-free petrobactin in surface waters may be due to photooxidation of the catecholate moieties on petrobactin (opposed to light-resistant hydroxamate moieties on synechobactin and schizokinen) (Barbeau et al. 2003). Photoreactive siderophores have important implications for iron bioavailability, as photolysis of iron-siderophore complexes results in the reduction of Fe(III) to Fe(II), which in turn may become available for marine organisms that cannot take up iron bound to siderophores (Barbeau et al. 2003). Thus, further exploration of photoactive siderophores, especially in the surface ocean, may reveal their importance to marine carbon and iron cycling.

We also putatively identified heterobactin B and some fungi-derived siderophores, but much less is known about the production of these compounds. To date, heterobactins have been shown to be produced by several strains of *Rhodococcus* (Carrano et al. 2001), a genus of gram positive bacteria related to *Mycobacterium*, although little is known about the genetically diverse *Rhodococcus* in the marine environment. Siderophore production by marine fungi has also not been well-documented. Siderophores produced by fungi characterized to date are mostly hydroxamate siderophores (Holinsworth and Martin 2009). Multiple strains of Zygomecetes have been shown to produce rhizoferrin, a carboxylate siderophore (Thieken and Winkelmann

1992). Marine fungi appear to produce higher concentrations of siderophores than their terrestrial counterparts (Baakza et al. 2004), however the importance of these siderophores in oceanic iron cycling remains unclear.

Overall, we observed high variability in the types of siderophores detected between the two cruises, with the exception of ferrioxamines. Differences in siderophore composition between the two cruises may reflect the fast turnover of siderophores, as previous incubation studies suggest that siderophore production can change on daily or weekly timescales (Mohamed and Gledhill 2017; Bundy et al. 2018). Considering the large compositional difference between the two cruises, it is interesting that the suite of ferrioxamines were identified from both cruises. It may be possible that the current siderophore analysis method may be preferentially extracting and isolating ferrioxamines, especially as ferrioxamines are ubiquitously detected from earlier studies (Boiteau et al. 2016a; Bundy et al. 2018; Boiteau et al. 2019). It may be also possible that ferrioxamines are more commonly observed because they are more common siderophores that can be produced and used by a much wider variety of microbes than other siderophores.

2.5.3 *Connecting genomes and transcriptomes to siderophore distributions*

Our dissolved siderophore data provides information about which molecules exist in the water column at the time of our sampling. However, these snapshots of siderophore distributions alone may not reflect whether *in situ* microbial communities are capable of siderophore production and uptake. To gain further insight into the interactions between the dissolved siderophore pool and microbial activity, we used environmental metagenomes to get a broad overview of the genetic potential for siderophore biosynthesis in surface communities across latitudes, then further focus specifically on transcripts of select iron-siderophore complex

transporters to determine whether siderophore transporters are expressed by the *in situ* community.

Siderophore transport and biosynthesis potential was widely represented across the transects. Siderophore transport genes were roughly ten-fold more abundant than biosynthesis genes (Figure 2.6A), consistent with the results of previous marine metagenome analyses (Hopkinson and Barbeau 2012; Toulza et al. 2012). As siderophore production is a metabolically expensive process, the scarcity of siderophore biosynthesis genes relative to siderophore transporter genes might be an example of the Black Queen Hypothesis, in which evolutionary selection may have caused most microbes to lose the ability to synthesize siderophores, but left a small subset of the microbial community that retained the ability to produce siderophores and a larger subset that retained the ability to take up siderophore-bound iron (Morris et al. 2012; Mas et al. 2016).

Both siderophore synthesis and transport genes were highly conserved across our study transects (Figure 2.6A). Earlier studies also found siderophore biosynthesis genes and Ton-B dependent outer membrane transporters targeting siderophores as substrates were globally common in open ocean datasets (Tang et al. 2012; Garber et al. 2020). Both siderophore synthesis and transport gene abundances showed significant correlations with latitude across the transects (Figure 2.6A), but changes in heterotrophic bacterial abundances, which also increased with latitude (Figure 2.1H), might only account for about two-thirds of this relationship. This may suggest that there were slight enrichments of siderophore synthesis and transcript gene abundances at higher latitudes.

ExbB and ExbD families were most frequently found among the siderophore transport gene families (Figure 2.6B). This may reflect the prevalence of TonB-ExbB-ExbD families in siderophore-mediated iron uptake systems. Siderophore uptake systems are typically comprised

of outer membrane receptors that recognizes siderophores, and periplasmic binding proteins and inner membrane proteins that provide the energy to import siderophore complexes into the periplasm (Moeck and Coulton 2002; Noinaj et al. 2010). Unlike the outer membrane receptors, which only recognize certain siderophores and are highly variable, the inner membrane proteins are much more general, and are mostly related to the TonB-ExbB-ExbD family (Moeck and Coulton 2002; Noinaj et al. 2010).

Among the siderophore synthesis gene families, VabA, VabE and VabF families were most commonly detected (Figure 2.6C). Vab genes were initially identified to mediate biosynthesis of vanchrobactin in *Vibrio anguillarum*, but these genes were also found to be highly homologous to multiple nonribosomal peptide synthases (NRPS) from other species (Balado et al. 2006). Therefore, the abundance of these gene families in our data do not necessarily suggest the ubiquity of vanchrobactin biosynthesis pathway in particular, but rather represent the presence of multiple NRPS siderophore biosynthesis pathways.

Both siderophore transport- and synthesis-related genes were mostly found in Gammaproteobacteria and Alphaproteobacteria (Supplementary Table 2.3), consistent with findings from a previous study that most siderophore transporters in the GOS metagenome dataset came from Gammaproteobacteria (63%) and Alphaproteobacteria (31%) (Tang et al. 2012). While both siderophore synthesis and transport-related genes were derived from the same major microbial groups, a few taxa such as *Synechococcus* and *Brevundimonas* were only found in siderophore transport-related genes (1-3 %) but not in siderophore synthesis-related genes (Supplementary Table 2.3). These taxa may be “cheaters” who cannot produce siderophores but have specific receptors to access exogenous siderophores (Kramer et al. 2020), and additional

investigation into their individual genomes may further reveal how these microbes may be competing for iron by exploiting siderophores within the community.

As the environmental metagenomes suggests that siderophore-mediated iron uptake may be a widespread strategy in the North Pacific, we examined transcript abundances of siderophore transporter homologs as a means to detect active uptake of siderophores identified from our samples. We focused on the outer membrane transporters for ferrioxamine, amphibactin, and salmochelin rather than the biosynthesis genes for these siderophores, as the latter genes have not yet been fully characterized.

Putative transporter homologs of these siderophores were predominantly transcribed by Gammaproteobacteria (Figure 2.6B), in accordance with the metagenome analysis that indicated Gammaproteobacteria carried the majority of siderophore transport genes. Earlier studies also repeatedly found members of Gammaproteobacteria to possess a wide range of siderophore transporters relative to other bacterial groups (Hopkinson and Barbeau 2012; Tang et al. 2012; Debeljak et al. 2019). We expected to find amphibactin and ferrioxamine transporter genes to be transcribed by Gammaproteobacteria, as amphibactins and ferrioxamines are currently known to be produced by multiple gammaproteobacterial taxa, including *Vibrio*, *Alcanivorax*, *Azotobacter*, and Actinobacteria (Martinez et al. 2003; Kem et al. 2014; Wang et al. 2014; Zhang et al. 2019). Interestingly, we also detected ferrioxamine-amphibactin-ferrichrome transporter homologs in Alphaproteobacteria reference genomes (Supplementary Figure 2.1) and detected expression of these homologs in the metatranscriptomes (Figure 2.6B). No studies to date indicate ferrioxamine and amphibactins can be synthesized or utilized by taxa other than Gammaproteobacteria, in part because they have been the focus of laboratory studies (Hopkinson and Barbeau 2012). However, multiple Rhodobacterales species, including Rhodobacter,

Roseovirus, Sulfitobacter and Oceanicola, have genes to transport ferrichrome, a hydroxamate-type siderophore similar to ferrioxamine and amphibactin (Rodionov et al. 2006; Hider and Kong 2010). The high protein sequence similarity (28-55%) between ferrioxamine, amphibactin and ferrichrome transporters makes it difficult to distinguish them from one another. Thus, some of the transcripts recruited by our reference tree may be ferrichrome uptake transporters, rather than ferrioxamine or amphibactin transporters. Although we did not detect ferrichrome from seawater, it is possible that the ferrichrome pool has a rapid turnover and its concentration was too low to be detected. Additional studies are required to discern the specific function(s) of these transporter homologs.

Ferrioxamine and amphibactin transporter transcript inventories from Vibrionales were generally more abundant at northern stations (Figure 2.6B, Supplementary Figure 2.3). Vibrionales are copiotrophic bacteria that are usually present in low abundance, but can quickly grow with additional nutrient pulses from bloom events (Gilbert et al. 2012; Westrich et al. 2016). Multiple species of *Vibrio* can produce and take up amphibactin, and at least one species of Vibrio is capable of exogenous ferrioxamine uptake (Gauglitz et al. 2021). Higher ferrioxamine and amphibactin transporter transcript abundances at higher latitudes by Vibrionales may reflect higher abundances of Vibrionales or increased induction of siderophore-mediated iron uptake pathways in this environment.

Ferrioxamine and amphibactin transporter transcripts from Altermonadales at 29.6°N in 2017 were more abundant relative to other latitudes (Figure 2.6B). Ferrioxamine transporter transcripts may be produced by taxa such as Pseudoalteromonas and Alteromonas, which are able to assimilate ferrioxamine-bound iron (Armstrong et al. 2004). However, it is currently unclear whether high transcript abundance at 29.6°N was caused by significant differences in

transcription rates or a more abundant Altermonadales population because we cannot normalize the transcript abundances to microbial biomass.

While ferrioxamine and amphibactin transporter transcripts were produced by multiple Gammaproteobacterial and possibly Alphaproteobacterial taxa, transcript homologs of the salmochelin-enterobactin transporter were predominantly detected in the Gammaproteobacterial lineage Oceanospiralles. Salmochelin is a C-glycosylated derivative of enterobactin, and both salmochelin and enterobactin are known to be produced by the Enterobacterales, including *Escherichia coli*, *Salmonella* and *Klebsiella* (Hantke et al. 2003; Müller et al. 2009). While iroN and fepA genes are often annotated as salmochelin and enterobactin transporter genes respectively, both receptors can transport both siderophores (Watts et al. 2012), which makes discerning these transport functions from each other not possible. Our observation that salmochelin-enterobactin transporter homologs are restricted primarily to Oceanospiralles, as well as the low abundance of associated transcripts, suggests that salmochelin or enterobactin may be utilized by a smaller subset of microbes than ferrioxamines or amphibactins. Given salmochelin and enterobactin uptake is limited to fewer microbes compared to ferrioxamine and amphibactin uptake, their production may also be low, considering the high metabolic cost of siderophore production. If so, this would result in much lower concentrations of salmochelin and enterobactin in the ocean than ferrioxamine and amphibactin, which may partly explain why we did not find enterobactin in this study (although we putatively identified salmochelin with low confidence). Future characterization of salmochelin and enterobactin biosynthesis pathways may help us address this hypothesis by allowing the analysis of transcripts involved in salmochelin and enterobactin biosynthesis in the environment. Nevertheless, changes in the taxonomic composition of microbial groups that transcribe siderophore transporters suggest that several

important bacterial taxa can compete for iron at different latitudes, perhaps contributing to niche differentiation in taxa that actively take up siderophore-bound iron.

2.6 CONCLUSIONS

The widespread presence of siderophores across a large range in latitude and depth in the North Pacific highlights the ubiquitous use of siderophores in oceanic iron cycling. Siderophores make up 2.4 ± 5.4 % (or 0-30%) of the total dissolved iron pool in our study sites. Within this pool, a wide variety of siderophores were identified, including ferrioxamines and amphibactins – the two most commonly identified siderophores in the ocean thus far – as well as putative photoreactive and fungal siderophores. Siderophore distribution patterns were not directly correlated to any single environmental parameter we measured during the two cruises, such as microbial biomass, dissolved iron or the genetic potential of siderophore production and uptake, but were rather shaped by an interplay of multiple factors, particularly microbial production and uptake. For instance, ferrioxamine, amphibactin and salmochelin were actively used by distinct microbial groups within Gammaproteobacteria and potentially Alphaproteobacteria at different latitudes. Altogether, these results suggest that diverse microbial taxa are primarily driving the patterns of siderophore distributions. While our measurements represent a snapshot of siderophore concentrations at the time of our sampling, a time-series of repeated dissolved siderophore profiles or intracellular siderophore secretion and uptake rate measurements may provide additional insight on the timescale of siderophore production, uptake and recycling by microbes, and will provide key insights into how microbes regulate iron availability in the open ocean.

2.7 ACKNOWLEDGEMENTS

This work was supported by the Simons Foundation (426570 to R.M.B, S.G.J., E.V.A., D.L., L.J. and A.E.I.; 823165 to B.P.D.). We thank the SCOPE-Gradients team for assisting with sample collection, sharing data and providing helpful feedback that improved this work. We thank L. Carlson and K. Heal for help with data acquisition on the Orbitrap, T. Ugrai for technical support on the ICP-MS, L. Pnueli and M. Peleg for their contributions to metagenome sample processing and sequence analysis, S. Curless and R. Foreman for nutrient analysis, J. McMillan, K. Cain and A. Hynes for helping collecting and processing flow cytometry samples, D. Karl and A. White for constructive comments on the manuscript, and the captain and crew of the R/V Marcus G. Langseth and R/V Ka'imikai-O-Kanaloa.

2.8 FIGURES AND TABLES

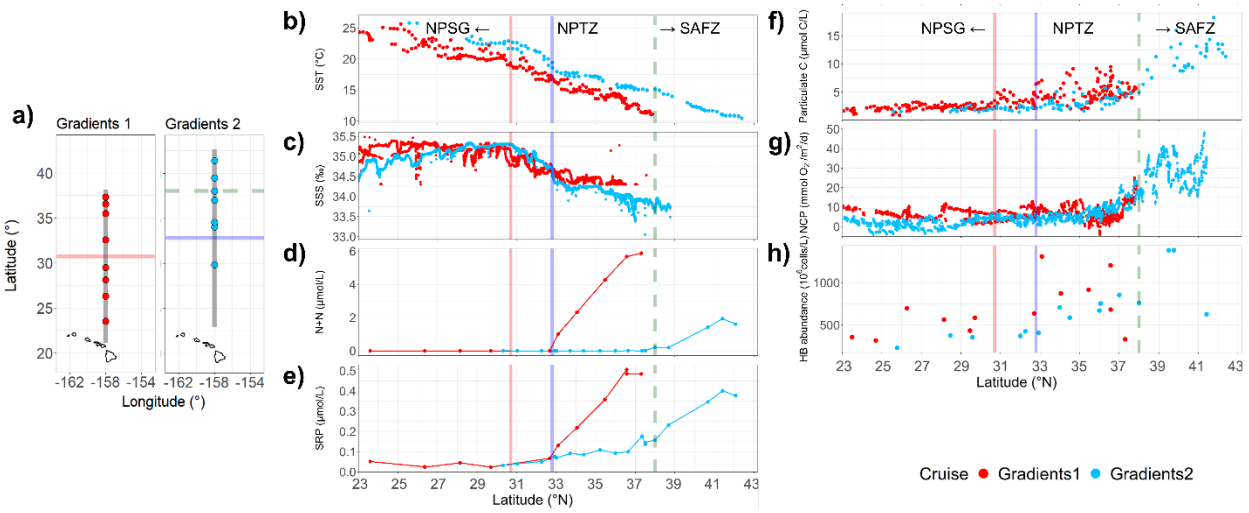

Figure 2.1 Physical, chemical and biological properties measured along the two cruise transects. A) Transects of Gradients 1 (red) and 2 (blue) cruises, B) Sea surface temperature (SST), C) sea surface salinity (SSS), D) nitrate and nitrite (N+N) concentrations, E) soluble reactive phosphorus (SRP) concentrations, F) particulate organic carbon concentrations, G) O_2/Ar-derived estimates of net community production (NCP) and H) heterotrophic bacterial abundances from Gradients 1 (red) and 2 (blue) cruises. Vertical red and blue solid lines indicate location of subtropical fronts from Gradients 1 and 2 cruises respectively; green dashed line indicates location of the subarctic front from Gradients 2.

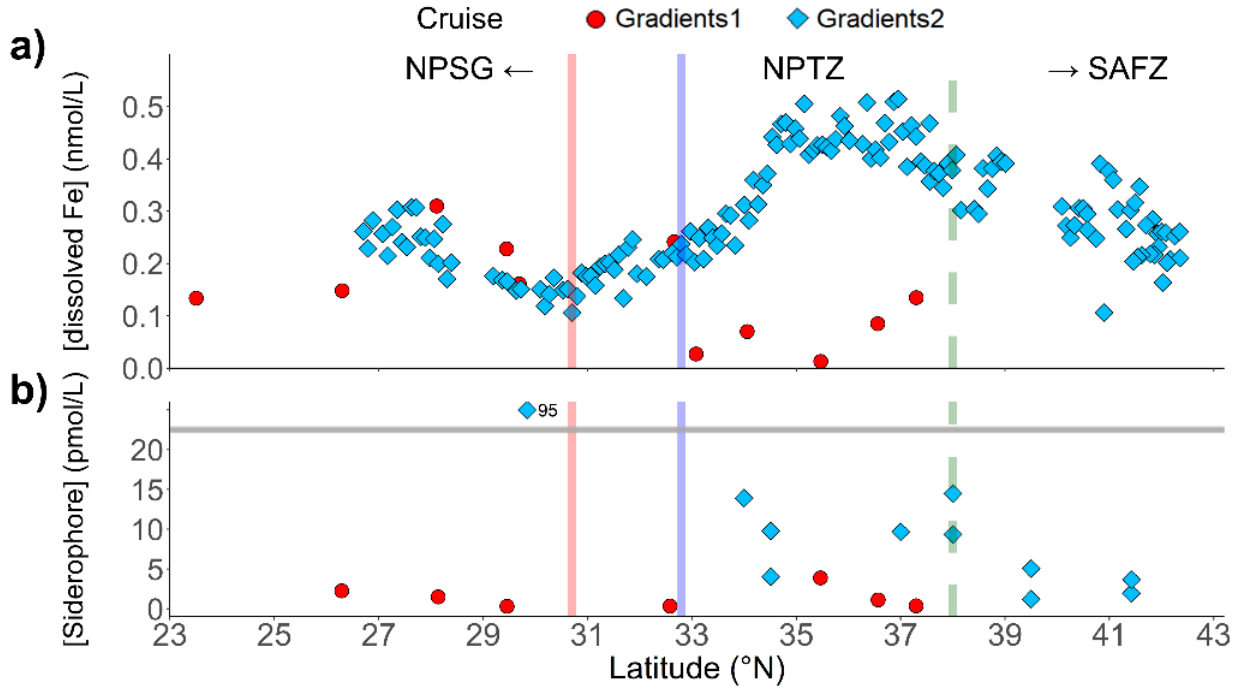

Figure 2.2 Dissolved iron and siderophore concentrations in surface waters along the two cruise transects.

A) Dissolved iron concentrations in surface waters collected with a trace metal clean towfish from Gradients 1 (red) and Gradients 2 (blue). B) Siderophore concentrations in surface waters (0-25 m) from Gradients 1 (red) and Gradients 2 (blue). One data point from Gradients 2 had siderophore concentrations outside the y-axis range of the plot (above the horizontal gray y-axis break line), and its concentrations is noted at the right of the data point. Vertical red and blue solid lines indicate location of subtropical fronts from Gradients 1 and 2 cruises respectively; green dashed line indicates location of the subarctic front from Gradients 2.

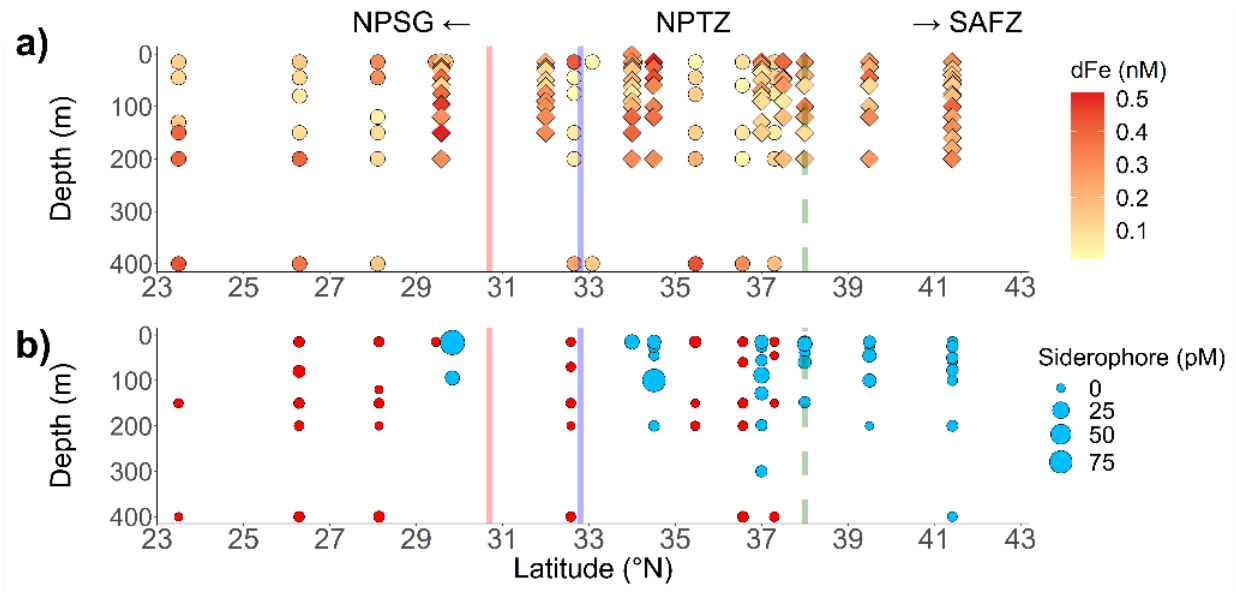

Figure 2.3 Depth profiles of dissolved iron and siderophore concentrations along the two cruise transects.

A) Depth profiles of dissolved iron concentrations from Gradients 1 (circles) and Gradients 2 (diamonds) across 0-400 m from CTD casts. B) Depth profiles of dissolved siderophore concentrations from Gradients 1 (red) and Gradients 2 (blue) across 0-400 m. Point sizes are proportional to siderophore concentrations. Vertical red and blue solid lines indicate location of subtropical fronts from Gradients 1 and 2 cruises respectively; green dashed line indicates the location of the subarctic front from Gradients 2.

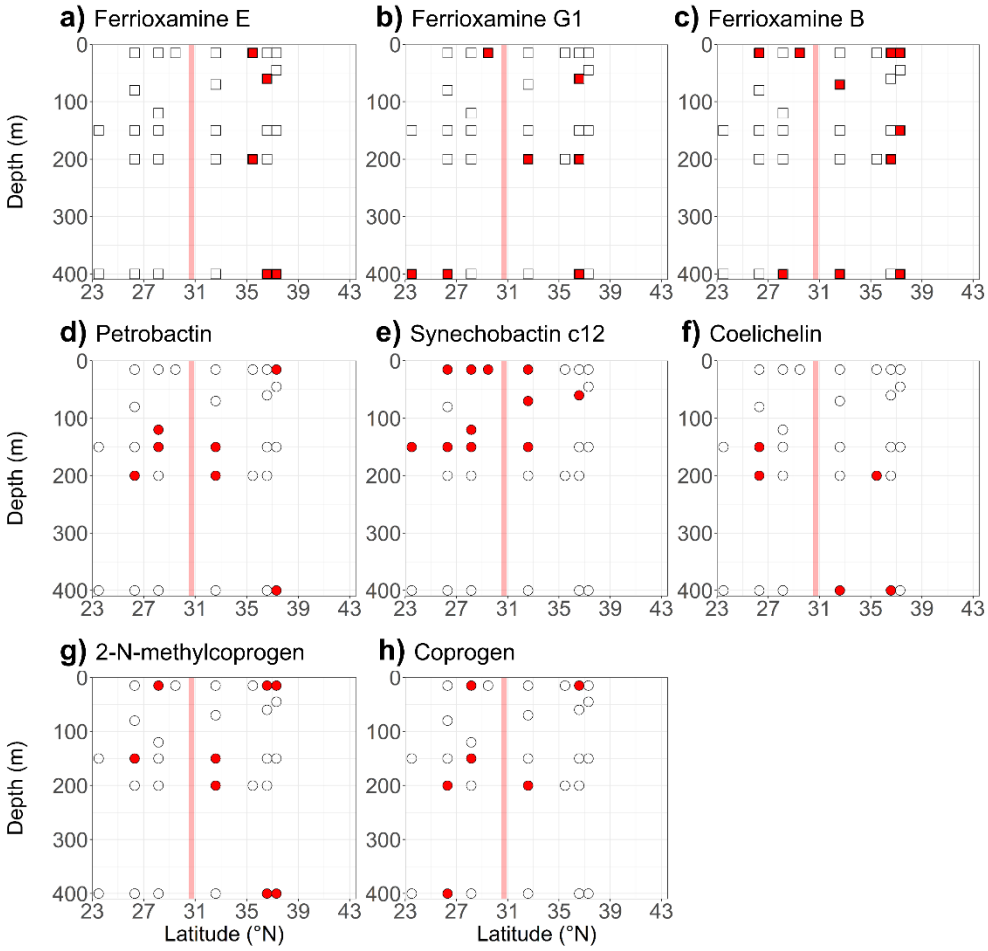

Figure 2.4 Distributions of siderophores identified with confidence level 1-3 from the Gradients 1 cruise.

Red-filled squares (Fe-bound form) and circles (Fe-free form) indicate stations where each siderophore was detected; blank squares and circles show where siderophore was not detected. Vertical red solid line indicates the location of the subtropical front from Gradients 1.

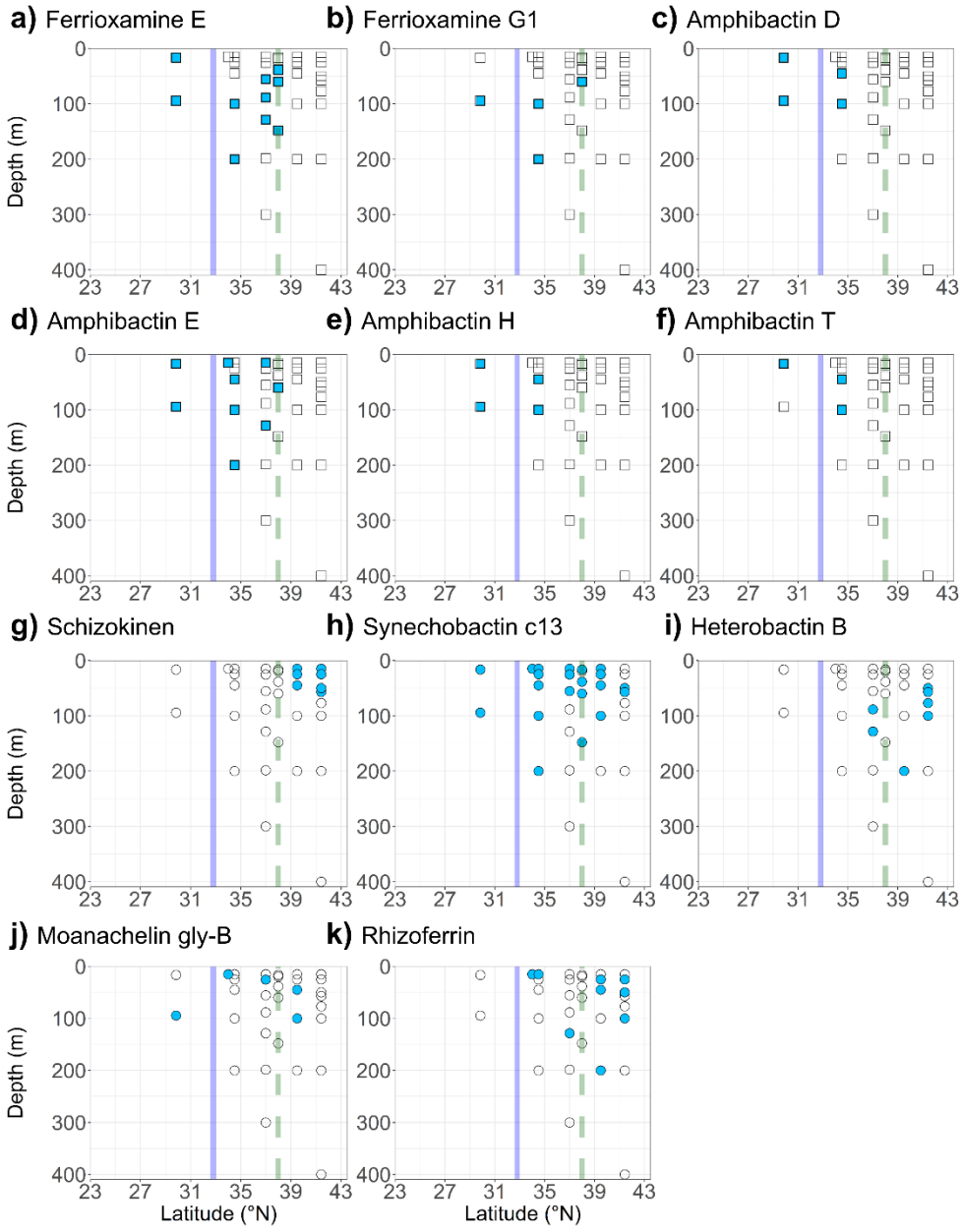

Figure 2.5 Distributions of siderophores identified with confidence level 1-3 from the Gradients 2 cruise.

Blue-filled squares (Fe-bound form) and circles (Fe-free form) indicate stations where each siderophore was detected; blank squares and circles show where siderophore was not detected. Vertical blue solid line and the green dashed line indicate location of the subtropical front and the subarctic front from Gradients 2.

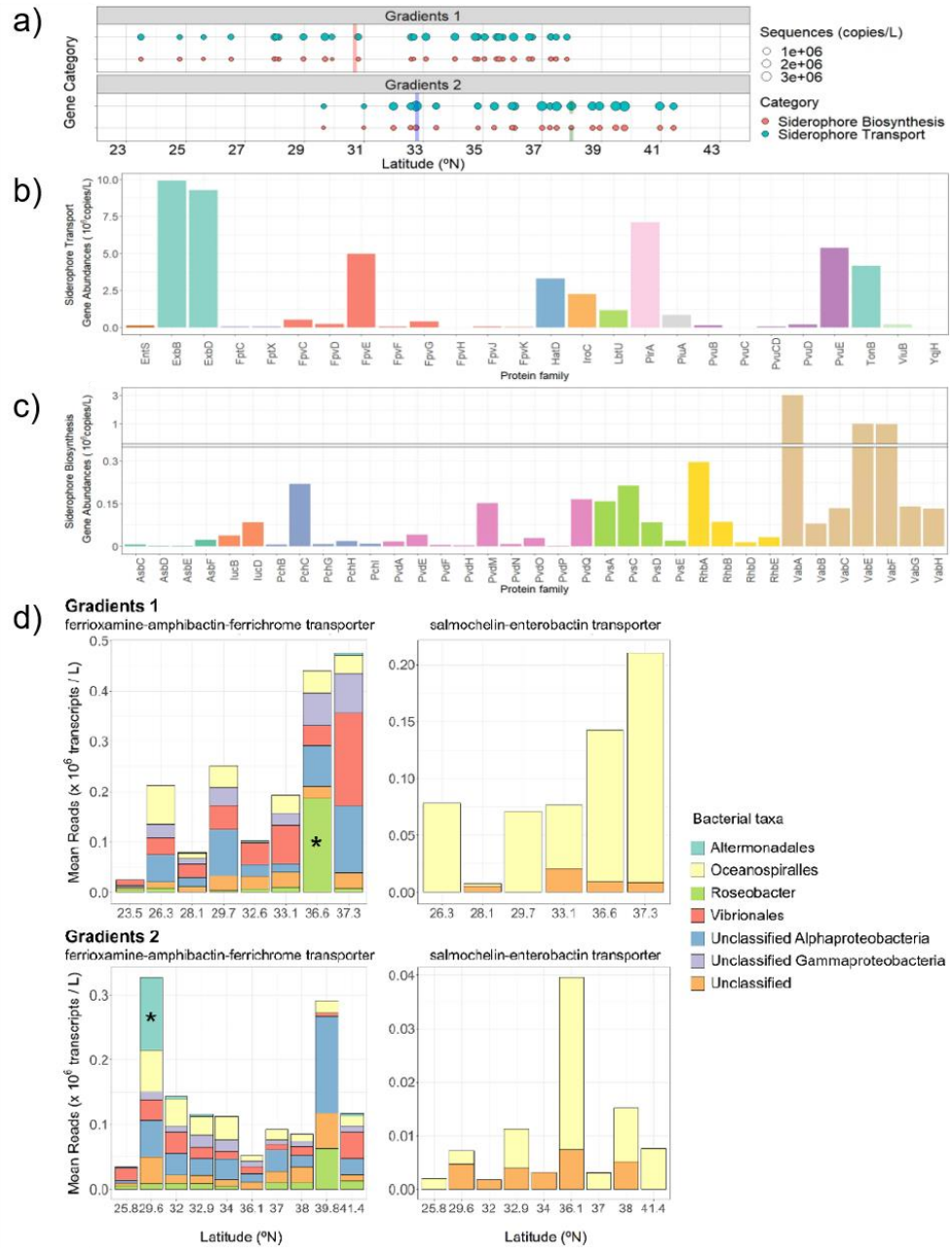

Figure 2.6 Siderophore uptake genes and transcripts abundances across the two cruise transects. A) Distribution of siderophore uptake (blue) and synthesis (red) genes across latitude at surface waters of Gradients 1 and 2 cruises. Point sizes are proportional to gene abundances (copies per liter of seawater). Vertical red and blue solid lines indicate location of subtropical fronts from Gradients 1 and 2 cruises respectively; green dashed line indicates the location of the subarctic

front from Gradients 2. B) Summed abundances of siderophore transport gene families across both Gradients 1 and 2 cruises. C) Summed abundances of siderophore synthesis gene families across both Gradients 1 and 2 cruises. D) Mean abundances of ferrioxamine-amphibactin-ferrichrome and salmochelin-enterobactin uptake transcript homologs (*10^6 transcripts per liter of seawater) from Gradients 1 and 2 cruises. Taxonomic groups that significantly changed transporter transcription levels at specific latitudes determined by the multiple comparison test ($p < 0.05$) are marked with stars.

2.9 Supplemental Methods and Results

To gain insight on which environmental parameters could predict the presence of siderophores in each sampling location, we performed a multiple logistic regression analysis on all putatively identified siderophores. The regression models included eight environmental variables (depth, latitude, temperature, salinity, photosynthetically active radiation (PAR), N + N, SRP and dissolved iron concentrations) that were standardized prior to the statistical analysis to account for different scales of measurement. To minimize the effect of multicollinearity between these predictor variables and to reduce the dimensions of the datasets, a principal component analysis (PCA) was first conducted using samples from both cruises. The first three principal components (PCs) accounted for 91% of the variation, so these three PCs were used to build initial multiple logistic regression models. Among 78 putatively identified siderophores (levels 1-4), we only built models built for 21 siderophores that were neither very widely or rarely detected (between 15-85% of all sampling locations) to avoid skewing model predictions using too many or too few zeros. For the 21 compounds, each PC in the initial model was substituted for environmental variables that were contributing most strongly to each PC. The best performing models were initially selected based on lowest Akaike information criterion (AIC)

values, but to avoid selecting highly correlated predictors, models with predictors that exceeded variance inflation factor (VIF) values of 3 were rejected and the next best models were selected.

Our analysis was limited in that the model parameters evaluated did not include biological parameters such as productivity, biomass and microbial community composition, which are potentially important parameters for siderophore predictions, because discrepancies in sampling locations made it difficult to pair some of our biological data directly with the siderophore measurements. In addition, the accuracy of the current regression models was further limited by both the small size of our dataset and the range of environmental parameters measured during the two cruises. We believe that additional siderophore measurements from different areas of the ocean would likely improve the performance of current models.

Despite these limitations, we find that latitude was the most effective predictor variable among the variables tested in both cruises from our regression models (included in 16 models out of 21) (Supplementary Table 2.5). The regression coefficients of latitude for compounds detected during the April 2016 cruise were mostly negative (8 out of 9), whereas those for compounds detected during the June 2017 cruise were all positive. This trend may be partly due to the differences in sampling locations between the two cruises, since dissolved siderophore samples were collected from relatively lower latitudes in the April 2016 cruise than the June 2017 cruise, and the statistical analyses combined data from both cruises.

Following latitude, salinity was also identified as a significant predictor for 4 compounds, although replacing salinity with latitude returned almost equally efficient regression models, with slightly higher AIC scores (5-10) relative to the best models. Dissolved iron concentration was also identified as a potentially important predictor for three siderophores found in April 2016, which were all predicted to be more likely to be found with low iron. Lack of predictive power

of dissolved iron towards siderophores may be expected, considering that siderophores have been shown to be present in both iron-limiting and iron-replete areas of the ocean (Mawji et al. 2008; Boiteau et al. 2016a; Bundy et al. 2018; Boiteau et al. 2019).

N + N concentrations and depth were found as a significant predictor in two and one compounds respectively, but the relationship between siderophores and macronutrients or depth are still largely unclear. There have been contradicting reports from culture studies about whether macronutrients can significantly affect siderophore, even within the same genus that produce the same siderophores (Fallahzadeh et al. 2010; Vindeirinho et al. 2021). Previous studies that identified siderophores from seawater have also largely focused on surface waters, which limits our knowledge on siderophores at depth.

2.10 SUPPLEMENTAL FIGURES AND TABLES

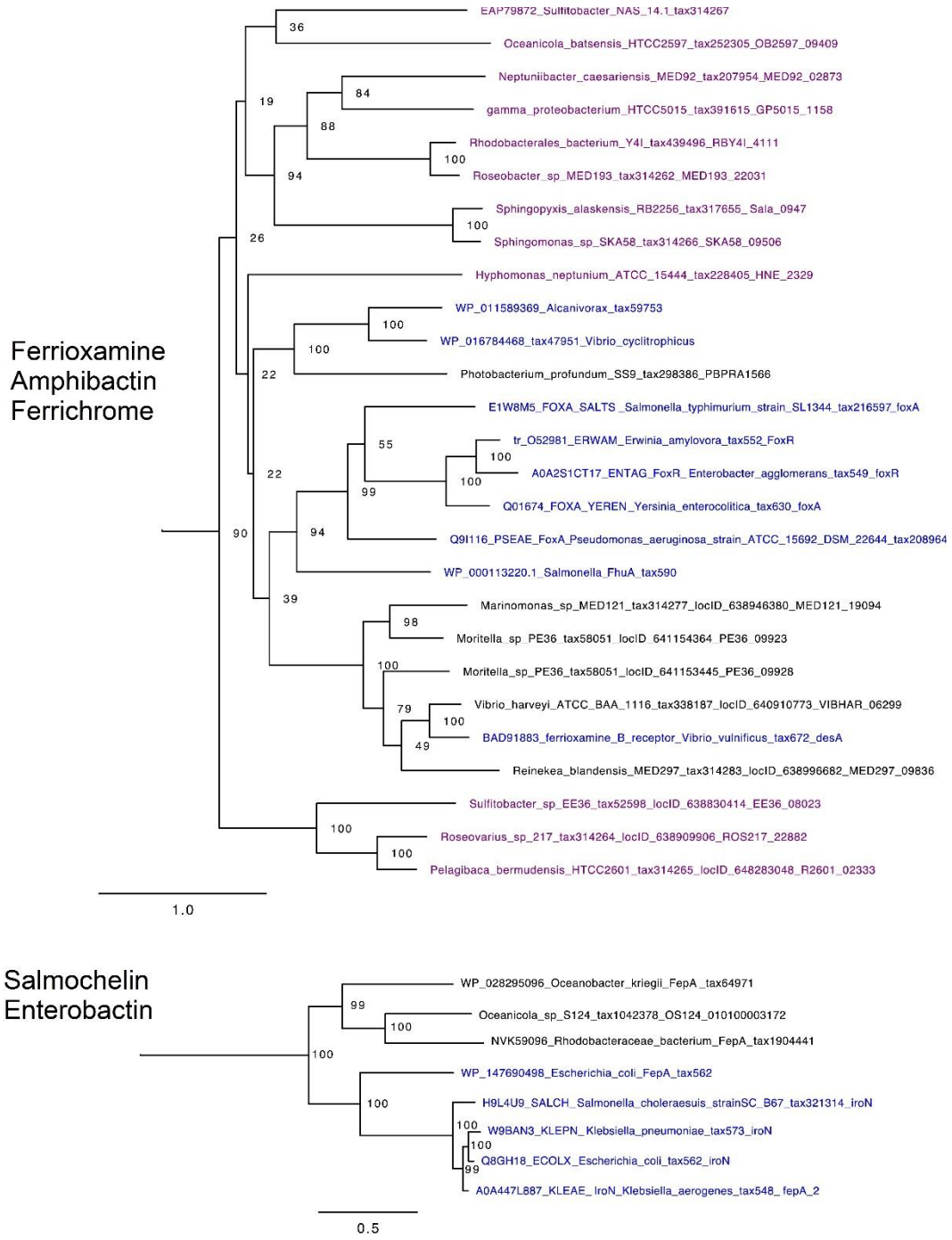

Supplementary Figure 2.1 Phylogenetic reference trees used to recruit ferrioxamine-amphibactin-ferrichrome transporters and salmochelin-enterobactin transporter homologs.

Blue sequences are experimentally verified protein sequences, black sequences are close homologs to the experimentally verified protein sequences, and purple sequences are more distant homologs to the experimentally verified protein sequences. Values at the nodes show the number of times the clade appeared in 100 bootstrapped data sets, and the scale bar indicates number of substitutions per site. Sequence names include the name of the organism, the locus tag and/or the NCBI protein accession number, and the NCBI taxonomy number ("tax###").

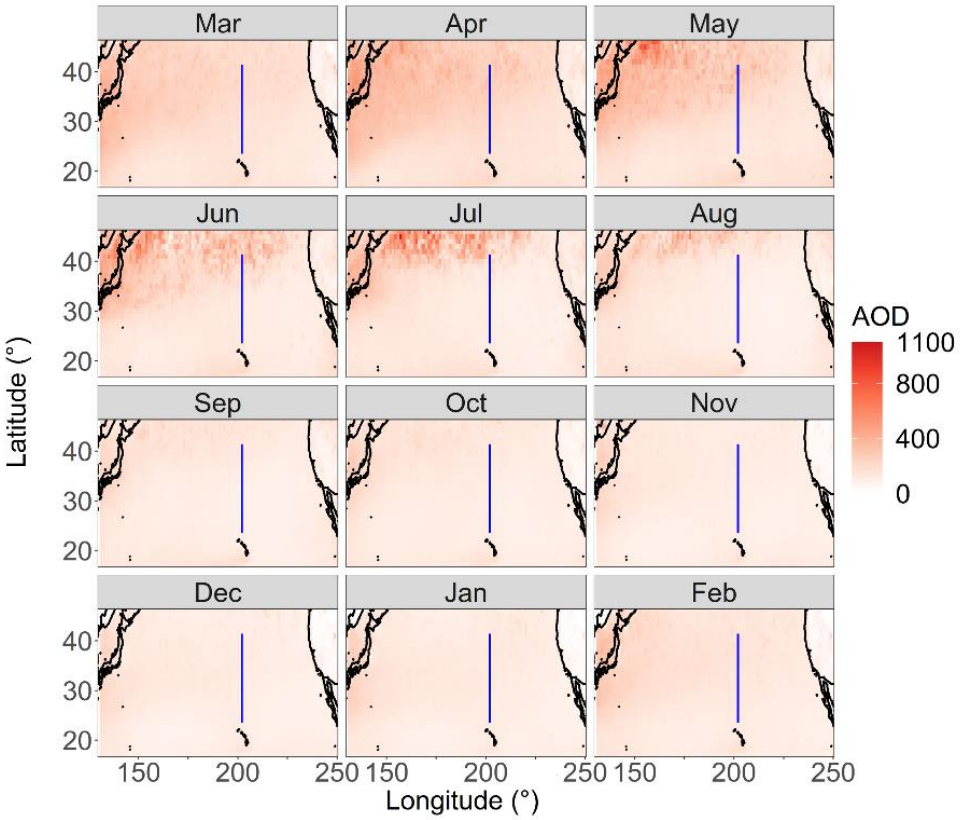

Supplementary Figure 2.2 Monthly aerosol optical depth (AOD) distribution over the North Pacific Ocean, from NASA's MODIS-Aqua satellite.

Monthly data from 2003 to 2018 was averaged over 1 × 1 degree pixels for plotting. Blue line shows both cruise transects from 23.5°N to 41.4°N.

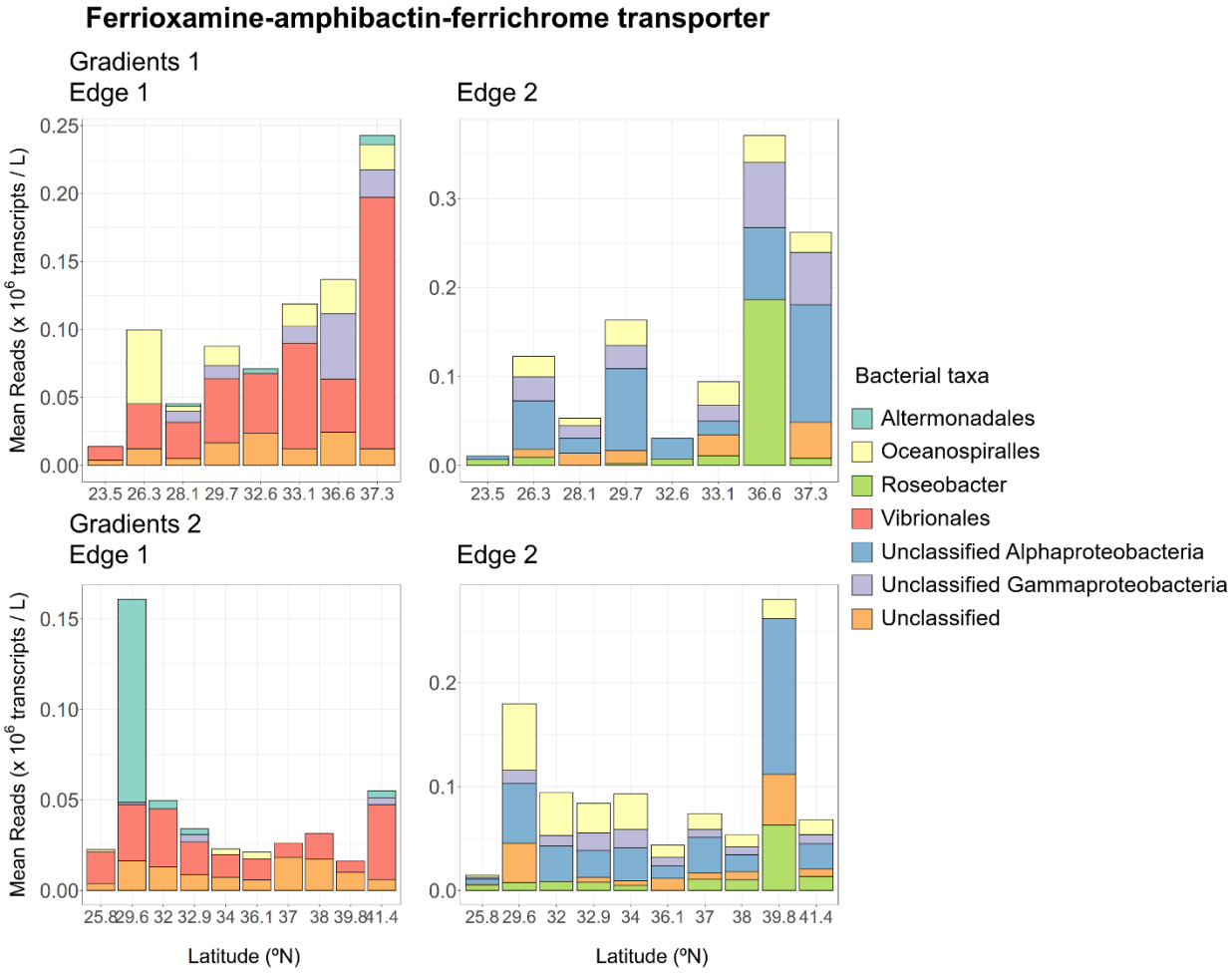

Supplementary Figure 2.3 Mean abundances of ferrioxamine-amphibactin-ferrichrome uptake transcript homologs (*10^6 transcripts per liter of seawater) from Gradients 1 and 2 cruises. Sequences that are more closely related to experimentally verified sequences (black sequences in Supplementary Figure 2.1) and less closely related (purple sequences in Supplementary Figure 2.1) were counted separately as Edge 1 and Edge 2.

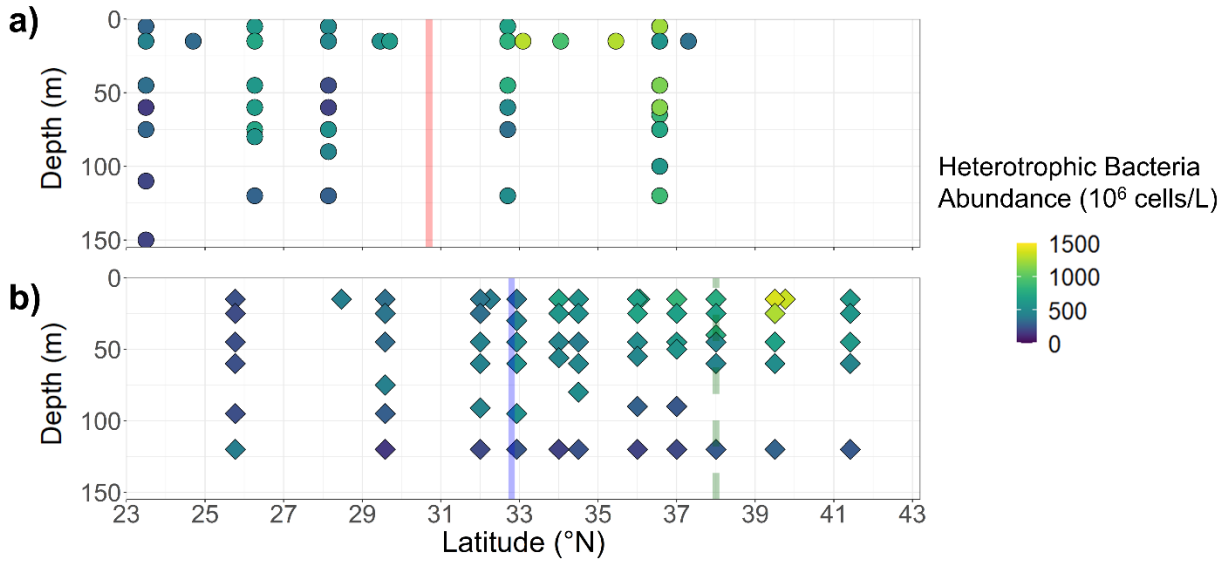

Supplementary Figure 2.4 Abundance of heterotrophic bacteria determined by flow cytometry from A) Gradients 1 and B) Gradients 2 cruises. Vertical red and blue solid lines indicate the location of subtropical fronts from Gradients 1 and 2 cruises respectively; vertical green dashed line indicates the location of the subarctic front from Gradients 2.

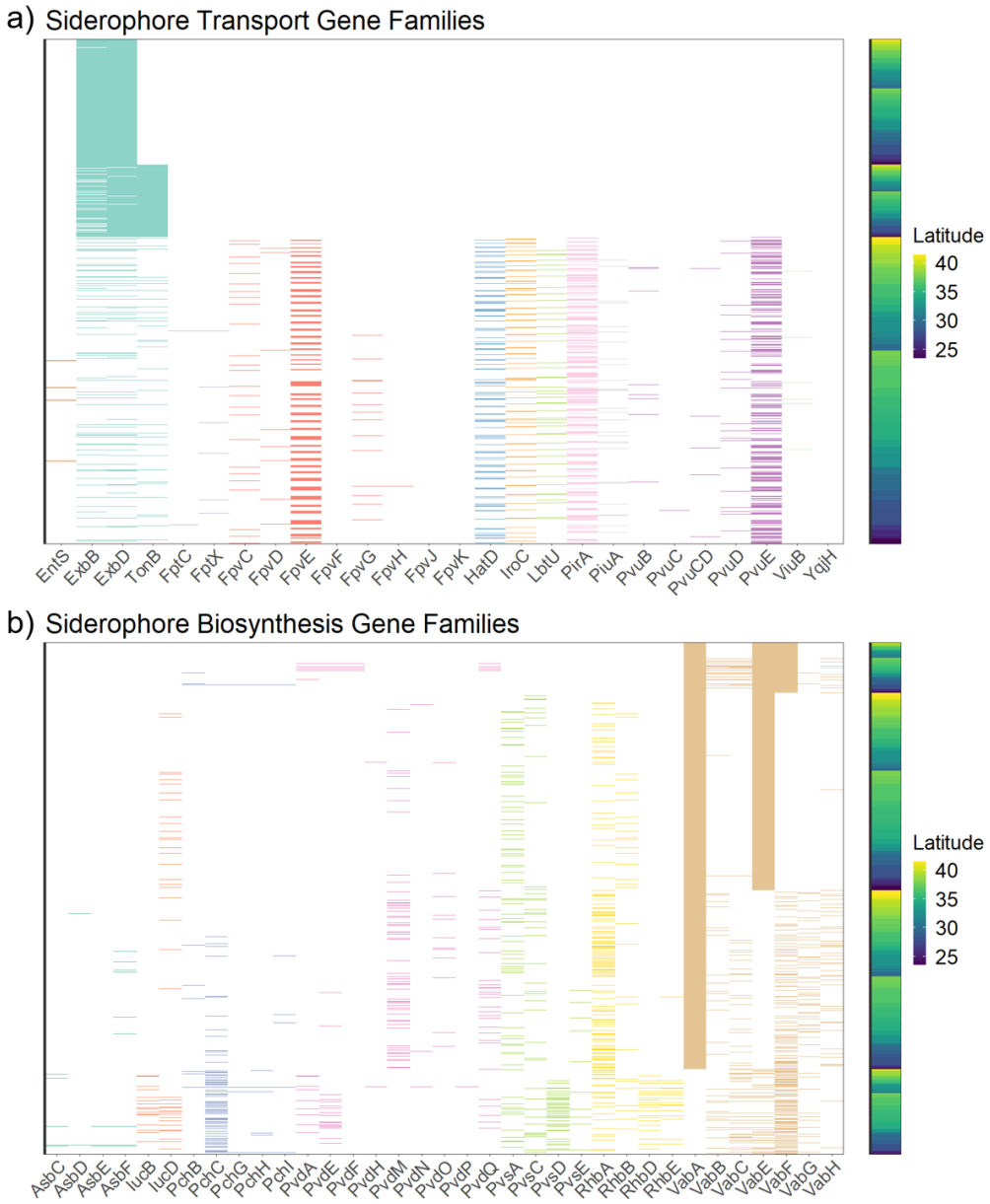

Supplementary Figure 2.5 Distribution and abundances of siderophore transport genes in metagenomes from both cruises. Each row of each panel corresponds to individual contigs, and colored rows indicate that the contig included sequences similar to A) siderophore transport gene sequences or B) siderophore biosynthesis gene sequences. Genes that are involved in the same siderophore uptake system or in the same siderophore biosynthetic gene clusters were assigned same colors. The rows on each panel were sorted by the three most abundant gene families detected across all contigs. The color bars on the right indicate the latitude at which each row (or each contig) was sampled from.

Supplementary Table 2.5 Results of multiple logistic regression analyses on each siderophores Each row on the table shows individual siderophores, for which one or more variables were identified as significant ($p < 0.05$) predictors in each logistic regression model. The top column shows the environmental variables, and the second column shows whether each siderophore was identified from Gradients 1 (G1) or Gradients 2 (G2) cruises. Positive and negative regression coefficients for each variable are noted in cells filled with red and blue respectively.

Siderophore	Latitude		Salinity		N + N		dFe		Depth	
	G1	G2	G1	G2	G1	G2	G1	G2	G1	G2
Agrobactin A			2.97				-6.61			
Amonabactin P693	-0.38				0.48		-8.31			
Carboxymycobactins 108_1		0.76								
Desferrioxamine T1	-0.25									
Desferrioxamine T2	-0.26									
Desferrioxamine T3	-0.16									
Erythrochelin		0.29								
Heterobactin B	-0.35									
Micacocidin	-0.24									
Mycobactin H		0.66								
Mycobactin P		0.39								
Mycobactin R		0.69								
Mycobactin T			-1.62							
Neocoprogen II		0.45								
Parabactin A	-0.28									
Protochelin	-0.24									
Salmochelin SX									-0.04	
Synechobactin c12			3.54							
Synechobactin c13	0.35				-0.44					
Vanchrobactin		0.33								
Vibriobactin			3.32				-6.77			

Chapter 3. CONNECTING THE DISSOLVED COBALT POOL WITH COBALT UPTAKE AND CYCLING IN THE NORTH PACIFIC

3.1 ABSTRACT

Cobalt is an essential element for life, particularly due to its role as the metal center in cobalamins. In the ocean, the most bioavailable form of cobalt is uncomplexed or weakly complexed cobalt, but the majority of dissolved cobalt in the ocean is strongly complexed to organic ligands. Based on these ligands' binding strengths, some are presumed to be cobalamins and their degradation products. Although the speciation of cobalt-binding ligands has important implications for cobalt bioavailability and primary productivity, the identity of these ligands remains underexplored. In this study, we aimed to identify cobalamin-related compounds in surface waters across a meridional transect in the North Pacific. Despite dissolved cobalt concentrations ranging from 30 to 87 pM across the transect, no cobalamin related compounds were identified. Low cobalamin cellular quotas and active transcription of cobalamin uptake and repair-related genes suggest that cobalamin is rapidly cycled across the transect, and cobalamins may not be accumulating in seawater as cobalt-binding ligands. Instead, we found the cobalt-binding ligand pool to be highly complex and heterogeneous, consisting of individual ligands with concentrations below 2.5 pM.

3.2 INTRODUCTION

Cobalt is an important bioactive trace metal. It is the metal center in vitamin B_{12} and related compounds (cobalamins), which are important cofactors for multiple enzymes that regulate DNA synthesis, carbohydrate and amino acid metabolism, and it can also substitute for zinc in carbonic anhydrase (Price and Morel 1990; Sunda and Huntsman 1995; Roth et al. 1996; Gruber et al. 2011). Some microbes including *Prochlorococcus*, *Synechococcus* and *Trichodesmium* have an absolute cobalt requirement (Sunda and Huntsman 1995; Saito et al. 2002; Rodriguez and Ho 2015). Nearly all of the dissolved cobalt in the surface ocean is complexed to strong organic ligands (Saito and Moffett 2001; Saito et al. 2005). Dissolved cobalt concentrations are very low in open ocean surface waters (<30 pmol/L) (GEOTRACES Intermediate Data Product Group 2021) due to a combination of biological uptake and scavenging (Bruland and Lohan 2003). As a result, cobalt has been identified as a primary or co-limiting nutrient for phytoplankton productivity in different areas of the ocean (Saito et al. 2005; Moore et al. 2013; Browning et al. 2017).

The interplay between cobalt and microbial communities in the ocean is highly complex. Cobalt distributions and speciation affect microbial cobalt uptake, recycling and community composition. For instance, compositional shifts in the phytoplankton community along with changes in cobalt speciation from labile (either free or weakly complexed cobalt) to strongly complexed cobalt suggest that the bioavailability of cobalt is influenced by cobalt speciation (Saito et al. 2004). The organic ligands that control cobalt speciation are thought to be microbially-produced, such as from *Prochlorococcus* and *Synechococcus* (Saito et al. 2002, 2005; Bown et al. 2012). However, despite their importance role in shaping microbial communities, the identity of organic cobalt-binding ligands is largely unknown.

Cobalamin and its degradation products have been hypothesized to be a major component of the cobalt-binding ligand pool due to the similarity between the binding strength of naturally-occurring cobalt ligands in seawater and that of cobalamins (Ellwood and van den Berg 2001; Saito et al. 2005; Hawco et al. 2020). Cobalamin concentrations in open ocean surface waters are very low (0-6 pM) (Menzel and Spaeth 1962; Carlucci and Silbernagel 1966; Panzeca et al. 2008; Bonnet et al. 2013; Joglar et al. 2020) due to a combination of factors including its photoreactivity (with a half-life on the timescale of days), limited *de novo* production by a subset of bacteria and archaea, and high biological demand (Carlucci et al. 1969; Panzeca et al. 2009; Shelton et al. 2019). These low concentrations can drive cobalamin, or vitamin B12, to be a limiting nutrient in different areas of the ocean, such as South Atlantic, Southern Ocean and Gulf of Alaska (Bertrand et al. 2007, 2015; Koch et al. 2012; Browning et al. 2017).

The high demand for exogenous cobalamins by microbes in the marine environment makes the accumulation of this micronutrient in seawater as an organic ligand for cobalt surprising, but nevertheless very few other potential candidates for the observed dissolved organic cobalt ligands in seawater have been suggested. In this study, we used a combination of metatranscriptomics, voltammetry and mass spectrometry techniques to assess the cobalamin status of the *in situ* microbial community and determine how the microbial community is influencing the speciation of cobalt in the subtropical and subpolar North Pacific. Future research directions and possible candidates for organic cobalt-biding ligands in seawater are also proposed and discussed.

3.3 METHODS

3.3.1 *Cobalt ligand analysis*

Samples for dissolved cobalt ligands and dissolved cobalt analysis were each collected from two cruises with overlapping transects in the North Pacific (Gradients 1 on the R/V *Ka'imikai-O-Kanaloa* from April 19 to May 3, 2016, and Gradients 3 on the R/V *Kilo Moana* from April 9 to 30, 2019, respectively). Both cruises travelled along 158°W, from 23.5°N to 37.3°N for Gradients 1 and 25.9°N to 42.3°N for Gradients 3.

Surface seawater was collected at 5-15 m depths, either using a trace metal-clean rosette equipped with Niskin-X sampling bottles with Teflon-coated springs (General Oceanics) on a non-metallic line, or using a trace metal clean "towfish" (Vink et al. 2000). 10-20 liters of seawater was sub-sampled from the Niskin-X bottles in a HEPA-filtered clean space on board, filtered through acid-cleaned 0.2 µm Acropak 200 filters (Pall Corporation), and pumped onto Bond Elut ENV columns (1g, 6 mL, Agilent Technologies) at a flow rate of 18 mL/min. The columns were cleaned and activated prior to loading seawater with 12 mL of pH 2 Milli-Q water followed by 12 mL of methanol (Fisher Scientific, Optima grade) and then 12 mL of Milli-Q water. After the columns were loaded, they were washed with 12 mL of Milli-Q water to remove salts, and eluted with 13 mL of Optima grade or distilled methanol into acid-cleaned polyethylene 15 ml tubes. The eluents were dried down using a SpeedVac vacuum concentrator with a refrigerated vapor trap (Thermo Scientific), brought up to 500 µL with Milli-Q water and stored at -20°C until analysis.

For quantification of cobalt binding ligands, liquid chromatography (LC) was coupled to an iCAP-RQ inductively coupled plasma mass spectrometer (Thermo Scientific). The LC system

(Dionex Ultimate 3000 HPLC, Thermo Scientific) was equipped with a PEEK ZORBAX-SB C18 column (4.2 x 150 mm, 3 µm, Agilent Technologies), and compounds were separated using a flow rate of 50 µL/min and a gradient of water and methanol buffered with 5 mM ammonium formate (Boiteau et al. 2016a; Bundy et al. 2018). The ICP-MS was equipped with platinum sample and skimmer cones, and samples from the LC were introduced using a PFA-ST nebulizer (Elemental Scientific) at a flow rate of 50 µl/min. Samples were analyzed in kinetic energy discrimination mode with helium collision gas at a flow rate of 3.8-4.0 mL/min and 10 % oxygen flow. Total ^{59}Co signal on the ICP-MS was quantified using cyanocobalamin as an external standard.

For identification of cobalt binding ligands, liquid chromatography was coupled to a Q-Exactive Orbitrap mass spectrometer (Thermo Scientific) with the same LC system and settings as for the quantification of cobalt ligands. Both MS^1 and MS^2 scans were collected using the following MS settings: MS_1 (full positive mode, 120,000 mass resolution, 100,000 AGC target, 100 ms maximum inject time, 200-2,000 *m/z* range) and dd-MS^2 (30,000 mass resolution, 20,000 AGC target, 100 ms maximum inject time, 1.0 *m/z* isolation window, normalized collision energy 35). We searched for masses and fragments associated with cobalamin analogs in the MS^1 and MS^2 data respectively, similar to an approach taken to identify organic arsenic compounds (Heal et al. 2022). The list of exact masses included commonly known corrinoids, including cobalamin analogs (cyanocobalamin, hydroxycobalamin, methylcobalamin and adenosylcobalamin), pseudocobalamin analogs, cobinamides and cobamides, while the list of fragments included known MS^2 fragments from cobalamin analogs (list and references in Supplementary Table 3.2). We also attempted to identify additional cobalt binding ligands by re-injecting the same samples under the same LC and MS settings but using higher normalized

collision energies of 140, 160 and 180 and the MS^1 *m/z* range limited to 50-750 to dissociate individual cobalt atoms (Tsednee et al. 2016), and searching for any precursor ions that had fragments matching the exact mass of ^{59}Co.

3.3.2 *Dissolved cobalt analysis*

Dissolved and labile cobalt concentrations were measured using cathodic stripping voltammetry, on a BASi Controlled Growth Mercury Electrode connected to a BASi Epsilon Eclipse analyzer. Sample preparation and analysis steps were adapted from Saito and Moffett (2001). Shortly, for dissolved cobalt analysis, samples were first UV oxidized to dissociate cobalt from strong cobalt-binding ligands, at 80°C for 2 hours. After the samples cooled down, 8.5 mL of each sample were poured into Teflon reaction cells, and 38.8 µL of recrystallized 0.1M DMG (dimethylglyoxmie), 130 µL of TM clean 0.5M EPPS buffer and 1.5 mL of TM clean 1.5M sodium nitrate were added. For labile cobalt analysis, 8.5 mL of each sample and 38.8 µL of recrystallized 0.1M DMG were added to acid cleaned 15 mL polypropylene tubes and left to equilibrate overnight (approximately 12 hours). After the equilibrated samples were poured into Teflon cells, 130 µL of TM clean 0.5M EPPS buffer and 1.5 mL of TM clean 1.5M sodium nitrate were added immediately before analysis. Samples were purged with 99.999% N_2 for 300 s, stirred for 90 s during deposition at -0.6V, equilibrated for 15 s, then went through a linear sweep from -0.6V to -1.4V at 10 V/s scan rate. After each scan, additions of 1 mg/L Co standards (ranging from 5 to 200 pM) provided a standard calibration curve to calculate dissolved and labile Co concentrations. For analytical blanks, filtered open ocean seawater from the surface equatorial Pacific was used.

3.3.3 *Particulate cobalamin analysis*

Samples for particulate cobalamin were collected on the Gradients 1 cruise at 15m depth, either from a CTD rosette or the ship's underway system. For particulate cobalamin analysis, 10-12 liters of seawater was sub-sampled into acid-washed polycarbonate carboys, and filtered through 147 mm 0.2 µm polytetrafluoroethylene (PTFE) filters. Filters were extracted as previously described in Boysen et al. (2018) by the Ingalls lab at University of Washington. These filters are also splits of the same samples as described in Heal et al. (2021). In short, filters were extracted by bead beating for 30 seconds with 1:1:2 methanol:water:dichloromethane and chilling at -20°C for 15 minutes three times. Extracts were centrifuged to obtain aqueous and organic fractions separately, dried down under clean N_2, and re-dissolved in solvents with isotope-labeled internal standards spiked in. To protect samples from photodegradation, samples were covered in foil whenever possible. All samples were analyzed using a LC (Waters I-Class Aquity UPLC) using the LC conditions as in Heal et al. (2019) coupled to a triple quadrupole mass spectrometer (Waters Xevo TQ-S), identified and quantified as described in Heal et al. (2017).

3.3.4 *Transcriptome analysis*

We scanned environmental metatranscriptomes to retrieve normalized transcript counts for gene families of interest. 11 and 3 gene families were selected as biomarkers for the cobalamin synthesis pathway (Doxey et al. 2015; Lu et al. 2020) and the cobalamin transport pathway respectively, and their HMM (hidden Markov models) profiles from TIGRFAM (Haft 2003) and Pfam (Finn et al. 2014) were used for the analysis. Profile HMMs are probabilistic models that

are built from multiple sequence alignments to quickly identify homologous sequences (Eddy 1998; Finn et al. 2014).

Whole-community metatranscriptomes from the Gradients 1 cruise were collected, extracted and sequenced by the Armbrust lab at University of Washington as described previously (Durham et al. 2019). In brief, seawater was sequentially filtered through a 200 μm prefilter and collected on 3 μm and 0.2 μm filters and flash-frozen in liquid nitrogen. Total RNA was extracted, rRNA-depleted and sequenced on an Illumina NovaSeq 6000 platform. Quality-controlled transcript fragments were translated into six frames with transeq vEMBOSS:6.6.0.0 (Rice et al. 2000) using the Standard Genetic Code, and potential protein sequences with ≥ 40 uninterrupted amino acids were retained for further analysis. We used HMMER 3.3 (Eddy 2011) to identify gene families of interest from these whole-community surface metatranscriptomes, using a minimum e-value threshold of $1e^{-05}$.

Environmental transcripts recruited by these HMM profiles were then annotated taxonomically using DIAMOND v 0.9.18 (Buchfink et al. 2015) (parameters: --sensitive -b 10 -c 1 -e 1e-5 --top 10 -f 100) against a custom reference sequence library containing 907 marine-relevant genomes and transcriptomes from prokaryotes and eukaryotes (Coesel et al. 2021). The Lowest Common Ancestor (LCA) was estimated using the LCA algorithm in DIAMOND in conjunction with NCBI taxonomy.

The raw transcript counts from triplicate samples for each gene family were normalized by the total number of short reads for each sample and averaged at each latitude. A one-way ANOVA test and a post-hoc Tukey test between latitude and transcript abundances was conducted to determine whether there were statistically significant differences in mean transcriptional abundances between latitudes.

3.4 Results and Discussion

3.4.1 *Organic speciation of cobalt in North Pacific surface waters*

Dissolved cobalt concentrations measured by cathodic stripping voltammetry (CSV) across the Gradients 3 transect (158°W, 25.9°N to 36.6°N) averaged 74.2 ± 22.9 pM (Figure 3.1). These concentrations are up to ten-fold higher than those obtained from surface waters within the same latitudinal range of the GEOTRACES GP15 Pacific Meridional Transect along 152°W from September to October 2018 (Saito 2021). The difference in dissolved cobalt distributions between the two geographically close transects may be attributed to seasonality, or to differences in cobalt sources between the two locations. In the open ocean, where there is no external source of cobalt from rivers, coastal sediments or hydrothermal vents, cobalt ligand abundances in the open ocean are likely primarily controlled by biological production and uptake (Saito et al. 2002, 2005). Therefore, our observations may be reflecting higher cobalt concentrations in the early spring, while high productivity during the late spring and summer led to depletion of dissolved cobalt in the fall observed in Saito (2021).

A fraction of the total dissolved cobalt pool in the ocean exists as labile cobalt, which includes either free cobalt or cobalt complexed to weak ligands that are exchangeable with dimethylglyoxime (DMG) (Saito et al. 2004). Across the same transect, labile cobalt concentrations measured by CSV were consistently below the detection limit at all latitudes, suggesting that almost all dissolved cobalt across the surface transect was complexed to strong organic ligands. Multiple studies have found labile cobalt to be very depleted in open ocean surface waters, including sections of the South Pacific, North and South Atlantic (Saito et al. 2004; Noble et al. 2012, 2017; Hawco et al. 2016). Depletion of labile cobalt at the euphotic

zone is likely due to its high bioavailability to phytoplankton (Saito et al. 2004, 2005) or possibly to ligand exchange and scavenging processes (Noble et al. 2017).

We also quantified the pool of dissolved cobalt ligands that are captured on the solid phase extraction (SPE) columns by LC-ICP-MS. Total cobalt binding ligand concentrations across the Gradients 1 transect (158°W, 23.5°N to 37.3°N) averaged 49.7 ± 16.6 pM (Figure 3.1). We note that seawater samples for CSV measurements and LC-ICP-MS measurements were taken from different cruises, but the latitudinal range of sampling locations and the timing of sampling between the two cruises were very similar. The solid phase extraction method used in this study was initially optimized for quantifying strong iron-binding ligands (Bundy et al. 2018), but as dissolved cobalt concentrations quantified by both methods are on the same order of magnitude, the SPE method may successfully retain the bulk of the total dissolved cobalt pool.

No distinct cobalt peaks in the LC-ICP-MS chromatograms in the samples were found (Figure 3.2). A cobalamin standard injected into our system appeared as a distinct peak at ~15 minutes, but the environmental samples showed up as one large unresolved peak between 18-30 minutes (Figure 3.2), suggesting a highly complex and slightly less polar cobalt-binding ligand pool that are unable to be resolved by our current chromatography method. These unresolved peaks have been observed in earlier studies that focused on iron, nickel and copper binding ligands and were interpreted as uncharacterized organic matter, although distinct peaks on top of the unresolved peaks have also co-occurred (Boiteau et al. 2016; Bundy et al. 2018; Boiteau et al. 2019).

We did not find a clear latitudinal trend in the dissolved cobalt concentrations measured by either CSV or ICP-MS. However, neither method provides direct information on the bioavailability of dissolved cobalt. Measurements of labile cobalt give an indication of

bioavailability, but as the CSV method only allows us to distinguish between ligands that bind to cobalt more or less strongly, relative to the competitive ligand (DMG), the dissolved organic cobalt pool that is complexed to ligands stronger than DMG may still be bioavailable to microbes. Therefore, it is unclear whether biologically available cobalt pools are also uniform across latitude without a better understanding of the different components of the dissolved organically-complexed cobalt pool.

3.4.2 *Cobalamin cellular quotas may reflect low cobalt or cobalamin availability across the study transect*

While understanding the distribution and speciation of cobalt would greatly improve our current understanding of cobalt nutritional status and the influence of cobalt speciation on shaping microbial community structure, the identities of cobalt ligands are unknown to date. Earlier studies suggest that cobalamin-related compounds may comprise at least some part of the cobalt binding ligand pool. However, as cobalamin concentrations in the ocean are very low, it may be unlikely that dissolved cobalamins that may be functioning as organic cobalt binding ligands are accumulating in seawater. Therefore, we tried to assess the supply of cobalamin to microbial communities across this study transect.

As earlier studies show that marine cyanobacteria synthesizes and uses pseudocobalamin, an analog of cobalamin, rather than cobalamins, as other eukaryotes, bacteria and archaea do (Helliwell et al. 2016; Heal et al. 2017), pseudocobalamin cellular quotas from the study transect were estimated using *Prochlorococcus* and *Synechococcus* cell carbon biomass. We calculated a quota of 26.5 ± 35.2 nmol pseudocobalamin / mol C on average (Table 3.1), which was on a similar order of magnitude with what was observed in North Pacific surface waters (87 nmol

pseudocobalamin / mol C), but up to two orders of magnitude lower than what was observed in cobalt-replete cultured *Prochlorococcus* and *Synechococcus* (Heal et al. 2017) (Supplementary Table 3.1). Pseudocobalamin quotas were also relatively higher and more variable at latitudes above 33°N (Table 3.1).

We did not calculate cobalamin cellular quotas because we do not have a realistic quantification of all organisms using cobalamin, which includes larger eukaryotic phytoplankton and heterotrophic organisms not captured by underway flow cytometry. Instead, particulate cobalamin concentrations were normalized to particulate organic carbon (POC). Particulate cobalamins : POC varied between 2.4 and 11.5 nmol cobalamin / mol C and were lowest at high latitudes (35.5°N and 36.6°N) (Table 3.1). These values are an order of magnitude smaller than previously observed from the San Pedro Channel or from cultures of marine bacteria, but the San Pedro Channel is strongly influenced by coastal upwelling that may result in higher growth and higher cyanocobalamin demand by microbes relative to our study site (Suffridge et al. 2017; Villegas-Mendoza et al. 2019) (Supplementary Table 3.1).

Variability in cobalamin and pseudocobalamin quotas is caused by multiple environmental conditions, such as differences in availability of cobalamin and other nutrients, light conditions and growth rate (Taylor and Sullivan 2008; Heal et al. 2017; Villegas-Mendoza et al. 2019). Multiple species of diatoms and haptophytes have been found to reduce their intracellular cobalamin concentrations in cobalamin-limited cultures (King et al. 2011; Heal et al. 2018; Nef et al. 2020). Some species of *Prochlorococcus* and *Synechococcus* were also found to reduce their cobalt quota by more than tenfold with lower extracellular cobalt concentrations, although it is unclear how much cobalt in these cells are allocated to cobalamins, or how this allocation changes with cobalt concentrations (Sunda and Huntsman 1995; Hawco et al. 2020). Therefore,

while the low environmental cobalamin quotas in our study transect do not directly suggest that the local microbial communities are experiencing cobalamin limitation, it may still be reflecting low cobalamin availability, particularly more so at low latitudes for pseudocobalamin users (cyanobacteria) and at high latitudes for cobalamin users.

3.4.3 *Cobalamin transport and synthesis transcripts can provide insight on cobalamin recycling and uptake across latitude*

To further infer the in situ cobalamin status across the study transect, we estimated the transcript abundances of genes involved in the cobalamin transport system (btuCDF), as these genes may be upregulated when cells are experiencing cobalamin limitation (Bertrand et al. 2012). While the full cobalamin transport pathway is comprised of btuBCDF genes, with btuB acting as the outer membrane receptor and btuCDF regulating cobalamin transport from the periplasm to the cytoplasm (Borths et al. 2005; Shultis et al. 2006), the btuB HMM profile did not recruit transcripts successfully, so we only report btuCDF transcripts here. The btuD gene was transcribed at higher abundances in the north (36.56°N, 37.28°N) relative to the south (23.48°N, 32.58°N, 33.08°N) (Tukey test p-values = 0.03-0.07 between each pair of latitudes) (Figure 3.3), which may suggest that the btuD transporter is being upregulated at higher latitudes to cope with higher cobalamin stress. Specifically, btuD transcripts derived from Gammaproteobacteria, Haptophyta, unclassified Alphaproteobacteria and Gammaproteobacteria were all more highly expressed in the north (ANOVA test p-values = 0.07 for Gammaproteobacteria, <0.01 for other microbial groups). This may imply that these taxa may have higher cobalamin requirements, or that they are competing for cobalamins more actively over other taxa at these latitudes. We note that most of btuD transcripts potentially derived from

haptophyceae were not taxonomically annotated below phylum level, but some were identified at genus level as Phaeocystis and Chrysochromulina. While eukaryotes are believed to acquire cobalamin through a different pathway than btuBCDF, the molecular mechanism is still largely unknown (Zhang et al. 2009a; Bertrand et al. 2012), and additional studies may be required to confirm whether these subsets of eukaryotes are equipped with cobalamin uptake systems resembling the btuBCDF transport system. In addition, low abundances of btuD transcripts also coincide with latitudes where dissolved cobalt concentrations are higher by 20-40 pM (31-34°N) (Figure 3.1, Figure 3.3). As cobalt-binding ligands are assumed to have biological origins, it may be possible that cell growth at this latitudinal range were less limited by cobalamin availability, which led to additional production of cobalt ligand concentrations.

While btuC and btuF transcript abundances between latitudes were not significantly different (Figure 3.3), the statistical significance was likely influenced by the relatively larger variability between triplicate samples at each latitude, as both transcripts were about an order or magnitude less abundant than btuD transcripts (Supplementary Figure 3.1). It is interesting that btuD transcripts were much more abundant than the btuC transcripts, as these two genes are encoded from the same btuCED operon, whereas btuF is located separately (Rioux and Kadner 1989), however whether these two genes are differentially regulated or whether these transcripts have different decay rates is unclear. Additional replicates or larger water sampling volumes may be necessary to further confirm whether btuC and btuF are also significantly upregulated at higher latitudes.

The abundance of cobalamin biosynthesis-related transcripts does not necessarily inform us about the cobalamin status of cells, but it can provide insight on what cobalamin biosynthesis pathway (*de novo* or cobalamin salvage) may be active. To address this, we used the

classification from (Lu et al. 2020) to group the 11 cobalamin biosynthesis genes into categories of “corrin ring synthesis” and “final synthesis and repair”. Although cyanobacteria produce and use pseudocobalamins rather than cobalamins, they still have the same set of corrin ring synthesis and final synthesis genes with other cobalamin-producers, and only lack genes that synthesize and activate DMB (lower ligand of cobalamin) (Helliwell et al. 2016; Heal et al. 2017). Corrin ring biosynthesis genes were mostly transcribed by *Prochlorococcus*, *Synechococcus* and Alphaproteobacteria (Figure 3.4), except at two southern stations (26.28°N and 29.70°N), where up to 55-70 % of total transcripts for cbiL/cobI and cbiF/cobM genes were derived from Choanoflagellata (more specifically the genus *Acanthoeca*). Interestingly, there is no study to date that explicitly show Choanoflagellata requires cobalamin for growth or is capable of synthesizing cobalamin. Up to 60% of cbiA/cobB transcripts were also transcribed by eukaryotes, most of which were uncharacterized, but some of the Mamiellophyceae were identified at the genus level as *Micromonas* and *Ostreococcus*. However, genomes of different *Micromonas* and *Ostreococcus* species were found to lack *de novo* cobalamin biosynthesis pathway, even though they have cyanocobalamin-dependent methionine synthase (Palenik et al. 2007; Helliwell et al. 2011).

Final repair and synthesis genes were primarily transcribed by *Prochlorococcus*, *Synechococcus* and Alphaproteobacteria, the same microbial groups that produced most of the initial cobalamin synthesis transcripts (Figure 3.4), but it is unclear whether these taxa are equipped with the full *de novo* synthesis pathway or only the salvage pathway. However, a higher proportion of transcripts were contributed by Gammaproteobacteria, which may suggest that a subset of this taxa may be able to salvage cobalamins by transporting the cobalamin intermediates produced by other bacteria and complete the last steps of cobalamin synthesis.

Indeed, we observed major contributions from Gammaproteobacteria to the total cobalamin uptake transcript pool (Figure 3.3). In addition, while *Prochlorococcus* and *Synechococcus* were major producers of cobalamins (contributing up to 68 % and 58 % of total transcripts for "corrin ring synthesis" and "final synthesis and repair" groups, respectively), they only comprised up to 17 % of the total cobalamin transport transcript pool. The relative importance of *Prochlorococcus* and *Synechococcus* in the total cobalamin synthesis and uptake transcript pools could be reflecting how a larger variety of microbes can compete for and transport cobalamin relative to synthesizing and repairing cobalamin (Bertrand et al. 2015; Heal et al. 2017; Fang et al. 2017). In summary, the transcriptome analysis suggests that while both cobalamin uptake and salvage pathway are active across latitude, more diverse microbial groups are participating in recycling cobalamins, and that transport of cobalamins may be more active in the north, possibly as a response to higher degree of cobalamin limitation.

3.4.4 *Probing the identity of dissolved organic cobalt ligands*

We tried to find evidence that cobalt ligands in seawater are likely derivatives and degradation products of cobalamin by searching for MS^1 masses of cobamides and cobinamides, and subsequently for MS^2 fragments that are believed to be characteristic of cobalamins (list in Supplementary Table 3.2), but did not identify any compounds with confidence that had matching masses or fragments. In terms of the MS^1 search, given that cobalamins are in high demand at the surface ocean and that cobalamin uptake and salvage are active, the pool of dissolved cobalamins and their biosynthetic intermediates may be too small in size or may be recycled too quickly for us to identify them. In addition, *in-situ* degradation of cobalamins leads to many diverse degradation products that are too exhaustive to search based on MS^1 alone.

However, we did not identify compounds with fragments characteristic of the corrin ring structure either, even though we expected them to be relatively well-preserved in the environment based on the stability of their structures, which stays intact when analyzed using the "typical" soft ionization mode (with collision energy between 20-40 eV) on ESI mass spectrometers (Carkeet et al. 2006; Owen et al. 2011; Chamlagain et al. 2018). While we found some compounds that had fragments matching the exact mass of lower ligands of cobalamins (DMB, 147.092; adenine, 136.062), these fragments may be derived from other sources other than cobalamins and are not sufficient alone to infer the presence of cobalamin-related compounds. Our current MS^2 search may not include fragments that occur naturally in the environment, as there is also no prior knowledge of how cobalamin degrades photochemically or microbially after the lower nucleotide loop is removed from the corrin nucleus. The current MS^2 search would greatly benefit from future studies that characterize cobalamin degradation products over long periods of time – for instance, by growing cyanobacterial cultures and measuring the cobalamins over time as they are taken up and recycled.

As we did not detect cobalamins and related compounds from the searches above, we also looked for compounds that may be unrelated to cobalamin but still contain cobalt using high-energy collisional dissociation (Tsednee et al. 2016). A 100 nM cyanocobalamin standard injected on our LC-ESI-MS system produced a MS^2 fragment that match the exact mass of ^{59}Co from a precursor ion with *m/z* of 678.291 (corresponding to the exact mass of cyanocobalamin with a +2 charge). However, free cobalt atoms were not detected in the fragmentation spectra of any isolated precursor ions when the same method was applied to environmental samples. This may be due to very low concentrations of individual cobalt-containing organic compounds in seawater. If we assume that we need to inject at least 100 nM of a single cobalt-containing

compound to observe enough ^{59}Co fragment in its fragmentation spectra, given that our cobalt ligand samples were extracted from 10-20 liters of seawater and concentrated to 500 μL, the concentration of each cobalt-containing compound in natural seawater to be identified on the mass spectrometer using this method should be 2.5-5 pM. As the cobalt ligand concentrations across the transect measured on the LC-ICP-MS averaged 49.7 ± 16.6 pM, the chances of finding a single cobalt ligand compound making up 5-10 % of the total cobalt ligand pool are likely low. Therefore, we suggest that a larger volume of seawater may need to be collected and preconcentrated for a successful application of this high collision energy LC-ESI-MS method on natural seawater samples.

Apart from focusing on cobalamins and their derivatives as components of the cobalt binding ligand pool, we may also need to consider that compounds unrelated to cobalamins may be able to bind cobalt. For example, cobalt has been shown to have very high affinity for strong iron-binding ligands (siderophores) including desferrioxamine B and for pyridine-2,6-bis(thiocarboxylic acid) (Cortese et al. 2002; Duckworth et al. 2009). While it has not yet been shown directly whether microbes can actively take up cobalt-bound siderophores similar to the way they take up iron-bound siderophores (Bi et al. 2010), the strong binding affinity of siderophores for cobalt may make them potential candidates for components of the cobalt ligand pool. However, we note that in our data we did not find cobalt-bound siderophores with confidence. Another potential candidate is porphyrins, as they are precursors to many biological molecules including chlorophyll and heme and is structurally very similar to corrins (Schneider and Stroiński 1987). For instance, cobalt can replace magnesium in chlorophyll within cyanobacteria and diatom cells or iron in protoporphyrin in E. coli (Csatorday et al. 1984; El-Sheekh et al. 2003; Majtan et al. 2011), but these studies used cobalt concentrations that are

several orders of magnitude higher than what is observed in natural seawater. This may suggest that the binding strength of cobalt to these organic compounds is lower than those of other metals, and that cobalt substitution may not be common (or spontaneous) in the ocean. Future studies that evaluate the binding strength of cobalt and other transition metals to porphyrins and related compounds may provide additional insight on whether these compounds can act as cobalt ligands.

3.5 CONCLUSIONS

Evidence from cobalamin quotas and transcriptome analysis suggest that while cobalamins are actively produced and recycled across this study transect, microbial communities may be potentially experiencing more cobalamin (or cobalt) limitation at higher latitudes despite a relatively constant dissolved cobalt pool with latitude. This may suggest that the composition of cobalt-binding ligands may vary latitudinally, with the amount of biologically available cobalt decreasing with increasing latitude. Therefore, further characterization of cobalt ligands is necessary to understand how the bioavailability of cobalt affects the cobalt nutritional status of the in situ microbial community. While we did not identify cobalamin-related compounds in the dissolved cobalt pool, this may be due to limitations in MS libraries and low volumes of sampled seawater. Future studies on cobalamin degradation products or other potential cobalt-binding ligand candidates may help us to further identify components of the cobalt ligand pool in the ocean, and may provide helpful insight on the two-way interaction between cobalt speciation and microbial activity and composition.

3.6 ACKNOWLEDGMENTS

This work was supported by the Simons Foundation (426570 to R.M.B, E.V.A., and A.E.I.). T. Ugrai and L. Carlson provided technical support with data acquisition on the ICP-MS and the Q-Exactive respectively. J. McMillan, K. Cain and A. Hynes helped with flow cytometry analysis. We also thank the captain and crew of the R/V *Ka'imikai-O-Kanaloa* and R/V *Kilo Moana*.

3.7 FIGURES AND TABLES

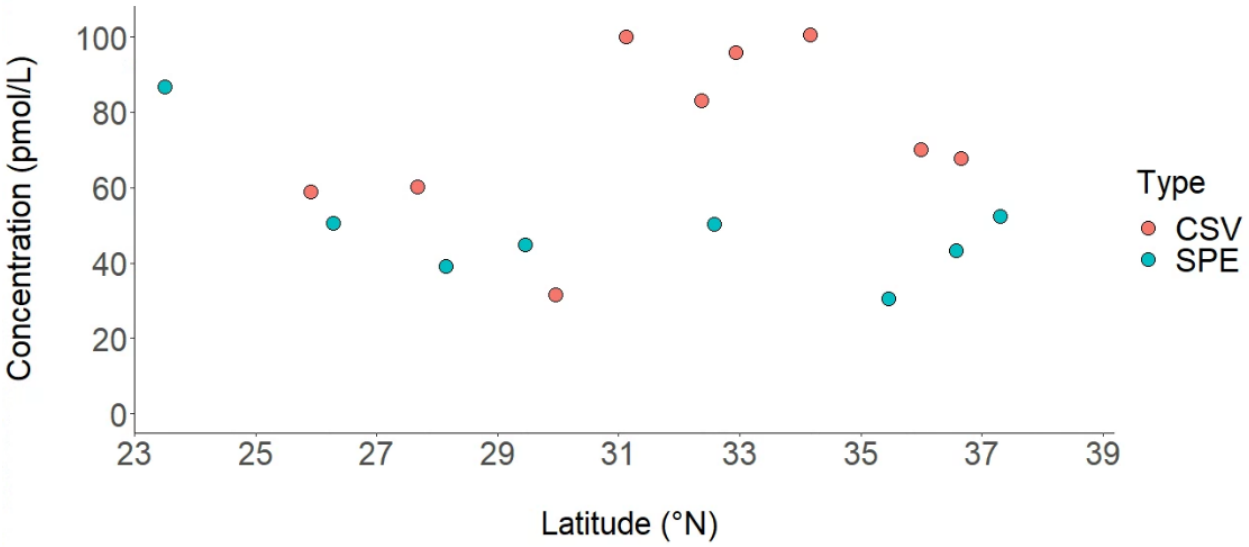

Figure 3.1 Dissolved Co concentrations from the Gradients 3 cruise (2019) measured by CSV (red) and Co ligand concentrations from the Gradients 1 cruise (2016) measured by LC-ICP-MS (blue).

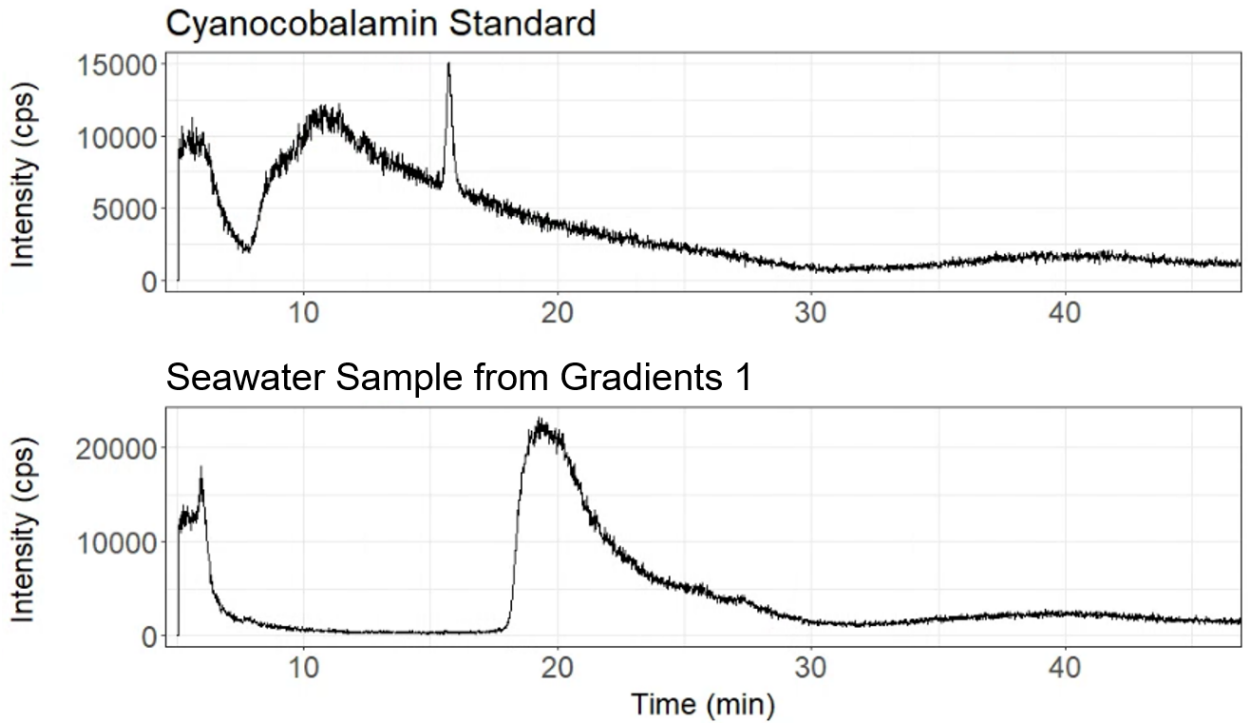

Figure 3.2 LC-ICP-MS chromatograms of ^{59}Co intensity of a cyanocobalamin standard (upper panel) and a SPE-column extracted seawater sample (bottom panel).

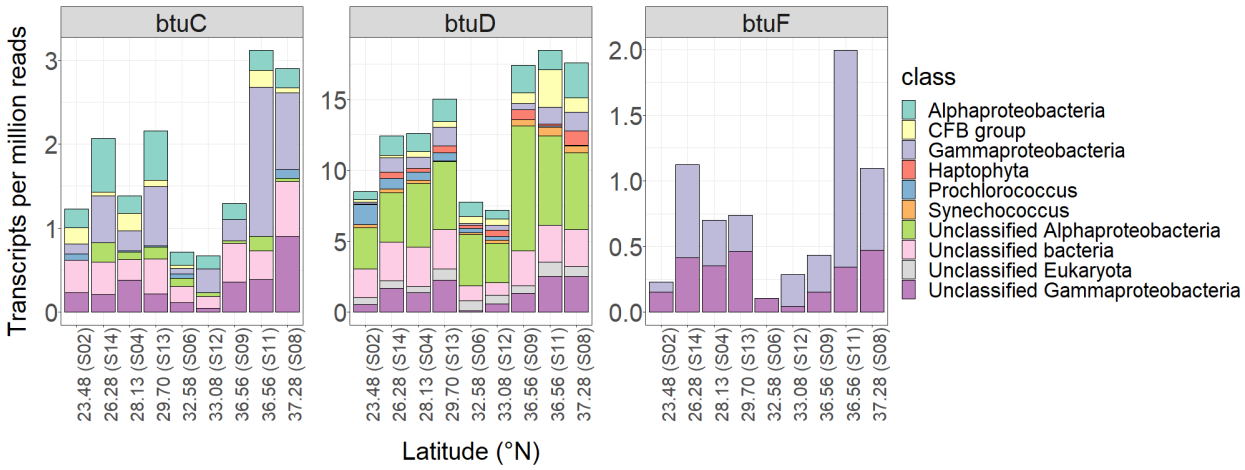

Figure 3.3 Mean abundances of cobalamin uptake-related transcripts across the study transect surface normalized to number of total short reads.

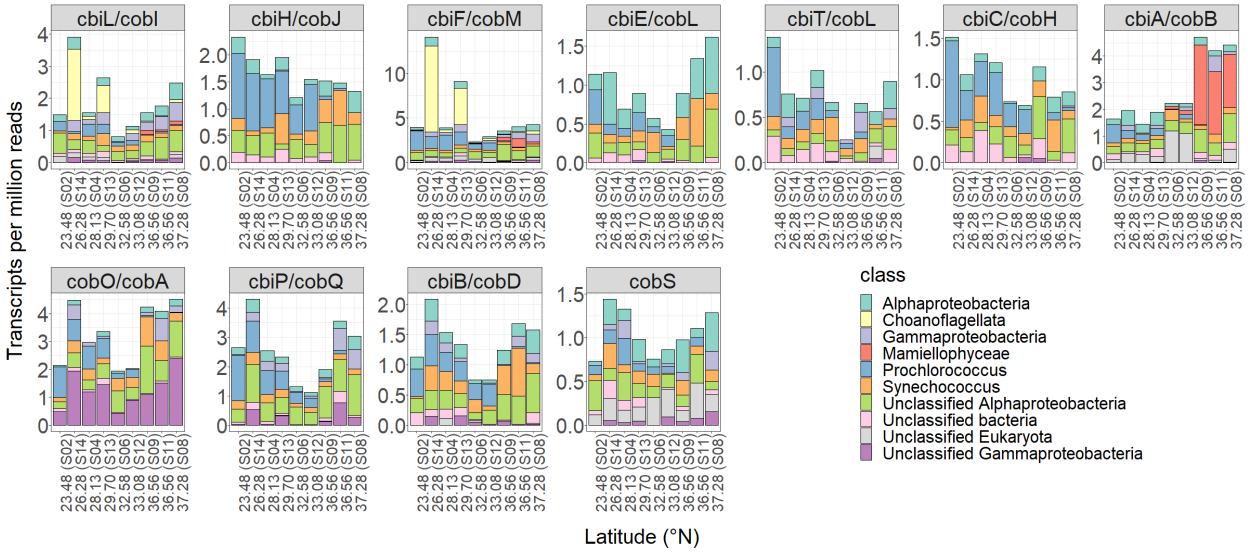

Figure 3.4 Mean abundances of cobalamin synthesis-related transcripts across the study transect surface normalized to number of total short reads. Seven panels in the upper row show genes in the "corrin ring synthesis" category, while four panels in the lower row show genes in the "final synthesis and repair" category.

Table 3.1 Particulate cobalamin and pseudocobalamin concentrations and estimated cellular quotas across the study transect ([1] from *Prochlorococcus* and *Synechococcus* biomass, [2] from POC measurements)

Latitude	Compound concentrations (pmol/L)				Pseudocobalamin cellular quota (nmol/mol C[1])	Particulate carbon (umol/L)	Particulate cobalamin : POC (nmol/mol[2])
	Pseudocobalamin		Cobalamin				
	average	stdev	average	stdev			
23.5	0.005	0.001	0.01	0.008	10	1.7	5.5
26.3	0.002	0.002	0.018	0	6.1	1.6	11.5
28.1	0.004	0.002	0.009	0.008	9.5	2.1	4.2
29.7	0.003	0.001	0.011	0.011	8.7	2.8	3.7
32.7	0.006	0.003	0.016	0.008	10.9	2.6	6.2
33.1	0.022	0	0.032	0.001	31.3	7.1	4.6
35.5	0.003	0	0.012	0.002	110.8	5	2.4
36.6	0.002	0.003	0.025	0.006	24.7	7.9	3.2

3.8 SUPPLEMENTAL FIGURES AND TABLES

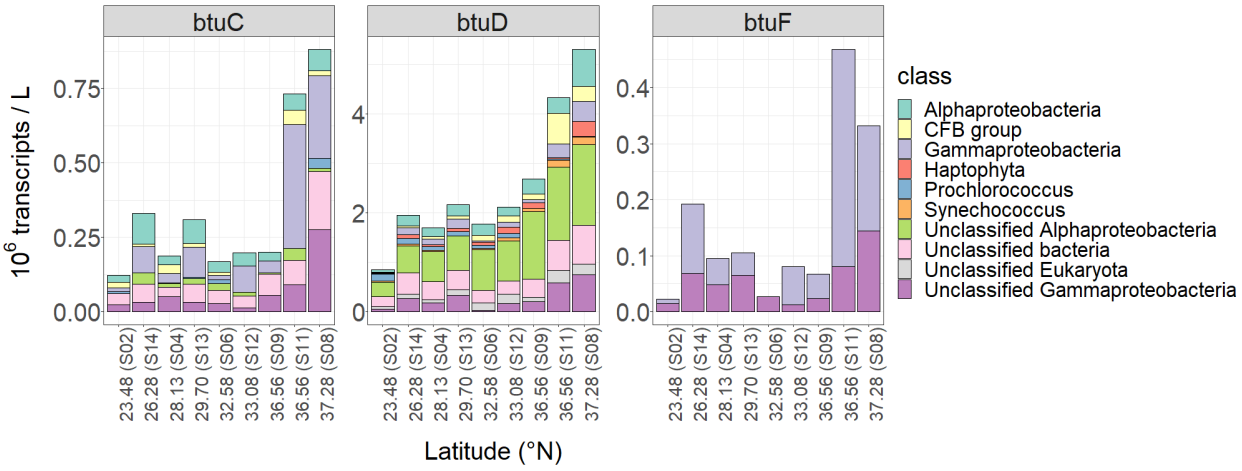

Supplementary Figure 3.1 Mean abundances of cobalamin uptake-related transcripts across the study transect surface in units of transcripts per liter.

Supplementary Table 3.1 Ranges of cobalamin and pseudocobalamin quotas reported in various studies. (References: a) Heal et al. 2017 b) Suffridge et al. 2017 c) Villegas-Mendoza et al. 2019)

Environment Type	Community type	Pseudocobalamin cellular quota (nmol/mol C)	Particulate cobalamin : POC (nmol/mol)
Environmental	this study	6-110	2.4-11.5
	North Pacific surface waters[a]	87	
	SPOT surface waters[b]		110 ± 184
Cultures	Multispecies marine bacteria from the California Current[c]		160
	Prochlorococcus[a]	130-1190	
	Synechococcus[a]	1480-3000	
	Dinoroseobacter[c]		120

Chapter 4. HYDROGEN AND CARBON ISOTOPE RESPONSES TO SALINITY IN GREENHOUSE-CULTIVATED MANGROVES

* This article was published in Organic Geochemistry, Volume 132, J. Park, S. N. Ladd and J. P. Sachs, Hydrogen and carbon isotope responses to salinity in greenhouse-cultivated mangroves, Pages 23-36, Copyright Elsevier (2019).

4.1 ABSTRACT

Paired hydrogen and carbon isotope ratios ($^{2}H/^{1}H$ and $^{13}C/^{12}C$) of mangrove lipids can be used to quantitatively reconstruct past salinity and $^{2}H/^{1}H$ ratios of environmental water, and in some cases precipitation rate. This approach is based on the observation that net ^{2}H- and ^{13}C-fractionation increases and decreases, respectively, with salinity of environmental water. In order to better understand the mechanisms underlying these empirical observations and ultimately improve estimates of paleoprecipitation from the paired H and C isotope approach, we analyzed the isotopic composition of fatty acids from five species of mangroves cultivated in salinity treatments of 5 to 30 ppt for 3.5 years in a greenhouse. Decreased net ^{13}C-fractionation with salinity in three mangrove species was attributed to increased water use efficiency and thus a ^{13}C-enriched internal CO_2 pool. Net ^{2}H-fractionation decreased with salinity in three mangrove species, opposite to previous observations of mangroves growing along salinity gradients in lakes and estuaries. The difference between uncultivated and greenhouse-cultivated mangroves may result from variability of $^{2}H/^{1}H$ of environmental water in natural environments. In addition, increased net ^{2}H-fractionation with salinity was potentially attributed to temporal variability in $^{2}H/^{1}H$ of leaf water and timing of lipid production, and the use of stored carbohydrates in seeds.

Due to the sensitivity of the salinity and ^{13}C-fractionation relationship for calculating both salinity and water isotopes, optimization of mangrove lipid H and C isotopes as a paleohydrologic tracer may be best achieved through lab-based calibrations of the relationship between ^{13}C-fractionation and salinity.

4.2 INTRODUCTION

The tropics play an important role in global climate, as tropical convection and ocean-atmosphere interaction affect Earth's radiation budget, global water cycle and precipitation patterns (Pierrehumbert 2000; Chiang 2009; Wohl et al. 2012). Current climate model simulations often disagree on future precipitation projections or do not reproduce recent rainfall estimates that agree with observations, and they could be potentially improved with long-term rainfall data from paleo-precipitation proxies (Zhang et al. 2007; Flato et al. 2013; Sun et al. 2017). These proxies include tropical corals, tree rings, ice cores from alpine glaciers and marine sediment cores, but these do not provide high resolution, long-term and continuous records of precipitation in the tropics that span sub-millennial to millennial timescales (Fairbanks et al. 1997; Greer and Swart 2006; Pfeiffer et al. 2006).

A promising proxy of past tropical hydroclimate is the hydrogen isotope composition of lipids ($\delta^2H = ((^2H/^1H_{sample})/(^2H/^1H_{VSMOW}) - 1)$ (‰)) produced by photoautotrophs and preserved in organic-rich lake and swamp sediments, as such sediment can provide continuous, high-resolution records on millennial timescales. δ^2H values of cyanobacterial and algal lipids are strongly correlated with δ^2H values of source environmental water (δ^2H_{water}), both in field- and laboratory-based studies (Sauer et al. 2001; Huang et al. 2004; Englebrecht and Sachs 2005; Zhang and Sachs 2007; Maloney et al. 2016). Similarly, δ^2H values of long-chained *n*-alkanes

and *n*-alkanoic acids produced as leaf waxes by vascular plants are also correlated with $\delta^2H_{precipitation}$ (Sachse et al. 2004; Polissar and Freeman 2010; Guenther et al. 2013; Tipple and Pagani 2013). Because δ^2H values of environmental water are strongly correlated with precipitation rate over seasonal or longer timescale in the tropics (Dansgaard 1964; Bony et al. 2008; Risi et al. 2008), δ^2H_{water} values derived from measurements of δ^2H_{lipid} of biomarkers from photosynthetic organisms can be used to calculate precipitation rate in the tropics (Smittenberg et al. 2011).

However, calculating δ^2H_{water} values (and ultimately precipitation rates) is complicated by other factors that affect δ^2H_{lipid} values. In phytoplankton, δ^2H_{lipid} values can be affected by temperature, salinity, light availability, biosynthetic pathway, growth rate, growth phase and source organism (Schouten et al. 2006; Zhang and Sachs 2007; Wolhowe et al. 2009; Zhang et al. 2009b; Nelson and Sachs 2014; Heinzelmann et al. 2015a; b; Sachs and Kawka 2015; van der Meer et al. 2015; Sachs et al. 2017; Ladd et al. 2018). Similarly, δ^2H_{lipid} values of vascular plants (including mangroves) can be affected by temperature, relative humidity, salinity, light intensity, timing of lipid synthesis and evapotranspiration (Smith and Freeman 2006; Yang et al. 2009; Feakins and Sessions 2010; Kahmen et al. 2011a, 2013; Douglas et al. 2012; Sachse et al. 2012; Tipple et al. 2013; Ladd and Sachs 2015a; b). Despite these complications, several studies have qualitatively reconstructed local precipitation in the tropics by a multi-proxy approach including δ^2H_{lipid} values from tropical lake and marine sediments (Schefuß et al. 2005; Pahnke et al. 2007; Tierney et al. 2008; Sachs et al. 2009; Niedermeyer et al. 2010; Smittenberg et al. 2011; Konecky et al. 2013; Atwood and Sachs 2014; Zhang et al. 2014; Richey and Sachs 2016; Arnold et al. 2018).

The application of leaf wax δ^2H_{lipid} values as a precipitation proxy in coastal tropical and subtropical regions can be complicated by the strong influence of salinity on hydrogen isotope fractionation in halophilic plant leaf waxes. About a third of organic matter in tropical and subtropical coastal sediments are produced by leaf litter from mangroves, which are halophilic trees and shrubs that grow widely in the intertidal zones in the tropics and subtropics (Jennerjahn and Ittekkot 2002; Giri et al. 2011; Alongi and Mukhopadhyay 2015). The net fractionation factor for ^2H between mangrove leaf lipids and source water (expressed as $\alpha^2H_{lipid\text{-}water} = (\delta^2H_{lipid} + 1000) / (\delta^2H_{water} + 1000)$) decreases with salinity for alkanes (0.7–1.8‰ / ppt) and triterpenoids (0.5–0.9‰ /ppt) in diverse genera of mangroves (*Avicennia, Rhizophora, Bruguiera, Laguncularia*) in tropical and subtropical estuaries and lakes from the western Pacific and from Florida (Ladd and Sachs 2012, 2013, 2015a; b, 2017; He et al. 2017). This suggests that if past salinity and water isotopes were to be reconstructed using δ^2H_{lipid} values, the salinity effect can be corrected if lipids were specifically derived from mangrove trees. In contrast, using δ^2H_{lipid} values from generic leaf wax compounds such as long chain *n*-alkanes may be problematic, since these could come from mixed mangrove/non-mangrove sources and have different responses to changing precipitation rates than mangrove-sourced *n*-alkanes.

The pentacyclic triterpenoid taraxerol is particularly useful as a mangrove specific biomarker, as it is produced in high amounts by *Rhizophora* spp. mangroves and is well preserved in sediments with minimal diagenetic alteration (Versteegh et al. 2004; Koch et al. 2005). $\delta^2H_{taraxerol}$ values are influenced by both salinity and δ^2H_{water} values, so they cannot be used on their own to estimate precipitation rate, but rather need to be paired with δ^2H values of algal lipids that grew in the same environment with the mangroves (as in Nelson and Sachs (2016). δ^2H values of algal lipids are also strongly influenced by salinity, but in the opposite way

as in mangroves, as $\alpha^2H_{lipid\text{-}water}$ in microalgae increases with salinity by 0.7-1.7‰ / ppt (Schouten et al. 2006; Sachse and Sachs 2008; Sachs and Schwab 2011; Chivall et al. 2014; M'boule et al. 2014; Nelson and Sachs 2014; Heinzelmann et al. 2015a; Maloney et al. 2016; Sachs et al. 2016). Therefore, using the two independent linear relationships between $\alpha^2H_{lipid\text{-}water}$ and salinity from both mangrove and algal lipids, salinity and δ^2H_{water} can be calculated (Ladd and Sachs 2012; Nelson and Sachs 2016).

A second possible approach to estimate salinity and δ^2H_{water} is to couple δ^2H and $\delta^{13}C$ measurements from the same mangrove leaf lipids (Ladd and Sachs 2013). Since net $^{13}C/^{12}C$ fractionation between mangrove leaf lipids and atmospheric CO_2 ($\alpha^{13}C_{lipid\text{-}atm}$) decreases with salinity by 0.2‰ / ppt for alkanes in *Avicennia marina* mangroves, salinity and δ^2H of environmental water can be calculated from the linear relationships between α^2H or $\alpha^{13}C$ and salinity (Ladd and Sachs 2013). This paired δ^2H/ $\delta^{13}C$ approach can be improved by reducing the uncertainties in the relationship between $\alpha^{13}C_{lipid\text{-}atm}$ and salinity, as it is less well-constrained than the relationship between α^2H and salinity, which has been established across different lipids and mangrove taxa (Ladd and Sachs 2012, 2013, 2015a; b, 2017; He et al. 2017).

Another way to improve the accuracy of mangrove-lipid-derived salinity and δ^2H_{water} estimates is to better understand the mechanisms that relate $\alpha^2H_{lipid\text{-}water}$ and $\alpha^{13}C_{lipid\text{-}atm}$ with salinity. The relationship between $\alpha^{13}C_{lipid\text{-}atm}$ and salinity has been attributed to higher water use efficiency (WUE) with increasing salinity and increased $^{13}CO_2$ fixation, responses observed in both salt-tolerant and salt-sensitive plants (Farquhar et al. 1982; Brugnoli et al. 1991; Lin and Sternberg 1992; Sobrado 1999; Rivelli et al. 2002; Jiang et al. 2006). The underlying mechanisms accounting for the relationship between $\alpha^2H_{lipid\text{-}water}$ and salinity, however, are less evident. The negative α^2H – salinity relationship has been attributed to variable biosynthetic

fractionation between lipids and leaf water (the direct source of hydrogen in lipids from dicots), which may be caused by differences in NADPH sources or reliance on stored carbohydrates, and variable timing of leaf or lipid production (Ladd and Sachs 2015a; b). However, in the case of *B. gymnorhiza* growing in marine lakes in Palau, biosynthetic fractionation did not vary with salinity, suggesting instead that the α^2H – salinity relationship could result from a greater contribution of ^2H-depleted water vapor to leaf water in a humid climate as salinity increases (Ladd and Sachs 2017). A better understanding of these mechanisms would facilitate the use of mangrove leaf lipid δ^2H measurements to reconstruct precipitation rates.

To improve the calibration of the relationship between mangrove leaf $\alpha^{13}C_{lipid\text{-}atm}$ and salinity by reducing uncertainty in the regression statistics, and to assess potential mechanisms causing the inverse relationship between mangrove leaf $\alpha^2H_{lipid\text{-}water}$ and salinity, five species of mangroves that employed different salt management strategies (Table 4.1) were cultivated in the University of Washington greenhouse for 3.5 years at 6 different salinity levels (5, 10, 15, 20, 25, 30 ppt). The δ^2H and $\delta^{13}C$ values of leaf wax fatty acids were measured along with the δ^2H values of growth water and the $\delta^{13}C$ values of bulk leaves.

4.3 METHODS

4.3.1 *Cultivation of mangroves in greenhouse*

4.3.1.1 Cultivated species and greenhouse growth conditions

We cultivated 5 species of mangroves (*Avicennia germinans*, *Laguncularia racemosa*, *Rhizophora apiculata*, *Rhizophora mangle*, and *Xylocarpus granatum*), each of which relies on different mechanisms to cope with salt stress at 6 salinity levels (5, 10, 15, 20, 25, 30 ppt) in the Botany greenhouse at the University of Washington in Seattle. Seeds and propagules of *A.*

germinans, L. racemosa and *R. mangle* were ordered from Florida Plants (Broward Co., FL), while seeds of *R. apiculata* and *X. granatum* were collected during fieldwork on the islands of Pohnpei and Kosrae, Federated States of Micronesia. 40–50 seeds or propagules from each species were germinated in water with salinity of 5 ppt during September to November 2012, then transferred to 1 gallon pots filled with sand in the greenhouse during October to December 2012. All pots were initially supplied with 5 ppt or 10 ppt salt water, then moved to water with higher salinity after every 4-5 days to help plants adjust to changes in salinity. A water pump pumped and drained water in the tub to a set level above the pots twice every day to simulate a mock tidal cycle. A fertilizer solution (10 mL of Peter's Plant Food solid with 1 L water) was added to all plants weekly. In the greenhouse, temperature ranged between 15.5 ℃ and 23 ℃, relative humidity ranged between 25% and 90%, and light levels between October and April were supplemented by P.L. Light system (600W). While temperature and relative humidity are expected to be higher in humid tropical climates where these mangrove species grow naturally, field conditions could not be more closely simulated due to other experiments that were conducted in the greenhouse at the same time. Because about half of *R. apiculata* were not growing well, additional *R. apiculata* from Kosrae were added in September 2013, and *R. apiculata* in poor health were removed between November 2013 and January 2014.

4.3.1.2 Tub water salinity and δ^2H maintenance

Salt water was produced by adding Instant Ocean Sea Salt to tap water. Salinity was monitored daily with a conductivity probe (Amprobe WT-60), and 2-3 L of tap water was added whenever evaporation caused salinity to increase by 0.5 ppt.

In January 2013 it was observed that the tub water isotopes had become enriched relative to the starting tap water. To counteract evaporative enrichment, after this point 10 L of water in

each tub was replaced with 10 L of fresh salt water (δ^2H = –70‰) every week to maintain relatively constant δ^2H_{water} = ~ –50‰ over time across all salinity tubs, and tub water samples for δ^2H measurements were collected weekly before and after water replacement.

4.3.1.3 Harvest

In order to monitor isotopic variability in leaves over time, one leaf from each *R. mangle* tree was collected and placed into a plastic bag (WhirlPak, Hach, CO, USA) in July 2014 and stored in a freezer at -20 °C until further analysis. In March 2016 all trees were completely harvested. For each plant, plant mass above the sand surface, wet root mass and dry root mass was recorded. Leaves were cut off from stem, placed in plastic bags and stored at –20 °C. Roots were cleaned with water, dried in the oven overnight and stored at –20 °C.

Development of mangrove seedlings in the greenhouse may have been constrained by temperature and pot size. The temperature range in the greenhouse was lower than that of typical mangrove habitats (20-30 °C), which may have subjected trees to cold stress (Duke 2006). Limited pot size can also constrain root growth, resulting in reduced photosynthesis and plant biomass (Arp 1991; Kasai et al. 2012; Poorter et al. 2012). In addition, placing plants inside pots itself can significantly affect root morphology, reducing capability of the roots to take up water efficiently (NeSmith and Duval 1998).

4.3.2 *Extraction and purification of lipids from leaves*

For each species, from the group of trees grown in same salinity treatments, two or three trees with healthy-looking leaves were selected. Strips of 2 to 4 leaves along the midrib from the same tree were freeze-dried and ground together to average out isotopic heterogeneity among

leaves or across the base and tip of a single leaf. Total lipid extracts were extracted by Accelerated Solvent Extraction (ASE) following methods previously described by Ladd and Sachs (2015b). The resulting total lipid extract from all species except *R. mangle* was saponified to separate fatty acids and neutral compounds (including alkanes and sterols). Each dry sample was incubated at 70 °C for 3 hours after adding 3 mL of 1 N KOH/MeOH and 2 mL HPLC-grade H_2O and cooled to room temperature. 2 mL hexane was added to the saponified samples and vortexed, and the organic phase (containing neutral compounds) was transferred to new vials. After 4-5 hexane rinses, 15-20 drops of 4 N HCl was added to the saponified samples to decrease pH below 2. Then, 2 mL hexane was added 4-5 times to the acidic saponified samples and vortexed, and the organic phase (containing protonated fatty acids) was transferred to new vials. For *R. mangle*, in order to separate alkanes and triterpenoids from other types of neutral compounds, the lipid extracts were purified using column chromatography methods previously described by Ladd and Sachs (2015b).

A 2% aliquot of fatty acids and alcohols from all species was silylated by adding 20 μL pyridine and 20 μL BSTFA at 60 °C for an hour. Lipid composition was identified by Gas Chromatography - Mass Spectrometry (GC-MS) with an Agilent (Santa Clara, CA, USA) 6890N gas chromatograph with an Agilent 5975 quadrupole mass selective detector and an Agilent DB-5 column (60 m × 0.25 mm × 0.25 μm) with helium as the carrier gas (1.1 mL/ min flow). The GC was heated initially to 100 °C for 2.1 min, then at 5 °C/ min to 320 °C for 23.9 min. Compounds were identified based on retention times and comparisons with published mass spectra.

50% of the remaining 98% of the acid fraction was methylated with the methylating agent prepared by adding 5 mL of acetyl chloride to 50 mL of anhydrous methanol chilled in an ice

bath. 1 mL dry hexane and 2 mL methylating agent was added to each sample, vortex-mixed and heated in an oven at 60 °C for 24 hours. After cooling samples to room temperature, 2 mL HPLC-grade H_2O and 2 mL hexane were added, vortex-mixed and separated 3 times. 50% of the remaining 98% of the sterol fraction from *R. mangle* leaves was acetylated by adding 20 μL pyridine and 20 μL acetic anhydride with known δ^2H composition at 70 °C for 30 minutes. 5- α-cholestane was added as a quantification standard to 25–75% aliquots of methylated samples. The samples were quantified on a GC (Agilent (Santa Clara, CA, USA) 6890N gas chromatograph) with Flame Ionization Detector (GC-FID) and an Agilent VF-17ms column (60 m × 0.25 mm × 0.25 um) with helium (1.4 mL/ min) as the carrier gas. The GC was heated initially to 100 °C for 2.1 min, then at 5 °C/ min to 320 °C where it was held for 23.9 min.

The saponification, isolation, and derivatization of fatty acids as described does not result in detectable isotope fractionation (Zhang and Sachs 2007; Smittenberg et al. 2011; Sachs and Kawka 2015; Sachs et al. 2016, 2017, 2018).

4.3.3 *Lipid δ^2H and $\delta^{13}C$ analysis*

Fatty acid samples from all five mangrove species were diluted with toluene to a concentration of ~150 ng/ μL (for δ^2H analyses) or ~40 ng/ μL (for $\delta^{13}C$ analyses) prior to measurement by Gas Chromatography - Isotope Ratio Mass Spectrometry (GC-IRMS) at the University of Washington on equipment described previously (Ladd and Sachs 2015b). For fatty acid analysis, an Agilent DB-5ms column (60 m × 0.25 mm × 0.25 μm) was used, with helium as the carrier gas (1.5 mL/ min flow). The GC was initially heated to 120 °C, then at 20 °C/ min to 180 °C, then at 3 °C/ min to 325 °C and held for 16 min. Alkanes and triterpenols from *R. mangle* were diluted to the same concentrations, and analyzed using an Agilent VF-17ms column

(60 m × 0.25mm × 0.25um) , also with helium as the carrier gas (1.1 mL/ min flow). The GC was initially heated to 120 °C, then at 20 °C/min to 260 °C, then at 1 °C/ min to 300 °C, and then at 20 °C/ min to 325 °C and held for 18.5 min. Each sample was injected three times for each isotope measurement.

Performance of the instrument was evaluated by running a mix of external standards ($C_{21, 23, 26, 28, 32, 34, 38}$ *n*-alkanes) after every 4 to 5 samples and co-injecting a mix of internal standards ($C_{26, 32, 38}$ *n*-alkanes) with each sample. All *n*-alkane isotopic reference standards and their δ^2H and $\delta^{13}C$ values were provided by A. Schimmelmann, University of Indiana. The average standard deviations of the external standards were 2.8‰ for δ^2H analyses and 0.26‰ for $\delta^{13}C$ analyses.

Raw δ^2H and $\delta^{13}C$ values from the instrument were corrected using Thermo ISODAT software V. 2.5 as described previously (Ladd and Sachs 2015b). Fatty acid δ^2H and $\delta^{13}C$ were corrected for methylation using a phthalic acid standard with known $\delta^2H = –95.5 \pm 2.2$‰ and $\delta^{13}C = –27.21 \pm 0.02$‰ (A. Schimmelmann, Indiana University, Bloomington, Indiana) that was methylated and measured in the same way as the fatty acid samples. The H_3^+ factor was determined at the start of each sequence, using pulses of a reference gas of varying heights, and was 1.66 ± 0.07 during November 2016 and March 2017 when *A. germinans, L. racemosa, R. apiculata* and *R. mangle* samples were analyzed, and 2.04 when *X. granatum* samples were analyzed in February 2018.

δ^2H values of triterpenols in leaves from 2014 and 2016 in each salinity treatment were averaged to calculate $\alpha^2H_{2016\text{-}2014} = (\delta^2H_{2016} + 1000)/ (\delta^2H_{2014} + 1000)$ in each salinity at each time, and fractionation factors between *R. mangle* lipids harvested in 2014 and 2016 were calculated with the equation $\varepsilon_{2016 - 2014} = (\alpha^2H_{2016\text{-}2014} - 1) \times 1000$ (‰) (Supplementary Table 4.3).

4.3.4 *Source water δ^2H analysis*

δ^2H values of tub water samples (δ^2H_{water}) collected between July 2014 and March 2016 were measured by Cavity Ring Down Spectroscopy following the methods described by Ladd and Sachs (2015b), and the average precision of the final three injections was 0.33‰ for δ^2H.

Fractionation factors of ^2H between lipids and environmental water ($\alpha^2H_{lipid\text{-}water}$) at harvest were calculated using the last two measured δ^2H_{water} values (from 2016 February and March) in order to represent as closely as possible the isotopic composition of water used to synthesize the leaf lipids, since fatty acids in plant leaf waxes are recycled every few days (Gao et al. 2012) and the δ^2H_{water} values increased over time (Supplementary Figure 4.1).

4.3.5 *Bulk leaf $\delta^{13}C$ analysis*

1 to 3 leaves from the same trees selected for lipid $\delta^{13}C$ analysis were dried in the oven at 60 °C for 24 hours, taken out and left outside for 24 hours to prevent over-drying and ground homogenously. ~4 mg of each leaf powder was enclosed in tin capsules and sent to the UC Davis Stable Isotope Facility for bulk leaf $\delta^{13}C$ analysis on a PDZ Europa ANCA-GSL elemental analyzer connected to a PDZ Europa 20-20 isotope ratio mass spectrometer (Sercon Ltd., Cheshire, UK). The samples were combusted in an oxidation reactor filled with chromium oxide and silver copper oxide at 1000 °C with helium flow, producing N_2, CO_2, water and oxides. To remove water and oxides these products went through a reduced copper reactor and a magnesium perchlorate water trap. CO_2 and N_2 were separated on a Carbosieve GC column (65 °C, 65 mL/ min) before entering the IRMS for isotope analysis.

4.3.6 *Leaf water model*

δ^2H values of leaf water (δ^2H_{lw}) were calculated using a Péclet-modified Craig Gordon model from Kahmen et al. (2011b), as described previously by Ladd and Sachs (2015a, 2017). The modeled δ^2H_{lw} values were used to compare the effect of salinity on δ^2H_{lw} in the greenhouse and to evaluate if the influence of salinity on δ^2H_{lw} can account for differences in δ^2H_{lipid} across a salinity gradient. Initially, a sensitivity test was performed with the leaf water model by calculating the range of δ^2H_{lw} values from end-member values of one variable at a time while holding the other variables constant. The range of temperature and relative humidity is as described in section 2.1.1., and the range of $\delta^2H_{atmospheric\ vapor}$ was determined from measurements with an isotopic water vapor analyzer (Los Gatos Research, San Jose, CA) during 2013 January. The range of stomatal conductance (g_s) (rate of water vapor loss, mol/ m^2/ s) encompasses published observations from *A. germinans, L. racemosa and R. mangle* leaves (Lin and Sternberg 1992; Sobrado 1999, 2000; Krauss and Allen 2003; Biber 2006). The range of effective path length (L, mm) was derived from published values in several species of mangroves (Ellsworth et al. 2013; Liang et al. 2018). The range of δ^2H values of xylem water (δ^2H_{xw}) was calculated using published $\alpha_{xw\text{-}sw}$ values (Ladd and Sachs 2015a) and measured δ^2H_{water} values, and accounts for the fractionation due to discrimination against ^2H at roots during water uptake that has been observed in mangroves (Lin and Sternberg 1993). As δ^2H_{water} values in the greenhouse were relatively stable (Supplementary Figure 4.1), and $\alpha_{xw\text{-}sw}$ decreases at high salinity (Lin and Sternberg 1993; Ladd and Sachs 2015a), δ^2H_{xw} values are expected to be ^2H-depleted at high salinity in our case.

Among the variables included in the model, stomatal conductance, $\delta^2H_{xylem\ water}$ and effective path length were identified to vary directly with salinity. We assessed the variation in δ^2H_{lw}

values from changes in these three factors across the 25 ppt salinity range, but did not account for species-specific differences in the factors, as the results of our sensitivity test suggested that the effects of species-specific variations in these variables are not as significant as effects from other variables common across species (Table 4.2; Supplementary Table 4.1). In our final calculations, g_s of *R. mangle* from Lin and Sternberg (1992) (0.35 mol/ m^2/ s at 5 ppt and 0.15 mol/ m^2/ s at 30 ppt) was used. L at 5 and 30 ppt were estimated using the inverse relationship between L and transpiration rate (Song et al. 2013), where the transpiration rate at each salinity was calculated from the g_s values above. δ^2H_{lw} values at 5 ppt and 30 ppt were calculated with the leaf water model using end-members of these three variables while keeping other variables constant (Table 4.3).

In addition, to assess the diurnal isotopic variability of leaf water, different "daytime" and "nighttime" temperature, relative humidity and atmospheric vapor δ^2H values (Table 4.4) were used to calculate daytime and nighttime δ^2H_{lw} values. A daytime temperature of 21 °C and a nighttime temperature of 17 °C were employed for this calculation. Relative humidity was estimated using water vapor content and saturated vapor pressure calculated from temperature.

An estimate of uncertainty for modeled δ^2H_{lw} values was derived from a Monte Carlo approach with 1000 iterations that included the uncertainties for all model variables.

4.3.7 *Statistical Analysis*

Simple ordinary least square regression was used to calculate the correlations between δ^2H, $\delta^{13}C$ or $\alpha^2H_{lipid\text{-}water}$ and salinity. In addition, to account for different magnitude of standard errors in the triplicate δ^2H and $\delta^{13}C$ measurements, using a dummy data point ($\delta^2H = -100 \pm 5‰$, $\delta^{13}C = -30 \pm 0.3‰$), a 1000 iteration Monte Carlo analysis with normally distributed errors from δ^2H

and $\delta^{13}C$ standard errors was conducted to calculate slopes, intercepts and associated uncertainties.

4.4 RESULTS

4.4.1 *Relationship between salinity and $\delta^{13}C_{fatty\ acid}$*

Out of five species, three (*L. racemosa*, *R. apiculata* and *X. granatum*) had significant ($p < 0.05$) positive correlations between salinity and $\delta^{13}C_{fatty\ acid}$ ($R^2 = 0.51$ for *L. racemosa n*-C_{18}, 0.45 for *R. apiculata n*-C_{16}, 0.69 for *R. apiculata n*-C_{18}, 0.35 for *X. granatum n*-C_{16} and 0.36 for *X. granatum n*-C_{18}) (Figure 4.1; Table 4.5). Slopes of the relationship between salinity and $\delta^{13}C_{fatty\ acid}$ calculated from ordinary least square regression were similar in *L. racemosa* and *R. apiculata* (0.123 ± 0.008 for *R. apiculata n*-C_{16}, 0.207 ± 0.009 for *R. apiculata n*-C_{18}, 0.207 ± 0.009 for *L. racemosa n*-C_{18}), while slopes from *X. granatum* were about half as steep (0.086 ± 0.006 for *n*-C_{16}, 0.095 ± 0.009 for *n*-C_{18}). Fatty acids from *X. granatum* (–38.1 ± 1.4‰) were more depleted than fatty acids from *L. racemosa* and *R. apiculata* (each –34.1 ± 2.3‰ and –33.3 ± 1.9‰) (Supplementary Table 4.2). In contrast, the other two species (*A. germinans* and *R. mangle*) did not have significant relationships between salinity and $\delta^{13}C_{fatty\ acid}$.

4.4.2 *Relationship between salinity and $\delta^{13}C_{bulk\ leaf}$*

A significant positive correlation ($p < 0.05$) between salinity and $\delta^{13}C_{bulk\ leaf}$ was observed in *L. racemosa* ($R^2 = 0.90$), *R. apiculata* ($R^2 = 0.74$) and *X. granatum* ($R^2 = 0.56$) (Figure 4.2; Table 4.6). Slopes of the relationship calculated from ordinary least square regression were of a similar order to the slopes of salinity vs $\delta^{13}C_{fatty\ acid}$ (0.164 ± 0.020 for *L. racemosa*, 0.220 ± 0.034 for *R. apiculata* and 0.101 ± 0.021 for *X. granatum*). *R. mangle* showed a significant negative

correlation between salinity and $\delta^{13}C_{bulk\ leaf}$ ($p = 0.032$, $R^2 = 0.26$, $m = -0.070 \pm 0.030$), while *A. germinans* did not show a significant correlation ($p = 0.555$).

4.4.3 *Relationship between salinity and $\delta^2H_{fatty\ acid}$*

Three of the five species (*R. apiculata*, *R. mangle* and *X. granatum*) displayed significant ($p<0.05$) correlations between salinity and $\delta^2H_{fatty\ acid}$ (Figure 4.3; Table 4.5). In all three, $\delta^2H_{fatty\ acid}$ values were positively correlated with salinity ($R^2 = 0.48$ for *R. apiculata n*-C_{16}, 0.31 for *R. apiculata n*-C_{18}, 0.39 for *R. mangle n*-C_{16} and 0.22 for *X. granatum n*-C_{18}). The slopes of the relationships between salinity and $\delta^2H_{fatty\ acid}$ calculated from ordinary least square regression were greater in *R. apiculata* (1.253 ± 0.113 and 1.179 ± 0.113 each for *n*-C_{16} and *n*-C_{18} fatty acids) than in either *R. mangle* (0.474 ± 0.142 for *n*-C_{16} fatty acid) or *X. granatum* (0.529 ± 0.060 for *n*-C_{18} fatty acid). $\delta^2H_{fatty\ acid}$ values from *R. apiculata* were between -88 ± 14‰ (*n*-C_{16}) and -74 ± 16‰ (*n*-C_{18}), which were generally more depleted than fatty acids from *R. mangle* (-81 ± 7‰ for *n*-C_{16}) or from *X. granatum* (-85 ± 7‰ for *n*-C_{18}) (Supplementary Table 4.2).

$\alpha^2H_{lipid\text{-}water}$ values were also positively correlated with salinity for *R. apiculata* and *R. mangle* ($R^2 = 0.48$ for *R. apiculata n*-C_{16}, 0.31 for *R. apiculata n*-C_{18}, and 0.36 for *R. mangle n*-C_{16}), but the correlation was not significant in *X. granatum* ($p = 0.105$) (Figure 4.4; Table 4.5). Lipids from the other two species (*A. germinans* and *L. racemosa*) did not display significant relationships between either $\delta^2H_{fatty\ acid}$ and salinity or $\alpha^2H_{lipid\text{-}water}$ and salinity.

4.4.4 *Leaf water model results*

Results of the sensitivity test show that modeled δ^2H_{lw} values are more sensitive to changes in δ^2H_{vapor} values, relative humidity and temperature, than they are to changes in stomatal conductance and effective path length (Table 4.2).

As salinity increased from 5 ppt to 30 ppt, stomatal conductance was estimated to decrease from 0.35 mol/ m^2/ s to 0.15 mol/ m^2/ s (Lin and Sternberg 1992), δ^2H_{xw} values were estimated to be ^{2}H-depleted by 7.6‰, and path length was estimated to increase from 120 mm to 280 mm. These variables ultimately resulted in modeled δ^2H_{lw} values that are depleted by 2.7‰ at 30 ppt relative to 5 ppt (Table 4.3). δ^2H_{lw} values were more depleted under daytime conditions (–42.2 ± 3.4‰) than under nighttime conditions (–25.9 ± 2.8‰).

4.4.5 *$\delta^2H_{triterpenoids}$ in R. mangle leaves harvested in 2014 and 2016*

δ^2H values of three triterpenoids (taraxerol, β-amyrin and lupeol) were more ^{2}H-depleted in 2016 than in 2014 in 15 of 18 *R. mangle* treatments (Figure 4.5; Supplementary Table 4.2). There were no statistically significant relationships (at $p < 0.05$) between salinity and $\delta^2H_{triterpenoids}$ of *R. mangle* harvested in either year, or between salinity and $\varepsilon_{2016-2014}$ for any of the three triterpenoids (Supplementary Table 4.1).

4.5 DISCUSSION

4.5.1 *Relationships between salinity and $\delta^{13}C_{fatty\ acid}$ of cultivated mangroves*

4.5.1.1 Effect of water use efficiency on $\delta^{13}C_{fatty\ acid}$ and $\delta^{13}C_{bulk\ leaf}$

The significant positive correlation between $\delta^{13}C_{bulk\ leaf}$ values and salinity of cultivated *L. racemosa, R. apiculata* and *X. granatum* observed in this study (Table 4.6) is consistent with past studies (Farquhar et al., 1982; Sobrado, 2000a; Ladd and Sachs, 2013). This has been attributed to increased WUE at high salinity, which results in limited exchange of CO_2 between the

atmosphere and the intercellular air space under high salinity treatments and more incorporation of ^{13}C into leaf lipids from a ^{13}C-enriched internal CO_2 pool (Farquhar et al. 1982, 1989).

Generally, the observed correlation between $\delta^{13}C_{bulk\ leaf}$ and salinity (R^2 range 0.56-0.90) is stronger than that between $\delta^{13}C_{fatty\ acid}$ and salinity (R^2 range 0.35-0.69) (Table 4.5; Table 4.6). The correlation between $\delta^{13}C_{bulk\ leaf}$ and salinity in greenhouse-cultivated trees is also much higher than that in uncultivated trees (Ladd and Sachs 2013). This strong relationship may have resulted from the nitrogen fertilizer we supplied to the greenhouse-cultivated mangroves. Martin et al. (2010) observed that N-fertilized *A. marina* have higher WUE than trees without fertilizer, possibly because the additional nitrogen was allocated to Rubisco to keep up with high carbon assimilation rates. Since the greenhouse-cultivated trees were supplied with nitrogen fertilizers throughout their growth, it may be possible that greenhouse-cultivated trees had higher WUE and reduced intercellular CO_2 concentration relative to uncultivated trees, resulting in a relatively strong positive trend between salinity and $\delta^{13}C_{bulk\ leaf}$ values.

There were no significant correlations between salinity and $\delta^{13}C_{fatty\ acid}$ or $\delta^{13}C_{bulk\ leaf}$ in *A. germinans* and *R. mangle*. These two species are highly salt-tolerant, and maintain high WUE across wide ranges of salinity (Reef and Lovelock 2015). If these species can lower water potential by efficiently secreting through salt glands (*A. germinans*) or accumulating solutes in cytoplasm (*A. germinans* and *R. mangle*) (Table 4.1), they may rely relatively less on stomatal opening and closure to minimize water loss. However, while mangrove species with salt glands (*Aegiceras corniculatum, Aegialitis annulata, A. marina*) have been observed to lack relationships between salinity and $\delta^{13}C_{bulk\ leaf}$ (Guy et al. 1989), some of the same species (*A. corniculatum* and *A. marina*) have also been observed to have lower stomatal conductance and carbon assimilation rate with increasing salinity, despite high solute concentrations in their

leaves (Ball and Farquhar 1984). Therefore, while the lack of correlation between salinity and $\delta^{13}C_{fatty\ acid}$ or $\delta^{13}C_{bulk\ leaf}$ values suggests that *A. germinans* and *R. mangle* may adjust their water potentials by excluding excess salt rather than limiting water loss through the stomata, additional studies are required to establish the significance of these salt exclusion strategies in maintaining high WUE.

4.5.1.2 Plant growth correlated with salinity and $\delta^{13}C_{fatty\ acid}$

Dry root mass and wet plant mass are good measures of halophilic plant growth. With increasing salinity, halophilic plants increase root mass to obtain water, reinforce cell-wall lignification to limit salt absorption (Cheng et al. 2012; Vovides et al. 2014), and decrease stomatal conductance and carbon assimilation rates (Ball and Farquhar 1984); therefore, plants under high salt stress are expected to have higher dry root mass and lower wet plant mass. In our study, *L. racemosa* and *X. granatum* displayed a decrease in total wet mass as salinity increased (Supplementary Figure 4.2), implying that growth was suppressed at high salinity. This observation is consistent with the suggestion above that these species decrease their stomatal conductance to increase WUE, and further supports the explanation that WUE is primarily responsible for the positive correlation between salinity and $\delta^{13}C_{bulk\ leaf}$. Meanwhile, dry root mass of all five species decreased or did not change significantly with increasing salinity (Supplementary Figure 4.3), which may suggest that factors other than salinity, such as lower temperature and relative humidity or limited pot size, may have had larger influences on the growth of greenhouse-cultivated mangroves. However, as environmental factors in the greenhouse other than salinity were equally imposed on all plants, carbon isotope fractionation observed in fatty acids and bulk lipids in greenhouse-cultivated mangroves is likely controlled by increased WUE in response to salinity.

Nevertheless, given that the positive correlations between $\delta^{13}C_{lipid}$ and salinity in three different species of cultivated mangroves (*L. racemosa*, *R. apiculata* and *X. granatum*) were similar to that in the field (Ladd and Sachs 2013), incorporating a larger set of greenhouse-cultivated and uncultivated samples may help to decrease uncertainty in the relationship between $\alpha^{13}C$ and salinity for some mangrove species.

4.5.2 *Relationships between salinity and $\delta^2H_{fatty\ acid}$ of greenhouse mangroves*

4.5.2.1 Differing trends among cultivated and uncultivated mangroves

Field studies have documented negative correlations between salinity and $\alpha^2H_{lipid\text{-}water}$ of various lipids (including *n*-C_{29} and *n*-C_{31} alkanes, taraxerol, stigmasterol, and β-sitosterol) from different mangrove species in diverse settings, including lakes and estuaries in Australia, Palau, Micronesia, and Florida (Ladd and Sachs 2012, 2015a; b, 2017; He et al. 2017). These published results differ from the positive correlations observed in greenhouse-cultivated *R. apiculata* and *R. mangle* in this study (Figure 4.4; Table 4.5). The discrepancy may be due to differences in environmental parameters between the field and the greenhouse, such as δ^2H_{water}, or to different responses of individual lipid compounds to salinity (Ladd and Sachs 2012, 2015a; b, 2017; He et al. 2017).

A major difference between field and greenhouse settings is that there are alternate fresh or less-saline water sources that may be utilized by trees in the field. Several studies have proposed that mangroves opportunistically take up fresh or less-saline water through their roots during precipitation events (Lambs et al. 2008; Wei et al. 2013; Santini et al. 2015) or from groundwater (Sternberg and Swart 1987; Ewe et al. 2007), or through their leaves when wetted by rain or dew (Reef and Lovelock 2015; Steppe et al. 2018). Hydrogen and oxygen isotope mixing models

have been used to determine quantitative contributions of different water sources, such as soil water, groundwater, and rainwater. Studies estimated that scrub *A. marina* use 37–93 % rainwater, *R. stylosa* use 21–41% groundwater and 14–20% dew and *L. racemosa* use 24 % groundwater and 9 % dew (Wei et al. 2013; Lovelock et al. 2017). Since freshwater is more depleted in ^{2}H than seawater, field trees under high salt stress may have been more dependent on opportunistic freshwater uptake than trees under low salt stress, resulting in the production of lipids that are more ^{2}H-depleted relative to the surface water from which net $\alpha^{2}H_{lipid\text{-}water}$ values are calculated (Ladd and Sachs 2017). Unlike in the field, where rain, dew, and low-salinity water sources may be at least sporadically available to mangroves, in the greenhouse, $\delta^{2}H_{water}$ was held relatively constant across the 25 ppt salinity range. Supplementary Figure 4.1 shows that while growth water became slightly more ^{2}H-enriched over ~1.5 years, differences in $\delta^{2}H_{water}$ across salinities were about 8‰, which is small relative to the observed differences between $\delta^{2}H$ of freshwater and saline water in the field (about 30‰) (Ladd and Sachs 2015a). Therefore, the lack of strong positive correlation between $\alpha^{2}H_{lipid\text{-}water}$ and salinity in greenhouse-cultivated trees may be due to the fact that, unlike trees in the field, they had no access to water with different $\delta^{2}H$ values than that provided in the growth tubs. In addition, while the field studies (Ladd and Sachs 2012, 2015a, 2017) found that the correlation coefficient between salinity and $\alpha^{2}H_{lipid\text{-}water}$ was higher than that between salinity and $\delta^{2}H_{lipid}$, our results show that the strength of the two correlations are about the same, or even lower in the case of *X. granatum*. The strong correlations of $\delta^{2}H_{water}$ values with salinity in the field (through the mixing of freshwater with a low $\delta^{2}H$ value and seawater with a high $\delta^{2}H$ value) are additive to the tendency of mangroves to fractionate ^{2}H from ^{1}H to a greater extent at high salinity, and stable $\delta^{2}H_{water}$

values across salinity treatments in the greenhouse may therefore have resulted in weaker observed relationships between $\alpha^2H_{lipid\text{-}water}$ and salinity.

Other differences between natural environments and greenhouse settings such as temperature may have contributed to different trends between uncultivated and greenhouse-cultivated mangrove-derived lipids and salinity. It is unclear what effect temperature would have on hydrogen isotope fractionation in mangroves, as this has not been studied directly. However, in growth chamber experiments with other vascular plants, temperature did not affect hydrogen isotope fractionation during lipid biosynthesis (Zhou et al. 2011). Additionally, since all mangroves in our study were exposed to the same temperature conditions regardless of salinity treatment, any possible effect of temperature on α^2H would have affected plants in all salinity treatments equally. However, it may be possible that cold temperature imposed significant cold stress on all greenhouse plants so that the temperature effect outweighed changes in isotopic fractionation due to differences in salinity, resulting in a different relationship between salinity and δ^2H_{lipid} from that of uncultivated trees.

It is also possible that parameters not controlled in the greenhouse experiments, such as nutrient availability or water temperature, co-varied with salinity in the field sites and were responsible for the observed relationships between salinity and $\alpha^2H_{lipid\text{-}water}$. However, considering that the same relationship between salinity and $\alpha^2H_{lipid\text{-}water}$ has been observed across diverse settings in the tropics and subtropics (Ladd and Sachs 2012, 2015a; b, 2017; He et al. 2017), this seems unlikely.

It is noteworthy that all δ^2H_{lipid} values we report here from greenhouse-cultivated mangroves are from *n*-C_{16} and *n*-C_{18} fatty acids, while the field studies focused on *n*-alkanes and triterpenoids. This study focused on fatty acids as they have shorter residence time in leaves than

other lipid compounds and would reflect conditions at time of sampling more closely (Sachse et al. 2009; Kahmen et al. 2011a; Gao et al. 2012). However, the significant correlation between salinity and *R. mangle* $\delta^2H_{fatty\ acid}$ (Figure 4.3) and lack of any correlation between salinity and *R. mangle* $\delta^2H_{taraxerol}$, δ^2H_{lupeol} or $\delta^2H_{n\text{-C31 alkane}}$ suggests that δ^2H values of fatty acids have different responses to salinity than do *n*-alkanes or triterpenoids (Supplementary Figure 4.4). Therefore, fractionation during biosynthesis of isoprenoids and longer-chain acetogenic lipids may be responsible for a significant portion of the negative correlations between salinity and $\alpha^2H_{lipid\text{-}water}$ for these compounds in uncultivated mangroves.

4.5.2.2 Influence of δ^2H_{lw} on $\delta^2H_{fatty\ acid}$

The relationship between salinity and δ^2H values of leaf water (δ^2H_{lw}) can partially account for enrichment of greenhouse-cultivated mangrove $\delta^2H_{fatty\ acid}$ values with increasing salinity. Plant leaf water is a major source of hydrogen in lipids produced by dicots, and δ^2H_{lw} values depend on variables including temperature, relative humidity, stomatal conductance, transpiration rate, δ^2H_{water} and δ^2H_{xw} (Schmidt et al. 2003; Kahmen et al. 2011a, 2013). Therefore, if any of these variables are correlated with salinity, δ^2H_{lw} would also be expected to vary with salinity, and lipids produced from leaf water will have different δ^2H values.

The effects on δ^2H_{lw} of environmental parameters that vary with salinity (e.g., stomatal conductance, δ^2H_{xw} and path length) were assessed with a Péclet-modified Craig-Gordon leaf water isotope model (Kahmen et al. 2011b). δ^2H_{lw} values became enriched by 3‰ as stomatal conductance decreased across the range expected for salinity ranging between 5 and 30 ppt. However, δ^2H_{lw} values at 30 ppt were ^2H-depleted by 2.7‰ due to δ^2H_{xw} decreasing by 7.6‰ across the 25 ppt salinity range. In addition, at 30 ppt salinity, leaf water was ^2H-depleted by 3‰ relative to 5 ppt salinity, as path length increased from 120 mm to 280 mm. Therefore, δ^2H_{lw}

values were expected to be depleted by 2.7‰ at higher salinity, which is opposite to the observed $\delta^2H_{fatty\ acid}$ variability across salinities.

The combined effects of diurnally-varying environmental parameters (e.g., air temperature, relative humidity and $\delta^2H_{atmospheric\ vapor}$) were assessed with the same leaf water model. Because plants under high salt-stress display diurnal variations in WUE and photosynthetic activity (Naidoo and von Willert 1995; Barr et al. 2009), and photosynthetic activity is related to fatty acid production (Delwiche and Sharkey 1993; Bao et al. 2000), preferential sourcing of lipid-hydrogen from either an ^2H-depleted daytime, or ^2H-enriched nighttime leaf water pool could impact $\delta^2H_{fatty\ acid}$ values. Different species of mangroves (*A. germinans, A. annulata* and *R. mangle*) growing under high salinity minimize evaporative water loss during mid-day, when both air temperature and vapor pressure deficit are highest, by maintaining high photosynthetic rates and low WUE in early morning (Naidoo and von Willert 1995; Barr et al. 2009). Newly fixed carbon in plants is utilized for fatty acid or isoprene synthesis within 2 to 3 minutes (Delwiche and Sharkey 1993; Bao et al. 2000). If fixed carbon is used for fatty acid production very quickly after it is assimilated, fatty acid production is also likely to be more active when the plant is photosynthetically more active. Therefore, if the mangroves cultivated at high salinity in our study exhibited highest photosynthetic performance in the morning to avoid water loss, the lipids produced may have incorporated the δ^2H composition of the nighttime leaf-water pool, which the leaf water model predicts would be enriched by 16‰ relative to the daytime leaf-water pool. Mangroves growing at low salinity, on the other hand, would be relatively less sensitive to water loss, and their lipids, by extension, less impacted by the ^2H-enriched nighttime leaf-water pool, which would result in more ^2H-depleted lipids. Integrated with the result above, while plants growing at high salinity draw from a leaf-water pool depleted by 3‰ relative to plants growing

at low salinity, if their lipid synthesis relies more on the enriched nighttime leaf-water pool, this mechanism alone can account for about half of the entire 22 to 24‰ variability in $\delta^2H_{fatty\ acid}$ of *R. mangle* and *X. granatum*, or about a quarter of the 48 to 64‰ variability in $\delta^2H_{fatty\ acid}$ of *R. apiculata.*

Differences in $\delta^2H_{fatty\ acid}$ values or trends with salinity among species may be due to species-specific physiological processes for salt management that result in different leaf water potential and leaf water enrichment. For example, effective salt secretion may influence the proportion of more or less enriched leaf water pool during day and night that gets incorporated into lipids. In our study, *A. germinans* and *L. racemosa* were the only species (of the five) that are known to secrete salt from their leaves, and $\delta^2H_{fatty\ acid}$ values of both species were uncorrelated with salinity. High efficiency of salt secretion may be maintained by daily variations in transpiration rates to keep xylem water potential very low during the day (Waisel et al. 1986). Therefore, effective salt secretion may have helped *A. germinans* and *L. racemosa* in high salinity treatments to be less sensitive to water loss during midday and less reliant on the enriched nighttime leaf water pool relative to other species. Different biophysical processes of species relying on the same salt management strategies may also affect water potentials. For example, while *A. germinans* and *Rhizophora* spp. are both capable of accumulating salt in leaf vacuoles and producing organic solutes, different types and concentrations of compatible solutes produced by each species may also affect osmotic potentials to different degrees (Popp et al. 1985). In addition, distinct compatible solutes produced by different species may have a larger impact on δ^2H_{lipid} values than on δ^2H_{water} values, as types and varying proportions of compatible solutes in different salt marsh plants or mangrove species may result in varying contributions of hydrogen

in alkanes and fatty acids from photosynthetic and metabolic NADPH pools (Ladd and Sachs 2015b; Eley et al. 2018).

4.5.2.3 Potential reliance on stored carbohydrates

The different relationship between lipid δ^2H values and salinity from greenhouse-cultivated and uncultivated mangroves may also be explained by greenhouse seedlings relying on stored carbohydrates in large propagules during fatty acid synthesis. Hydrogen in lipids is derived from leaf water and NADPH from either photosynthesis or sugar metabolism (Schmidt et al. 2003). When plants synthesize lipids from stored carbohydrates, hydrogen can come from NADPH either in the chloroplast (produced by photosynthesis) or in the cytosol (produced by sugar metabolism), and photosynthetic NADPH is expected to be depleted in ^2H relative to metabolic NADPH by as much as several hundred per mill (Schmidt et al. 2003). If photosynthetic activity is limited during lipid synthesis, plants are more likely to rely on NADPH from the cytosol, producing more ^2H-enriched lipids (Schmidt et al. 2003; Cormier et al. 2018). Several studies have observed ^2H-enriched *n*-alkanes in leaf waxes of angiosperms that were photosynthetically limited and relied on stored carbohydrates in large seeds (Newberry et al. 2015; Freimuth et al. 2017; Cormier et al. 2018).

Weights of mangrove seeds vary widely between species, but the two genera that showed significant correlation between salinity and δ^2H_{lipid} in our study have very large seeds. *X. granatum* seeds typically weigh 45–77 g, while *Rhizophora* species propagules weigh 14–30 g (Rabinowitz 1978; Smith 1987; Gokhale and Chavan 2002; Das and Ghose 2003), and 40–60% of the propagule mass is in the form of starch and sugar, potentially providing a long-lasting carbohydrate source (Smith 1987; Gunawan et al. 2013). If mangrove seedlings growing at high salinity had limited photosynthetic capability and relied more on stored carbohydrates in

propagules for lipid production, contributions of H derived from the ^{2}H-enriched metabolic NADPH pool would be larger than that from the ^{2}H-depleted photosynthetic NADPH pool, so lipids would be more enriched in ^{2}H (Newberry et al. 2015; Cormier et al. 2018). This trend is expected to be more pronounced in alkanes or isoprenoids than in fatty acids, which have relatively short turnover times (Sachse et al. 2009; Kahmen et al. 2011a; Gao et al. 2012). In our study, δ^{2}H values of triterpenoids extracted from *R. mangle* leaves harvested in 2016 were more depleted than those extracted from leaves harvested in 2014 (Figure 4.5), supporting the possibility that lipid-hydrogen was derived in part from carbohydrates stored in propagules and large seeds. As the plants matured they presumably relied less on those maternal reserves and more on their photosynthetic capacity.

In summary, the relationships between $\delta^{2}H_{lipid}$ values and salinity were different for fatty acids produced by three cultivated mangrove species (*R. apiculata, R. mangle* and *X. granatum*) than for *n*-alkanes and triterpenols from 7 mangrove species in diverse natural settings (Ladd and Sachs 2012, 2015a; b, 2017; He et al. 2017). In order to be able to improve uncertainties in the relationship between α^{2}H and salinity using greenhouse-cultivated mangroves, a better understanding of the impact of salinity on α^{2}H is necessary. For instance, if the difference is largely due to a lack of ^{2}H-depleted freshwater sources in the greenhouse, improved calibrations might only be possible if alternate freshwater sources can be provided in the greenhouse.

4.5.3 *Implications of $\delta^{2}H$ and $\delta^{13}C_{fatty\ acid}$ measurements from greenhouse-cultivated mangroves for reconstructing precipitation rates*

The use of coupled δ^{2}H and δ^{13}C values of mangrove lipids holds promise for quantitatively reconstructing precipitation rates in the past, a climate parameter for which there are few proxies

at present. In order to do so, salinity and δ^2H_{water} values are calculated from the definition of α ($\alpha^2H = (\delta^2H_{lipid} + 1000) / (\delta^2H_{water} + 1000)$ and $\alpha^{13}C = (\delta^{13}C_{lipid} + 1000) / (\delta^{13}C_{atm} + 1000)$) and the linear relationships between α and salinity ($\alpha^2H = m_2 \times S + b_2$ and $\alpha^{13}C = m_{13} \times S + b_{13}$), as implied in equations (1) and (2). Representative slopes and intercepts were $m_2 = -0.0015 \pm 0.000026$, $b_2 = 0.892 \pm 0.0057$, $m_{13} = 0.00019 \pm 0.000053$ and $b_{13} = 0.970 \pm 0.0012$ (calibrations from *A. marina n*-C_{31} alkanes, Ladd and Sachs (2012, 2013)). We assessed uncertainties in the derived salinity and δ^2H_{water} values using a 1000-iteration Monte Carlo simulation that included both calibration and analytical uncertainties for both δ^2H and $\delta^{13}C$.

$$\text{Salinity} = \left(\frac{\left(\delta^{13}C_{lipid} + 1000\right)}{\left(\delta^{13}C_{atm} + 1000\right)} - b_{13} \right) \times \frac{1}{m_{13}} \qquad (1)$$

$$\delta^2H_{water} = \left(\frac{\left(\delta^2H_{lipid} + 1000\right)}{\frac{m_2}{m_{13}}\left(\frac{\left(\delta^{13}C_{lipid} + 1000\right)}{\left(\delta^{13}C_{atm} + 1000\right)} - b_{13}\right) + b_2} \right) - 1000 \qquad (2)$$

To evaluate the effect that reducing uncertainties in the calibrations of both α^2H and $\alpha^{13}C$ versus salinity would have on the uncertainty of the derived salinity and δ^2H_{water} values, several 1000-iteration Monte Carlo analyses with a surrogate data point were performed ($\delta^2H_{lipid} = -100 \pm 5‰$, $\delta^{13}C_{lipid} = -30 \pm 0.3‰$), assuming a 50% and 100% reduction in the calibration uncertainties and propagating the reduced errors to calculate uncertainties in salinity and δ^2H_{water}. Results of these analyses (Table 4.7) indicate that reducing uncertainty in the $\alpha^{13}C$ – salinity calibration alone can reduce as much uncertainty in the derived salinity and δ^2H_{water} values as reducing uncertainties in both the α^2H-salinity and $\alpha^{13}C$-salinity calibrations. Future work should therefore focus on obtaining improved $\alpha^{13}C$-salinity calibrations from both field and lab-based studies, possibly by increasing the number of samples to be analyzed.

Future work should also focus on measuring H and C isotopes of source-specific biomarkers. We have used slopes and intercepts from *n*-C_{31} alkanes for the uncertainty analysis above to demonstrate how the paired H and C isotope approach would work, and focused on *n*-C_{16} and *n*-C_{18} fatty acid δ^2H and $\delta^{13}C$ measurements to gain more insight into the mechanisms that control H and C isotope fractionation as a function of salinity in mangrove lipids. However, *n*-C_{16}, *n*-C_{18} fatty acids and *n*-alkanes are produced not only by mangroves, but also by terrestrial vascular plants, phytoplankton, and bacteria (Bianchi and Canuel 2011). Therefore, it would be virtually impossible to discern whether fatty acids or *n*-alkanes in mangrove swamps and coastal sediments originated from mangroves or other organisms. Because hydrogen and carbon isotope fractionation in lipids produced by organisms other than mangroves may respond differently to salinity, application of paired δ^2H and $\delta^{13}C$ of fatty acids or alkanes with unknown sources cannot provide reasonable estimates of salinity and δ^2H_{water}. A promising alternative to fatty acids and *n*-alkanes is taraxerol, which is primarily produced by *Rhizophora spp.* mangroves (Versteegh et al. 2004; Koch et al. 2005), which are dominant in many tropical mangrove forests (Duke 2006). Since taraxerol found in coastal tropical and subtropical sediments is likely to be derived from mangroves, applying the paired δ^2H and $\delta^{13}C$ approach with taraxerol is a promising approach for constructing past precipitation rates.

In addition, for future mangrove culturing studies that may be conducted to improve the calibrations between salinity and δ^2H or $\delta^{13}C$ of mangrove-derived lipids, the culturing could simulate field conditions more closely. For instance, temperature and relative humidity inside the greenhouse could be set higher to better mimic tropical climate conditions and protect trees from possible cold stress. Also, transferring plants to larger pots more often would allow more space for roots and prevent plant growth from possible root restriction by container sizes.

4.6 CONCLUSIONS

$\delta^{13}C$ and $\delta^{2}H$ values of *n*-C_{16} and *n*-C_{18} fatty acids and $\delta^{13}C$ values of bulk leaves in five species of mangroves cultivated in salinity treatments of 5 to 30 ppt in the UW greenhouse were measured. Both $\delta^{13}C_{fatty\ acids}$ and $\delta^{13}C_{bulk\ leaf}$ values from three species (*L. racemosa, R. apiculata,* and *X. granatum*) were positively correlated with salinity (0.12–0.21‰ / ppt and 0.10–0.22‰ /ppt, respectively), due to increased WUE and ^{13}C-enriched internal CO_2 pool with increasing salinity.

$\delta^{2}H_{fatty\ acids}$ values from three species (*R. apiculata, R. mangle,* and *X. granatum*) were positively correlated with salinity (0.47–1.25‰ / ppt), opposite to all field studies up to date, most likely due to lack of ^{2}H-depleted freshwater in the greenhouse. The positive relationship observed between salinity and $\delta^{2}H_{fatty\ acids}$ in greenhouse-cultivated mangroves may be caused by temporal variation in $\delta^{2}H_{leaf\ water}$ values and timing of lipid production, or reliance on stored carbohydrates in seeds.

To use paired $\delta^{2}H$ and $\delta^{13}C$ measurements of mangrove lipids to quantitatively reconstruct salinity and water isotopes, $\delta^{2}H$ and $\delta^{13}C$ values of mangrove-specific biomarkers such as taraxerol should be measured. In addition, improving field and lab-based calibrations between salinity and $\alpha^{13}C$, partly by cultivating mangroves under an environment that resembles tropical or subtropical climate more closely, will be important for future studies. At this point, improving field and lab-based calibrations between salinity and $\alpha^{13}C$ will be most likely to reduce uncertainties in estimated salinity and water isotopes.

4.7 ACKNOWLEDGMENTS

This work was supported by the National Science Foundation under Grants No. EAR-1348396 and OCE-1736222 (J.P.S.). Erick Waguk assisted with seed collection in Micronesia. Doug Ewing, June Landenburger, Marta Wolfshorndl, Colton Skavicus, Cyrena Thibodeau and Josh Gregersen assisted with mangrove cultivation in the greenhouse. Matthew Wolhowe, Mark Haught, Ashley Maloney and Tess Clinkingbeard provided assistance and advice with isotope measurements and other analytical techniques. Paul Quay, Jodi Young, Steve Emerson and Liz van Volkenberg provided constructive feedback and comments that greatly improved both this study and this manuscript. Two anonymous reviewers provided helpful feedback and comments that improved this manuscript. We are grateful for all their contributions.

4.8 FIGURES AND TABLES

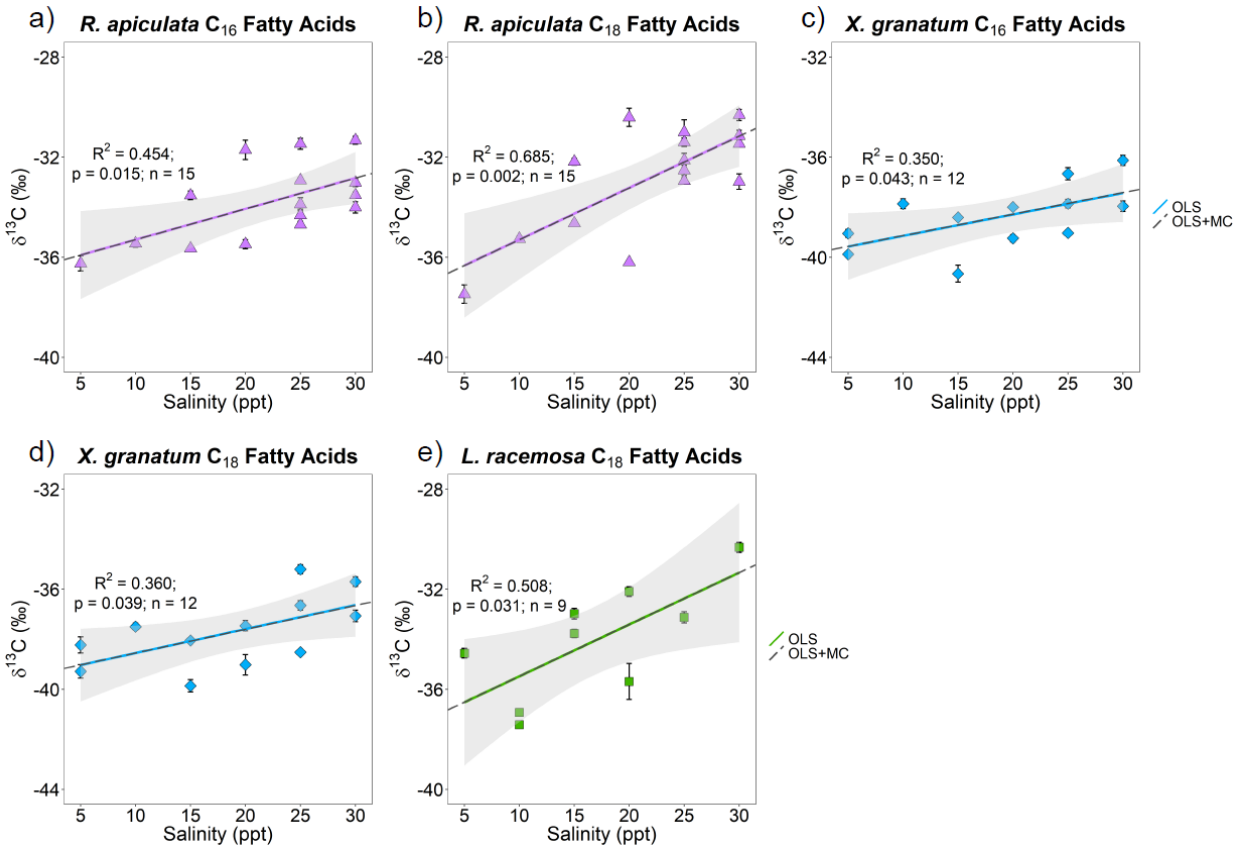

Figure 4.1 Relationships between salinity and $\delta^{13}C_{fatty\ acid}$ in mangrove leaf lipids. Panels only show species and compounds that display significant relationship ($p < 0.05$). All panels include the regression lines (colored solid lines, labeled "OLS"), regression lines from Monte Carlo analysis (gray dashed lines, labeled "OLS+MC") and 95% confidence intervals (gray shaded areas). Error bars that are not displayed are smaller than the plot marker size.

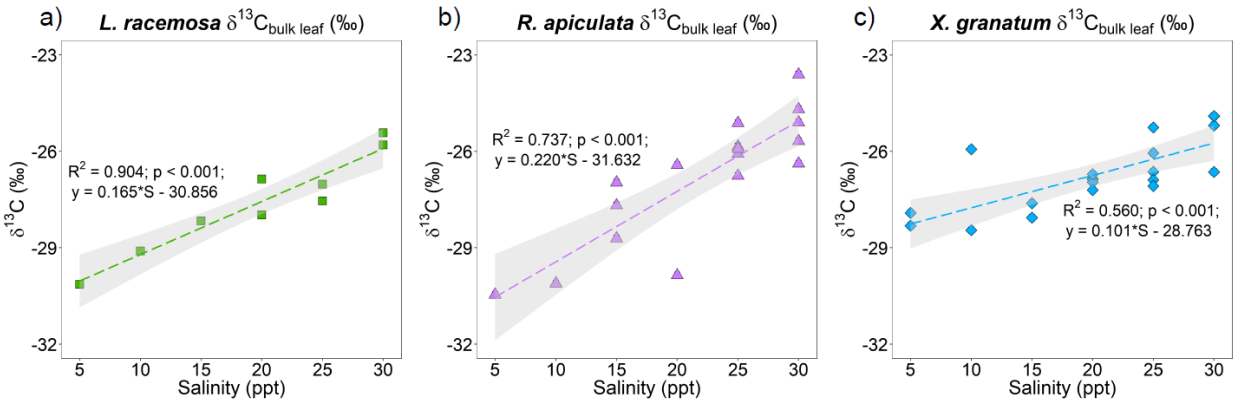

Figure 4.2 Relationships between salinity and $\delta^{13}C_{bulk\ leaf}$ in mangrove leaf lipids. Panels only show species that display significant relationship ($p < 0.05$). All panels show the regression lines (colored dashed lines) and 95% confidence intervals (gray shaded areas). Error bars that are not displayed are smaller than the plot marker size.

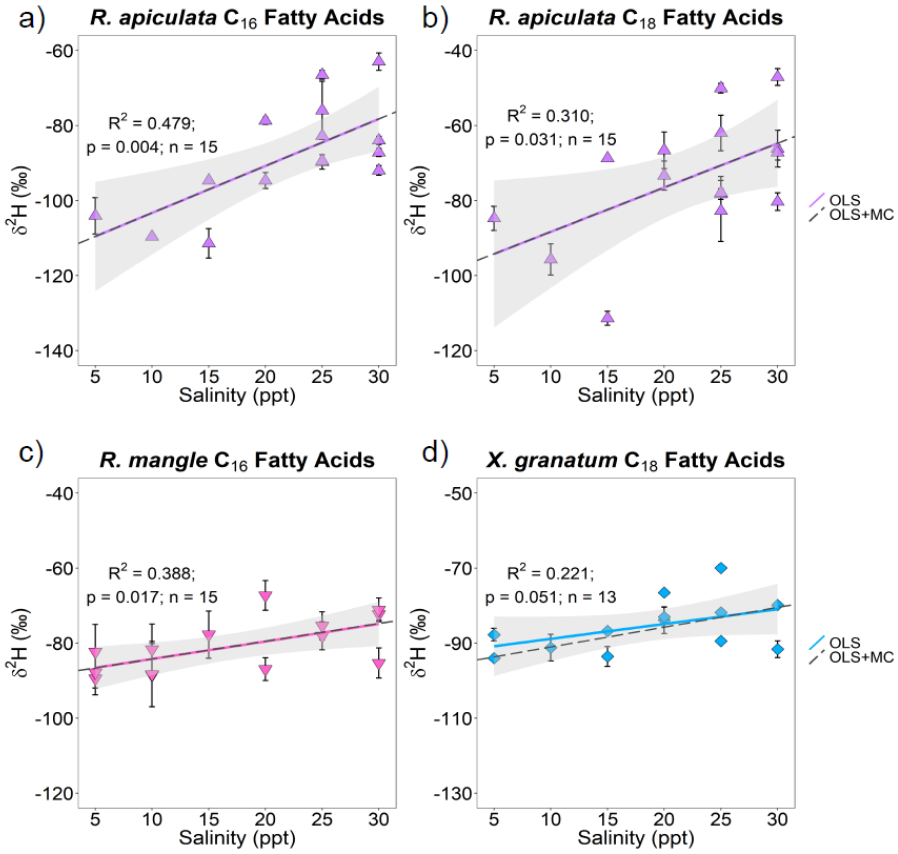

Figure 4.3 Relationships between salinity and $\delta^2H_{fatty\ acid}$ in mangrove leaf lipids. Panels only show species and compounds that display significant relationship ($p < 0.05$). All panels include the regression lines (colored solid lines), regression lines from Monte Carlo analysis (gray dashed lines) and 95% confidence intervals (gray shaded areas). Error bars that are not displayed are smaller than the plot marker size.

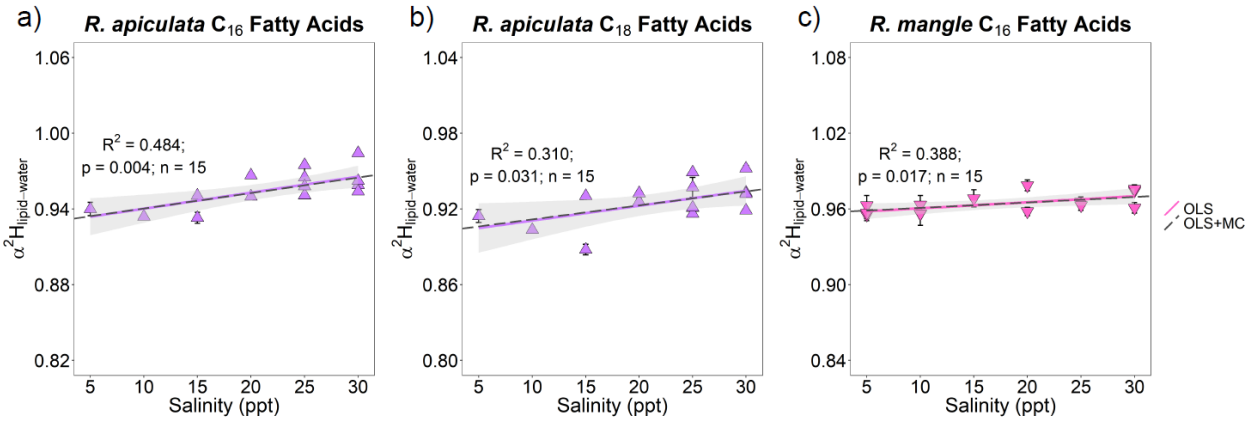

Figure 4.4 Relationships between salinity and $\alpha^2H_{lipid\text{-}water}$ in mangrove leaf lipids. Panels only show species and compounds that display significant relationship ($p < 0.05$). All panels include the regression line (colored solid lines), regression line from Monte Carlo analysis (gray dashed lines) and 95% confidence intervals (gray shaded areas). Error bars in each panel represent propagated uncertainties from δ^2H_{lipid} and δ^2H_{water} measurements, and those that are not displayed are smaller than the plot marker size.

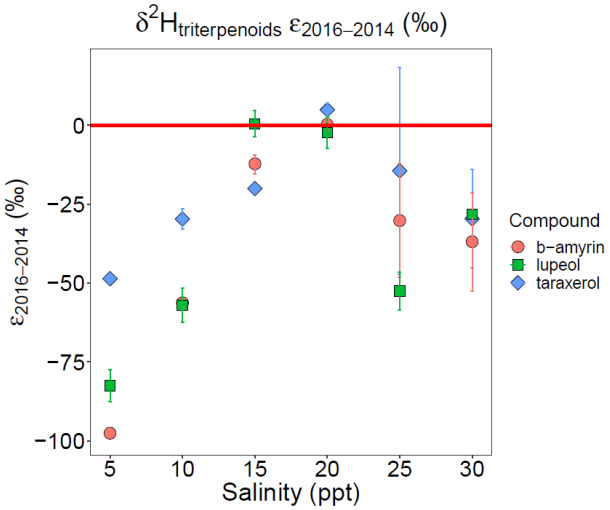

Figure 4.5 Relationships between salinity and $\delta^2H_{triterpenoids}$ in *R. mangle* leaf lipids. Y axis values show the fractionation between lipids harvested in 2016 and 2014 ($\varepsilon_{2016\text{-}2014}$). Red solid line ($\delta^2H$ = 0‰) is drawn for reference. Error bars that are not displayed are smaller than the plot marker size.

Table 4.1 Types of mangroves cultivated in the UW greenhouse and their salt management strategies (Parida and Jha, 2010; Reef and Lovelock, 2015)

Mangrove Species	Exclude	Secrete	Accumulate	Salt tolerance level
Avicennia germinans	X	X	X	High
Heritiera littoralis	X			Mid
Laguncularia racemosa	X	X		Mid
Rhizophora apiculata	X		X	Mid
Rhizophora mangle	X		X	High
Xylocarpus granatum			X	Low

Table 4.2 Leaf water model sensitivity tested by holding other variables constant while changing a single variable

	Input	δ^2H_{lw} (‰)	Range of δ^2H_{lw}
Temperature (°C)	16 ± 3 to 23 ± 3	−31 ± 3 to −38 ± 3	7 ‰
Relative humidity (%)	25 ± 5 to 90 ± 5	−28 ± 11 to −39 ± 4	11 ‰
$\delta^2H_{atmospheric\ vapor}$ (‰)	−110 ± 5 to −125 ± 5	−32 ± 3 to −44 ± 3	12 ‰
Stomatal conductance (g_s; mol/m^{2}s)	0.1 ± 0.05 to 0.4 ± 0.05	−41 ± 3 to −38 ± 3	3 ‰
Effective path length (L; mm)	150 ± 50 to 300 ± 50	−48 ± 3 to −44 ± 3	4 ‰
$\delta^2H_{xylem\ water}$ (‰)	−42 ± 5 to −48 ± 5	−35 ± 3 to −37 ± 3	2 ‰

Table 4.3 Inputs used for leaf water model to calculate $\delta^2H_{leaf\ water}$ at 5 and 30 ppt salinity levels

Salinity (ppt)	g_s (mol/m^2/s)	L (mm)	$\delta^2H_{xylem\ water}$ (‰)	$\delta^2H_{leaf\ water}$ (‰)
5	0.35	120	-42	−36.1 ± 2.6
30	0.15	280	-48	−38.9 ± 3.0

Table 4.4 Inputs used for leaf water model to calculate $\delta^2H_{leaf\ water}$ in daytime and nighttime

	Temperature	Water vapor content	Relative Humidity	$\delta^2H_{atmospheric\ vapor}$
Day	21 ± 2 °C	15000 ppm	0.97 ± 0.10	−125 ± 5 ‰
Night	17 ± 2 °C	12000 ppm	1.00 ± 0.10	−110 ± 5 ‰

Table 4.5 Results of linear regression analysis between salinity and $\delta^2H_{fatty\ acid}$ or $\delta^{13}C_{fatty\ acid}$ in all mangrove species and two fatty acid compounds

Isotopes	Species	N	Compound	Slope	Intercept	MC slope	MC intercept	R^2	p
$\delta^2H_{fatty\ acid}$	*A. germinans*	10	*n*-C_{16}	−0.378 ± 0.240	−94.524 ± 5.040	−0.380 ± 0.037	−94.485 ± 0.818	0.237	0.153
			n-C_{18}	−0.108 ± 0.346	−64.258 ± 7.278	−0.109 ± 0.118	−64.221 ± 3.421	0.012	0.764
	L. racemosa	9	*n*-C_{16}	0.031 ± 0.205	−160.411 ± 3.747	0.039 ± 0.055	−160.428 ± 0.783	0.005	0.858
			n-C_{18}	0.506 ± 0.396	−148.100 ± 7.231	0.502 ± 0.092	−148.029 ± 1.728	0.189	0.242
	R. apiculata	**15**	***n*-C_{16}**	**1.252 ± 0.362**	**−115.812 ± 8.411**	**1.253 ± 0.113**	**−115.816 ± 2.769**	**0.479**	**0.004**
			***n*-C_{18}**	**1.180 ± 0.488**	**−100.133 ± 11.336**	**1.179 ± 0.113**	**−100.069 ± 2.582**	**0.310**	**0.031**
	R. mangle	**15**	***n*-C_{16}**	**0.467 ± 0.169**	**−88.888 ± 3.310**	**0.474 ± 0.142**	**−88.970 ± 3.408**	**0.388**	**0.017**
	X. granatum	13	*n*-C_{16}	0.149 ± 0.230	−93.505 ± 4.587	0.148 ± 0.038	−93.506 ± 0.842	0.012	0.529
			***n*-C_{18}**	**0.528 ± 0.244**	**−96.293 ± 4.874**	**0.529 ± 0.060**	**−96.307 ± 1.396**	**0.221**	**0.051**
$\delta^{13}C_{fatty\ acid}$	*A. germinans*	10	*n*-C_{16}	−0.007 ± 0.081	−33.969 ± 1.712	−0.007 ± 0.034	−33.983 ± 0.708	0.001	0.934
			n-C_{18}	0.021 ± 0.079	−32.918 ± 1.670	0.020 ± 0.029	−32.896 ± 0.612	0.009	0.797
	L. racemosa	**9**	*n*-C_{16}	0.179 ± 0.119	−39.167 ± 2.173	0.178 ± 0.021	−39.125 ± 0.929	0.244	0.176
			***n*-C_{18}**	**0.207 ± 0.077**	**−37.554 ± 1.408**	**0.207 ± 0.009**	**−37.544 ± 0.141**	**0.508**	**0.031**
	R. apiculata	**15**	***n*-C_{16}**	**0.123 ± 0.044**	**−36.525 ± 1.015**	**0.123 ± 0.008**	**−36.525 ± 0.185**	**0.454**	**0.015**
			***n*-C_{18}**	**0.207 ± 0.052**	**−37.363 ± 1.206**	**0.207 ± 0.009**	**−37.366 ± 0.210**	**0.685**	**0.002**
	R. mangle	15	*n*-C_{16}	−0.026 ± 0.024	−39.308 ± 0.460	−0.026 ± 0.008	−39.329 ± 0.176	0.092	0.292
	X. granatum	**12**	***n*-C_{16}**	**0.086 ± 0.037**	**−39.999 ± 0.759**	**0.086 ± 0.006**	**−39.998 ± 0.116**	**0.350**	**0.043**

			***n*-C$_{18}$**	**0.096 ± 0.040**	**−39.507 ± 0.831**	**0.095 ± 0.009**	**−39.496 ± 0.185**	**0.360**	**0.039**
$\alpha^2H_{lipid\text{-}sw}$	*A. germinans*	10	*n*-C$_{16}$	−0.00044 ± 0.00028	0.95037 ± 0.00590	−0.00049 ± 0.00108	0.95133 ± 0.02713	0.236	0.154
			n-C$_{18}$	−0.00011 ± 0.00035	0.93485 ± 0.00727	−0.00010 ± 0.00103	0.93493 ± 0.02635	0.012	0.764
	L. racemosa	9	*n*-C$_{16}$	0.00000 ± 0.00025	0.88130 ± 0.00460	0.00001 ± 0.00105	0.88097 ± 0.02395	0.000	0.992
			n-C$_{18}$	0.00051 ± 0.00040	0.85115 ± 0.00722	0.00051 ± 0.00107	0.85079 ± 0.02406	0.189	0.242
	R. apiculata	**15**	***n*-C$_{16}$**	**0.00127 ± 0.00036**	**0.92755 ± 0.00845**	**0.00123 ± 0.00139**	**0.92808 ± 0.03468**	**0.484**	**0.004**
			***n*-C$_{18}$**	**0.00118 ± 0.00049**	**0.89903 ± 0.01132**	**0.00111 ± 0.00138**	**0.90059 ± 0.03369**	**0.310**	**0.031**
	R. mangle	**15**	***n*-C$_{16}$**	**0.00047 ± 0.00018**	**0.95583 ± 0.00359**	**0.00043 ± 0.00177**	**0.95655 ± 0.04262**	**0.356**	**0.024**
	X. granatum	13	*n*-C$_{16}$	0.00003 ± 0.00022	0.95330 ± 0.00455	0.00002 ± 0.00098	0.95451 ± 0.02385	0.001	0.910
			n-C$_{18}$	0.00039 ± 0.00022	0.90634 ± 0.00458	0.00034 ± 0.00090	0.90774 ± 0.02227	0.221	0.105

Columns “MC slope” and “MC intercept” refer to results obtained from Monte Carlo approach. Relationships that are significant at the $p < 0.05$ level are indicated in bold letters.

Table 4.6 Results of linear regressions between salinity and $\delta^{13}C_{bulk\ leaf}$ in all five mangrove species

Isotopes	Species	N	Slope	Intercept	R^2	p
$\delta^{13}C_{bulk\ leaf}$	*A. germinans*	17	−0.030 ± 0.050	−28.445 ± 1.024	0.024	0.555
	L. racemosa	**9**	**0.164 ± 0.020**	**−30.858 ± 0.416**	**0.904**	**0.000**
	R. apiculata	**17**	**0.220 ± 0.034**	**−31.632 ± 0.767**	**0.737**	**0.000**
	R. mangle	18	−0.070 ± 0.030	−25.845 ± 0.567	0.257	0.032
	X. granatum	**20**	**0.101 ± 0.021**	**−28.763 ± 0.448**	**0.560**	**0.000**

Table 4.7 Uncertainties in salinity and δ^2H_{water} from Monte Carlo analysis with reduced uncertainties in current calibrations

	Salinity (ppt)	Salinity error (ppt)	δ^2H_{water} (‰)	δ^2H_{water} error (‰)
100% uncertainty in both C and H	43.07	3.08	87.93	6.09
50% uncertainty in both C and H	43.18	1.69	88.13	3.34
50% uncertainty in only H	43.16	3.26	88.11	6.47
50% uncertainty in only C	43.21	1.70	88.18	3.36
0% uncertainty in both C and H	43.26	0.52	88.26	1.02

.

4.9 SUPPLEMENTAL FIGURES AND TABLES

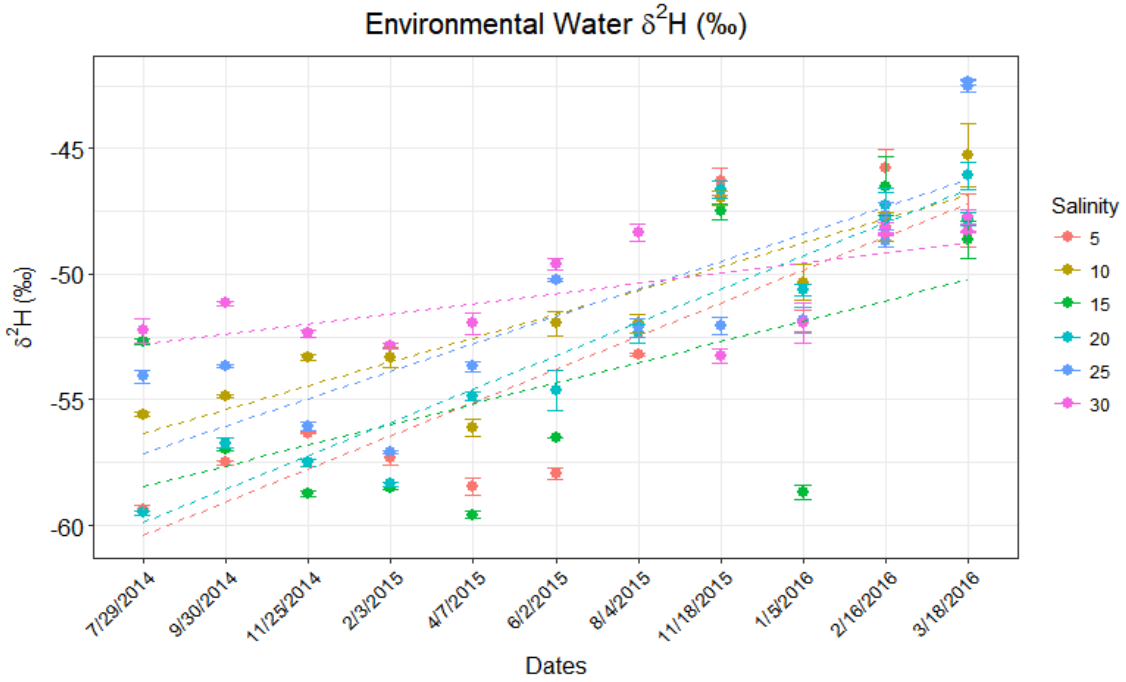

Supplementary Figure 4.1 δ^2H_{water} in the greenhouse tanks from July 2014 to March 2016

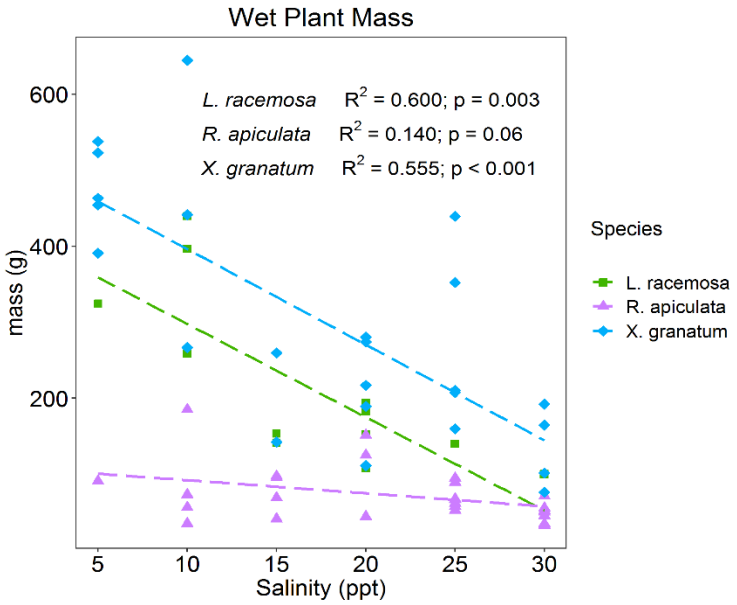

Supplementary Figure 4.2 Significant relationships ($p < 0.05$) between wet plant mass and salinity for mangrove species

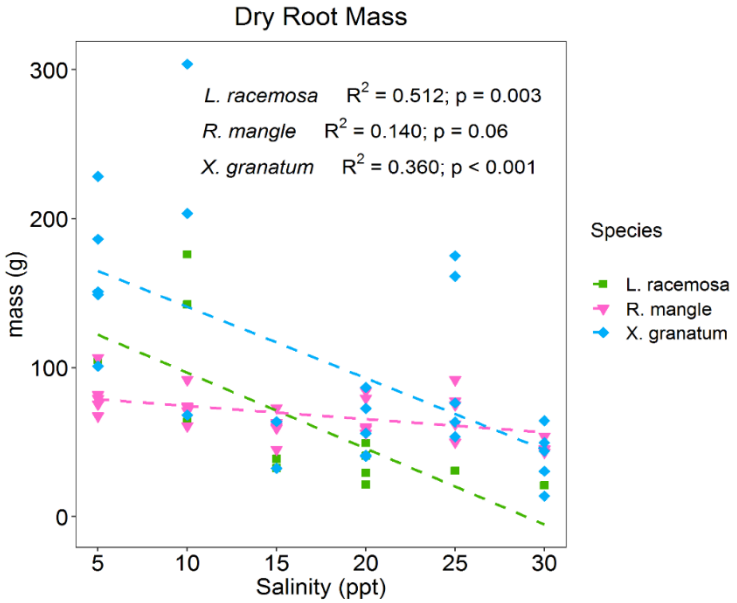

Supplementary Figure 4.3 Significant relationships ($p < 0.05$) between dry root mass and salinity for mangrove species

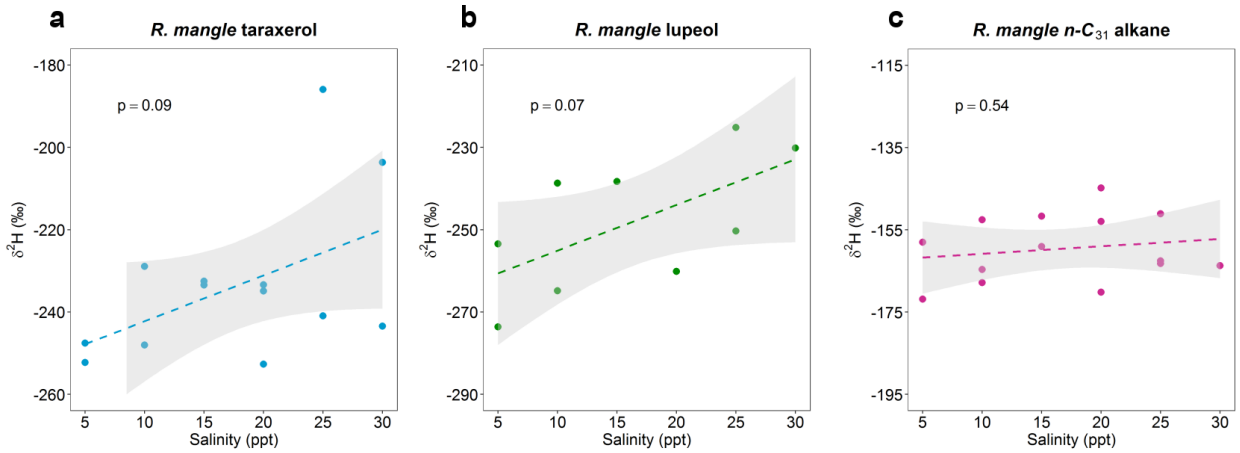

Supplementary Figure 4.4 $\delta^2H_{taraxerol}$, δ^2H_{lupeol} and $\delta^2H_{n\text{-}C31alkane}$ values from *R. mangle*, with regression lines (dashed) and 95% confidence intervals (gray shaded area).

Supplementary Table 4.1 δ^2H_{lw} calculated from stomatal conductance measurements in five mangrove species. Stomatal conductance of each species was measured with a porometer over 3 days in July 2014.

Species	*A. germinans*	*L. racemosa*	*R. apiculata*	*R. mangle*	*X. granatum*
Salinity	Stomatal conductance (mol/m^2/s)				
5 ppt	0.28 ± 0.07	0.14 ± 0.11	0.28 ± 0.22	0.12 ± 0.01	0.26 ± 0.20
30 ppt	0.21 ± 0.10	0.09 ± 0.07	0.16 ± 0.13	0.17 ± 0.08	0.11 ± 0.14
Salinity	Leaf water δ^2H (‰)				
5 ppt	-40.1 ± 3.1	-38.6 ± 3.1	-40.1 ± 3.2	-38.3 ± 3.0	-39.9 ± 3.2
30 ppt	-39.4 ± 3.1	-37.8 ± 3.1	-38.9 ± 3.1	-39.0 ± 3.1	-38.1 ± 3.2

Supplementary Table 4.2 Range of $\delta^2H_{fatty\ acid}$ and $\delta^{13}C_{fatty\ acid}$ values in five mangrove species

Species		*A. germinans*	*L. racemosa*	*R. apiculata*	*R. mangle*	*X. granatum*
Isotopes	Compound					
$\delta^2H_{fatty\ acid}$	*n*-C_{16}	-101 ± 6	-160 ± 4	-88 ± 14	-81 ± 7	-90 ± 7
	n-C_{18}	-66 ± 8	-140 ± 9	-94 ± 14	-	-85 ± 7
$\delta^{13}C_{fatty\ acid}$	*n*-C_{16}	-34.1 ± 1.9	-36.2 ± 2.9	-33.8 ± 1.5	-39.8 ± 0.8	-38.4 ± 1.3
	n-C_{18}	-32.5 ± 1.9	-34.1 ± 2.3	-32.8 ± 2.2	-	-37.7 ± 1.4

Supplementary Table 4.3 $\delta^2H_{triterpenoids}$ values measured from *R. mangle* leaves harvested in 2014 and 2016.

Compound	Salinity	δ^2H_{2014} (‰, VSMOW)	δ^2H_{2016} (‰, VSMOW)	$\varepsilon_{2016-2014 triterpenoids}$
β-amyrin	5	-188 ± 3	-267 ± 9	-98 ± 1
	10	-214 ± 3	-258 ± 9	-56 ± 1
	15	-231 ± 2	-240 ± 13	-12 ± 3
	20	-253 ± 2	-253 ± 10	0 ± 2
	25	217 ± 2	-241 ± 33	-30 ± 18
	30	-210 ± 8	-239 ± 29	-37 ± 16
Lupeol	5	-189 ± 8	-256 ± 16	-83 ± 5
	10	-207 ± 4	-251 ± 18	-57 ± 5
	15	-229 ± 2	-229 ± 15	0 ± 4
	20	-245 ± 3	247 ± 17	-2 ± 5
	25	-196 ± 5	-238 ± 18	-53 ± 6
	30	-210 ± 6	-232 ± 3	-28 ± 1
Taraxerol	5	-212 ± 2	-249 ± 3	-49 ± 0
	10	-215 ± 3	-238 ± 14	-30 ± 3
	15	-217 ± 2	-233 ± 1	-20 ± 0
	20	-244 ± 2	-240 ± 11	5 ± 2
	25	202 ± 2	-213 ± 39	-14 ± 33
	30	-200 ± 3	-224 ± 28	-30 ± 16

BIBLIOGRAPHY

Abualhaija, M. M., H. Whitby, and C. M. G. van den Berg. 2015. Competition between copper and iron for humic ligands in estuarine waters. Marine Chemistry **172**: 46–56. doi:10.1016/j.marchem.2015.03.010

Adly, C. L., J.E. Tremblay, R. T. Powell, E. Armstrong, G. Peers, and N. M. Price. 2015. Response of heterotrophic bacteria in a mesoscale iron enrichment in the northeast subarctic Pacific Ocean: Bacterial response in an iron-enrichment. Limnol. Oceanogr. **60**: 136–148. doi:10.1002/lno.10013

Allen, L. H. 2012. Vitamin B-12. Advances in Nutrition **3**: 54–55. doi:10.3945/an.111.001370

Alongi, D. M., and S. K. Mukhopadhyay. 2015. Contribution of mangroves to coastal carbon cycling in low latitude seas. Agricultural and Forest Meteorology **213**: 266–272. doi:10.1016/j.agrformet.2014.10.005

Arístegui, J., J. M. Gasol, C. M. Duarte, and G. J. Herndld. 2009. Microbial oceanography of the dark ocean's pelagic realm. Limnology & Oceanography **54**: 1501–1529. doi:10.4319/lo.2009.54.5.1501

Armstrong, E., J. Granger, E. L. Mann, and N. M. Price. 2004. Outer-membrane siderophore receptors of heterotrophic oceanic bacteria. Limnol. Oceanogr. **49**: 579–587. doi:10.4319/lo.2004.49.2.0579

Arnold, T. E., A. F. Diefendorf, M. Brenner, K. H. Freeman, and A. A. Baczynski. 2018. Climate response of the Florida Peninsula to Heinrich events in the North Atlantic. Quaternary Science Reviews **194**: 1–11. doi:10.1016/j.quascirev.2018.06.012

Arp, W. J. 1991. Effects of source-sink relations on photosynthetic acclimation to elevated CO2. Plant Cell Environ **14**: 869–875. doi:10.1111/j.1365-3040.1991.tb01450.x

Årstøl, E., and M. F. Hohmann-Marriott. 2019. Cyanobacterial Siderophores—Physiology, Structure, Biosynthesis, and Applications. Marine Drugs **17**: 281. doi:10.3390/md17050281

Atwood, A. R., and J. P. Sachs. 2014. Separating ITCZ- and ENSO-related rainfall changes in the Galápagos over the last 3 kyr using D/H ratios of multiple lipid biomarkers. Earth and Planetary Science Letters **404**: 408–419. doi:10.1016/j.epsl.2014.07.038

Baakza, A., A. K. Vala, B. P. Dave, and H. C. Dube. 2004. A comparative study of siderophore production by fungi from marine and terrestrial habitats. Journal of Experimental Marine Biology and Ecology **311**: 1–9. doi:10.1016/j.jembe.2003.12.028

de Baar, H. J. W. 2005. Synthesis of iron fertilization experiments: From the Iron Age in the Age of Enlightenment. J. Geophys. Res. **110**: C09S16. doi:10.1029/2004JC002601

Bagg, A., and J. B. Neilands. 1987. Molecular mechanism of regulation of siderophore-mediated iron assimilation. MICROBIOL. REV. **51**: 10.

Baker, A. R., and P. L. Croot. 2010. Atmospheric and marine controls on aerosol iron solubility in seawater. Marine Chemistry **120**: 4–13. doi:10.1016/j.marchem.2008.09.003

Balado, M., C. R. Osorio, and M. L. Lemos. 2006. A gene cluster involved in the biosynthesis of vanchrobactin, a chromosome-encoded siderophore produced by *Vibrio anguillarum*. Microbiology **152**: 3517–3528. doi:10.1099/mic.0.29298-0

Ball, M. C., and G. D. Farquhar. 1984. Photosynthetic and Stomatal Responses of Two Mangrove Species, *Aegiceras corniculatum* and *Avicennia marina* , to Long Term Salinity and Humidity Conditions. Plant Physiol. **74**: 1–6. doi:10.1104/pp.74.1.1

Bao, X., M. Focke, M. Pollard, and J. Ohlrogge. 2000. Understanding in vivo carbon precursor supply for fatty acid synthesis in leaf tissue. Plant Journal **22**: 39–50. doi:10.1046/j.1365-313X.2000.00712.x

Barbeau, K., E. L. Rue, C. G. Trick, K. W. Bruland, and A. Butler. 2003. Photochemical reactivity of siderophores produced by marine heterotrophic bacteria and cyanobacteria based on characteristic Fe(III) binding groups. Limnol. Oceanogr. **48**: 1069–1078. doi:10.4319/lo.2003.48.3.1069

Barr, J. G., J. D. Fuentes, V. Engel, and J. C. Zieman. 2009. Physiological responses of red mangroves to the climate in the Florida Everglades. Journal of Geophysical Research: Biogeosciences **114**: 1–13. doi:10.1029/2008JG000843

van den Berg, M. G. 1989. Adsorptive cathodic stripping voltammetry of trace elements in sea water. Analyst **114**: 1527. doi:10.1039/an9891401527

Bertrand, E. M., A. E. Allen, C. L. Dupont, T. M. Norden-Krichmar, J. Bai, R. E. Valas, and M. A. Saito. 2012. Influence of cobalamin scarcity on diatom molecular physiology and identification of a cobalamin acquisition protein. Proc. Natl. Acad. Sci. U.S.A. **109**. doi:10.1073/pnas.1201731109

Bertrand, E. M., J. P. McCrow, A. Moustafa, and others. 2015. Phytoplankton–bacterial interactions mediate micronutrient colimitation at the coastal Antarctic sea ice edge. Proc. Natl. Acad. Sci. U.S.A. **112**: 9938–9943. doi:10.1073/pnas.1501615112

Bertrand, E. M., M. A. Saito, P. A. Lee, R. B. Dunbar, P. N. Sedwick, and G. R. DiTullio. 2011. Iron Limitation of a Springtime Bacterial and Phytoplankton Community in the Ross Sea: Implications for Vitamin B12 Nutrition. Front. Microbio. **2**. doi:10.3389/fmicb.2011.00160

Bertrand, E. M., M. A. Saito, J. M. Rose, C. R. Riesselman, M. C. Lohan, A. E. Noble, P. A. Lee, and G. R. DiTullio. 2007. Vitamin B $_{12}$ and iron colimitation of phytoplankton growth in the Ross Sea. Limnol. Oceanogr. **52**: 1079–1093. doi:10.4319/lo.2007.52.3.1079

Bi, Y., D. L. Hesterberg, and O. W. Duckworth. 2010. Siderophore-promoted dissolution of cobalt from hydroxide minerals. Geochimica et Cosmochimica Acta **74**: 2915–2925. doi:10.1016/j.gca.2010.02.028

Bianchi, T. S., and E. A. Canuel. 2011. Chemical biomarkers in aquatic ecosystems, Princeton University Press.

Biber, P. D. 2006. Measuring the effects of salinity stress in the red mangrove, *Rhizophora mangle L.* African Journal of Agricultural Research **1**: 1–4. doi:doi.org/10.5897/AJAR.9000485

Blanco-Ameijeiras, S., D. J. E. Cabanes, R. N. Cable, and others. 2020. Exopolymeric Substances Control Microbial Community Structure and Function by Contributing to both C and Fe Nutrition in Fe-Limited Southern Ocean Provinces. Microorganisms **8**: 1980. doi:10.3390/microorganisms8121980

Boiteau, R. M., D. R. Mende, N. J. Hawco, and others. 2016a. Siderophore-based microbial adaptations to iron scarcity across the eastern Pacific Ocean. Proc Natl Acad Sci USA **113**: 14237–14242. doi:10.1073/pnas.1608594113

Boiteau, R. M., and D. J. Repeta. 2022. Slow Kinetics of Iron Binding to Marine Ligands in Seawater Measured by Isotope Exchange Liquid Chromatography–Inductively Coupled Plasma Mass Spectrometry. Environ. Sci. Technol. **56**: 3770–3779. doi:10.1021/acs.est.1c06922

Boiteau, R. M., C. P. Till, T. H. Coale, J. N. Fitzsimmons, K. W. Bruland, and D. J. Repeta. 2019. Patterns of iron and siderophore distributions across the California Current System. Limnol. Oceanogr. **64**: 376–389. doi:10.1002/lno.11046

Boiteau, R. M., C. P. Till, A. Ruacho, and others. 2016b. Structural Characterization of Natural Nickel and Copper Binding Ligands along the US GEOTRACES Eastern Pacific Zonal Transect. Front. Mar. Sci. **3**: 1–16. doi:10.3389/fmars.2016.00243

Bolger, A. M., M. Lohse, and B. Usadel. 2014. Trimmomatic: a flexible trimmer for Illumina sequence data. Bioinformatics **30**: 2114–2120. doi:10.1093/bioinformatics/btu170

Bonnet, S., A. Tovar-Sánchez, C. Panzeca, C. M. Duarte, E. Ortega-Retuerta, and S. A. Sañudo-Wilhelmy. 2013. Geographical gradients of dissolved Vitamin B12 in the Mediterranean Sea. Front. Microbiol. **4**. doi:10.3389/fmicb.2013.00126

Bony, S., C. Risi, and F. Vimeux. 2008. Influence of convective processes on the isotopic composition ($\delta^{18}O$ and δD) of precipitation and water vapor in the tropics: 1. Radiative-convective equilibrium and Tropical Ocean-Global Atmosphere-Coupled Ocean-Atmosphere Response Experiment (. Journal of Geophysical Research Atmospheres **113**: 1–21. doi:10.1029/2008JD009942

Borths, E. L., B. Poolman, R. N. Hvorup, K. P. Locher, and D. C. Rees. 2005. In Vitro Functional Characterization of BtuCD-F, the *Escherichia coli* ABC Transporter for Vitamin B_{12} Uptake. Biochemistry **44**: 16301–16309. doi:10.1021/bi0513103

Boström, K. H., K. Simu, Å. Hagström, and L. Riemann. 2004. Optimization of DNA extraction for quantitative marine bacterioplankton community analysis: DNA extraction from bacterioplankton. Limnol. Oceanogr. Methods **2**: 365–373. doi:10.4319/lom.2004.2.365

Bown, J., M. Boye, and D. M. Nelson. 2012. New insights on the role of organic speciation in the biogeochemical cycle of dissolved cobalt in the southeastern Atlantic and the Southern Ocean. Biogeosciences **9**: 2719–2736. doi:10.5194/bg-9-2719-2012

Boyd, P. W., T. Jickells, C. S. Law, and others. 2007. Mesoscale Iron Enrichment Experiments 1993-2005: Synthesis and Future Directions. Science **315**: 612–617. doi:10.1126/science.1131669

Boyd, P. W., R. F. Strzepek, M. J. Ellwood, D. A. Hutchins, S. D. Nodder, B. S. Twining, and S. W. Wilhelm. 2015. Why are biotic iron pools uniform across high- and low-iron pelagic ecosystems? Global Biogeochem. Cycles **29**: 1028–1043. doi:10.1002/2014GB005014

Boysen, A. K., K. R. Heal, L. T. Carlson, and A. E. Ingalls. 2018. Best-Matched Internal Standard Normalization in Liquid Chromatography–Mass Spectrometry Metabolomics Applied to Environmental Samples. Anal. Chem. **90**: 1363–1369. doi:10.1021/acs.analchem.7b04400

Browning, T. J., E. P. Achterberg, I. Rapp, A. Engel, E. M. Bertrand, A. Tagliabue, and C. M. Moore. 2017. Nutrient co-limitation at the boundary of an oceanic gyre. Nature **551**: 242–246. doi:10.1038/nature24063

Brugnoli, E., M. Lauteri, and C. N. R. Istituto. 1991. Effects of Salinity on Stomatal Conductance, Photosynthetic Capacity, and Carbon Isotope Discrimination of Salt-Tolerant (Gossypium hirsutum L.) and Salt-Sensitive (Phaseolus vulgaris L.) C3 Non-Halophytes. Plant Physiol **95**: 628–635. doi:10.1104/pp.95.2.628

Bruland, K. W., and M. C. Lohan. 2003. Controls of Trace Metals in Seawater, p. 23–47. *In* Treatise on Geochemistry. Pergamon.

Buchfink, B., C. Xie, and D. H. Huson. 2015. Fast and sensitive protein alignment using DIAMOND. Nat Methods **12**: 59–60. doi:10.1038/nmeth.3176

Buck, K. N., M. C. Lohan, C. J. M. Berger, and K. W. Bruland. 2007. Dissolved iron speciation in two distinct river plumes and an estuary: Implications for riverine iron supply. Limnol. Oceanogr. **52**: 843–855. doi:10.4319/lo.2007.52.2.0843

Buck, K. N., J. Moffett, K. A. Barbeau, R. M. Bundy, Y. Kondo, and J. Wu. 2012. The organic complexation of iron and copper: an intercomparison of competitive ligand exchange-adsorptive cathodic stripping voltammetry (CLE-ACSV) techniques: GEOTRACES speciation intercomparison. Limnol. Oceanogr. Methods **10**: 496–515. doi:10.4319/lom.2012.10.496

Buck, K. N., P. N. Sedwick, B. Sohst, and C. A. Carlson. 2018. Organic complexation of iron in the eastern tropical South Pacific: Results from US GEOTRACES Eastern Pacific Zonal Transect (GEOTRACES cruise GP16). Marine Chemistry **201**: 229–241. doi:10.1016/j.marchem.2017.11.007

Buck, K. N., B. Sohst, and P. N. Sedwick. 2015. The organic complexation of dissolved iron along the U.S. GEOTRACES (GA03) North Atlantic Section. Deep Sea Research Part II: Topical Studies in Oceanography **116**: 152–165. doi:10.1016/j.dsr2.2014.11.016

Bundy, R. M., H. A. N. Abdulla, P. G. Hatcher, D. V. Biller, K. N. Buck, and K. A. Barbeau. 2015. Iron-binding ligands and humic substances in the San Francisco Bay estuary and estuarine-influenced shelf regions of coastal California. Marine Chemistry **173**: 183–194. doi:10.1016/j.marchem.2014.11.005

Bundy, R. M., D. V. Biller, K. N. Buck, K. W. Bruland, and K. A. Barbeau. 2014. Distinct pools of dissolved iron-binding ligands in the surface and benthic boundary layer of the California Current. Limnol. Oceanogr. **59**: 769–787. doi:10.4319/lo.2014.59.3.0769

Bundy, R. M., R. M. Boiteau, C. McLean, K. A. Turk-Kubo, M. R. McIlvin, M. A. Saito, B. A. S. Van Mooy, and D. J. Repeta. 2018. Distinct Siderophores Contribute to Iron Cycling in the Mesopelagic at Station ALOHA. Front. Mar. Sci. **5**: 1–15. doi:10.3389/fmars.2018.00061

Bundy, R. M., A. Tagliabue, N. J. Hawco, and others. 2020. Elevated sources of cobalt in the Arctic Ocean. Biogeosciences **17**: 4745–4767. doi:10.5194/bg-17-4745-2020

Capella-Gutierrez, S., J. M. Silla-Martinez, and T. Gabaldon. 2009. trimAl: a tool for automated alignment trimming in large-scale phylogenetic analyses. Bioinformatics **25**: 1972–1973. doi:10.1093/bioinformatics/btp348

Carkeet, C., S. R. Dueker, J. Lango, and others. 2006. Human vitamin B $_{12}$ absorption measurement by accelerator mass spectrometry using specifically labeled ^{14} C-cobalamin. Proc. Natl. Acad. Sci. U.S.A. **103**: 5694–5699. doi:10.1073/pnas.0601251103

Carlucci, A. F., and S. B. Silbernagel. 1966. Bioassay of seawater. III. Distribution of Vitamin B $_{12}$ in the Northeast Pacific Ocean. Limnol. Oceanogr. **11**: 642–646. doi:10.4319/lo.1966.11.4.0642

Carlucci, A. F., S. B. Silbernagel, and P. M. McNally. 1969. Influence of temperature and solar radiation on persistence of vitamin B12, thiamine, and biotin in seawater. Journal of Phycology **5.4**: 302–305.

Carrano, C. J., M. Jordan, H. Drechsel, and D. G. Schmid. 2001. Heterobactins: A new class of siderophores from Rhodococcus erythropolis IGTS8 containing both hydroxamate and catecholate donor groups. BioMetals **14**: 119–125.

Carroll, C. S., and M. M. Moore. 2018. Ironing out siderophore biosynthesis: a review of non-ribosomal peptide synthetase (NRPS)-independent siderophore synthetases. Critical Reviews in Biochemistry and Molecular Biology **53**: 356–381. doi:10.1080/10409238.2018.1476449

Chamlagain, B., T. A. Sugito, P. Deptula, M. Edelmann, S. Kariluoto, P. Varmanen, and V. Piironen. 2018. *In situ* production of active vitamin B12 in cereal matrices using *Propionibacterium freudenreichii*. Food Sci Nutr **6**: 67–76. doi:10.1002/fsn3.528

Cheng, H., N. F. Y. Tam, Y. Wang, S. Li, G. Chen, and Z. Ye. 2012. Effects of copper on growth, radial oxygen loss and root permeability of seedlings of the mangroves Bruguiera gymnorrhiza and Rhizophora stylosa. Plant and Soil **359**: 255–266. doi:10.1007/s11104-012-1171-1

Chiang, J. C. H. 2009. The Tropics in Paleoclimate. Annual Review of Earth and Planetary Sciences **37**: 263–297. doi:10.1146/annurev.earth.031208.100217

Chivall, D., D. M'Boule, D. Sinke-Schoen, J. S. Sinninghe Damsté, S. Schouten, and M. T. J. Van der Meer. 2014. The effects of growth phase and salinity on the hydrogen isotopic composition of alkenones produced by coastal haptophyte algae. Geochimica et Cosmochimica Acta **140**: 381–390. doi:10.1016/j.gca.2014.05.043

Cochlan, W. P. 2001. The heterotrophic bacterial response during a mesoscale iron enrichment experiment (IronEx II) in the eastern equatorial Pacific Ocean. Limnol. Oceanogr. **46**: 428–435. doi:10.4319/lo.2001.46.2.0428

Coesel, S. N., B. P. Durham, R. D. Groussman, S. K. Hu, D. A. Caron, R. L. Morales, F. Ribalet, and E. V. Armbrust. 2021. Diel transcriptional oscillations of light-sensitive regulatory elements in open-ocean eukaryotic plankton communities. Proc Natl Acad Sci USA **118**: e2011038118. doi:10.1073/pnas.2011038118

Cormier, M. A., R. A. Werner, P. E. Sauer, D. R. Gröcke, M. C. Leuenberger, T. Wieloch, J. Schleucher, and A. Kahmen. 2018. 2H-fractionations during the biosynthesis of carbohydrates and lipids imprint a metabolic signal on the δ2H values of plant organic compounds. New Phytologist **218**: 479–491. doi:10.1111/nph.15016

Cortese, M. S., A. Paszczynski, T. A. Lewis, J. L. Sebat, and R. L. Crawford. 2002. Metal chelating properties of pyridine-2,6-bis(thiocarboxylic acid) produced by Pseudomonas spp. and the biological activities of the formed complexes. BioMetals **15**: 103–20.

Csatorday, K., Z. Gombos, and B. Szalontai. 1984. Mn^{2+} and Co^{2+} toxicity in chlorophyll biosynthesis. Proc. Natl. Acad. Sci. U.S.A. **81**: 476–478. doi:10.1073/pnas.81.2.476

Dansgaard, W. 1964. Stable isotopes in precipitation. Tellus **16**: 436–468. doi:10.3402/tellusa.v16i4.8993

Darriba, D., G. L. Taboada, R. Doallo, and D. Posada. 2011. ProtTest 3: fast selection of best-fit models of protein evolution. Bioinformatics **27**: 1164–1165. doi:10.1093/bioinformatics/btr088

Das, S., and M. Ghose. 2003. Seed Structure and Germination Pattern of Some Indian Mangroves with Taxonomic Relevance. Science **48**: 287–298.

Debeljak, P., E. Toulza, S. Beier, S. Blain, and I. Obernosterer. 2019. Microbial iron metabolism as revealed by gene expression profiles in contrasted Southern Ocean regimes. Environ Microbiol **21**: 2360–2374. doi:10.1111/1462-2920.14621

Delwiche, C. F., and T. D. Sharkey. 1993. Rapid appearance of 13C in biogenic isoprene when 13CO2 is fed to intact leaves. Plant, Cell & Environment **16**: 587–591. doi:10.1111/j.1365-3040.1993.tb00907.x

Djaoudi, K., F. Van Wambeke, A. Barani, and others. 2020. Potential bioavailability of organic matter from atmospheric particles to marine heterotrophic bacteria. Biogeosciences **17**: 6271–6285. doi:10.5194/bg-17-6271-2020

Djoumbou-Feunang, Y., A. Pon, N. Karu, and others. 2019. CFM-ID 3.0: Significantly Improved ESI-MS/MS Prediction and Compound Identification. Metabolites **9**: 72. doi:10.3390/metabo9040072

Dortch, Q. 1990. The interaction between ammonium and nitrate uptake in phytoplankton. Mar. Ecol. Prog. Ser. **61**: 183–201. doi:10.3354/meps061183

Douglas, P. M. J., M. Pagani, M. Brenner, D. A. Hodell, and J. H. Curtis. 2012. Aridity and vegetation composition are important determinants of leaf-wax δD values in southeastern Mexico and Central America. Geochimica et Cosmochimica Acta **97**: 24–45. doi:10.1016/j.gca.2012.09.005

Doxey, A. C., D. A. Kurtz, M. D. Lynch, L. A. Sauder, and J. D. Neufeld. 2015. Aquatic metagenomes implicate Thaumarchaeota in global cobalamin production. ISME J **9**: 461–471. doi:10.1038/ismej.2014.142

Duckworth, O. W., J. R. Bargar, A. A. Jarzecki, O. Oyerinde, T. G. Spiro, and G. Sposito. 2009. The exceptionally stable cobalt(III)–desferrioxamine B complex. Marine Chemistry **113**: 114–122. doi:10.1016/j.marchem.2009.01.003

Duke, N. 2006. Australia's Mangroves: an authoritative guide to Australia's mangrove plants, University of Queensland, Brisbane, QLD, Australia.

Durham, B. P., A. K. Boysen, L. T. Carlson, and others. 2019. Sulfonate-based networks between eukaryotic phytoplankton and heterotrophic bacteria in the surface ocean. Nat Microbiol **4**: 1706–1715. doi:10.1038/s41564-019-0507-5

Eddy, S. R. 1998. Profile hidden Markov models. Bioinformatics **14**: 755–763. doi:10.1093/bioinformatics/14.9.755

Eddy, S. R. 2011. Accelerated Profile HMM Searches W.R. Pearson [ed.]. PLoS Comput Biol **7**: e1002195. doi:10.1371/journal.pcbi.1002195

Edgar, R. C. 2010. Search and clustering orders of magnitude faster than BLAST. Bioinformatics **26**: 2460–2461. doi:10.1093/bioinformatics/btq461

Eiler, A., S. Langenheder, S. Bertilsson, and L. J. Tranvik. 2003. Heterotrophic Bacterial Growth Efficiency and Community Structure at Different Natural Organic Carbon Concentrations. Appl Environ Microbiol **69**: 3701–3709. doi:10.1128/AEM.69.7.3701-3709.2003

Eley, Y., J. White, L. Dawson, M. Hren, and N. Pedentchouk. 2018. Variation in Hydrogen Isotope Composition Among Salt Marsh Plant Organic Compounds Highlights Biochemical Mechanisms Controlling Biosynthetic Fractionation. J. Geophys. Res. Biogeosci. **123**: 2645–2660. doi:10.1029/2018JG004403

Ellsworth, P. V., P. Z. Ellsworth, W. T. Anderson, and L. S. L. Sternberg. 2013. The role of effective leaf mixing length in the relationship between the δ18O of stem cellulose and source water across a salinity gradient. Plant, Cell and Environment **36**: 138–148. doi:10.1111/j.1365-3040.2012.02562.x

Ellwood, M. J., and C. M. G. van den Berg. 2001. Determination of organic complexation of cobalt in seawater by cathodic stripping voltammetry. Marine Chemistry **75**: 33–47. doi:10.1016/S0304-4203(01)00024-X

El-Sheekh, M. M., A. H. El-Naggar, M. E. H. Osman, and E. El-Mazaly. 2003. Effect of cobalt on growth, pigments and the photosynthetic electron transport in Monoraphidium minutum and Nitzchia perminuta. Braz. J. Plant Physiol. **15**: 159–166. doi:10.1590/S1677-04202003000300005

Englebrecht, A. C., and J. P. Sachs. 2005. Determination of sediment provenance at drift sites using hydrogen isotopes and unsaturation ratios in alkenones. Geochimica et Cosmochimica Acta **69**: 4253–4265. doi:10.1016/j.gca.2005.04.011

Ewe, S. M. L., L. D. S. L. Sternberg, and D. L. Childers. 2007. Seasonal plant water uptake patterns in the saline southeast Everglades ecotone. Oecologia **152**: 607–616. doi:10.1007/s00442-007-0699-x

Fairbanks, R. G., M. N. Evans, J. L. Rubenstone, R. A. Mortlock, K. Broad, M. D. Moore, and C. D. Charles. 1997. Evaluating climate indices and their geochemical proxies measured in corals. Coral Reefs **16**: S93–S100. doi:10.1007/s003380050245

Fallahzadeh, V., M. Ahmadzadeh, and R. Sharifi. 2010. Growth and pyoverdine production kinetics of Pseudomonas aeruginosa 7NSK2 in an experimental fermentor. Journal of Agricultural Technology **6**: 107–115.

Fang, H., J. Kang, and D. Zhang. 2017. Microbial production of vitamin B12: a review and future perspectives. Microb Cell Fact **16**: 15. doi:10.1186/s12934-017-0631-y

Farquhar, G. D., J. R. Ehleringer, and K. T. Hubick. 1989. Carbon Isotope Discrimination and Photosynthesis. Annual Review of Plant Physiology and Plant Molecular Biology **40**: 503–537.

Farquhar, G., M. O'Leary, and J. Berry. 1982. On the Relationship Between Carbon Isotope Discrimination and the Intercellular Carbon Dioxide Concentration in Leaves. Australian Journal of Plant Physiology **9**: 121. doi:10.1071/PP9820121

Feakins, S. J., and A. L. Sessions. 2010. Controls on the D/H ratios of plant leaf waxes in an arid ecosystem. Geochimica et Cosmochimica Acta **74**: 2128–2141. doi:10.1016/j.gca.2010.01.016

Field, C. B., M. J. Behrenfeld, J. T. Randerson, and P. Falkowski. 1998. Primary Production of the Biosphere: Integrating Terrestrial and Oceanic Components. Science **281**: 237–240. doi:10.1126/science.281.5374.237

Finn, R. D., A. Bateman, J. Clements, and others. 2014. Pfam: the protein families database. Nucl. Acids Res. **42**: D222–D230. doi:10.1093/nar/gkt1223

Flato, G., J. Marotzke, P. Abiodun, and others. 2013. Evaluation of Climate Models, p. 741–866. *In* Climate Change 2013:The Physical Science Basis. Contribution of Working Group I to the Fifth Assessment Report of the Intergovernmental Panel on Climate Change [Stocker, T.F., D. Qin, G.-K. Plattner, M. Tignor, S.K. Allen, J. Boschung, A. Nauels, Y. Xia, V. Bex and P.M. Midgley (eds.)]. Cambridge University Press.

Follett, C. L., S. Dutkiewicz, G. Forget, B. B. Cael, and M. J. Follows. 2021. Moving ecological and biogeochemical transitions across the North Pacific. Limnol Oceanogr **66**: 2442–2454. doi:10.1002/lno.11763

Freimuth, E. J., A. F. Diefendorf, and T. V. Lowell. 2017. Hydrogen isotopes of n-alkanes and n-alkanoic acids as tracers of precipitation in a temperate forest and implications for paleorecords. Geochimica et Cosmochimica Acta **206**: 166–183. doi:10.1016/j.gca.2017.02.027

Gao, L., A. Burnier, and Y. Huang. 2012. Quantifying instantaneous regeneration rates of plant leaf waxes using stable hydrogen isotope labeling: Quantifying regeneration rates of plant leaf waxes. Rapid Commun. Mass Spectrom. **26**: 115–122. doi:10.1002/rcm.5313

Garber, A. I., K. H. Nealson, A. Okamoto, S. M. McAllister, C. S. Chan, R. A. Barco, and N. Merino. 2020. FeGenie: A Comprehensive Tool for the Identification of Iron Genes and Iron Gene Neighborhoods in Genome and Metagenome Assemblies. Front. Microbiol. **11**: 37. doi:10.3389/fmicb.2020.00037

Gauglitz, J. M., R. M. Boiteau, C. McLean, L. Babcock-Adams, M. R. McIlvin, D. M. Moran, D. J. Repeta, and M. A. Saito. 2021. Dynamic proteome response of a marine Vibrio to a gradient of iron and ferrioxamine bioavailability. Marine Chemistry **229**: 103913. doi:10.1016/j.marchem.2020.103913

GEOTRACES Intermediate Data Product Group. 2021. The GEOTRACES Intermediate Data Product 2021 (IDP2021).doi:.5285/cf2d9ba9-d51d-3b7c-e053-8486abc0f5fd

Gilbert, J. A., J. A. Steele, J. G. Caporaso, and others. 2012. Defining seasonal marine microbial community dynamics. ISME J **6**: 298–308. doi:10.1038/ismej.2011.107

Giovagnetti, V., C. Brunet, F. Conversano, F. Tramontano, I. Obernosterer, C. Ridame, and C. Guieu. 2013. Assessing the role of dust deposition on phytoplankton ecophysiology and succession in a low-nutrient low-chlorophyll ecosystem: a mesocosm experiment in the Mediterranean Sea. Biogeosciences **10**: 2973–2991. doi:10.5194/bg-10-2973-2013

Giri, C., E. Ochieng, L. L. Tieszen, Z. Zhu, A. Singh, T. Loveland, J. Masek, and N. Duke. 2011. Status and distribution of mangrove forests of the world using earth observation satellite data. Global Ecology and Biogeography **20**: 154–159. doi:10.1111/j.1466-8238.2010.00584.x

Gledhill, M., and C. M. G. van den Berg. 1994. Determination of complexation of iron(III) with natural organic complexing ligands in seawater using cathodic stripping voltammetry. Marine Chemistry **47**: 41–54. doi:10.1016/0304-4203(94)90012-4

Gledhill, M., and K. N. Buck. 2012. The organic complexation of iron in the marine environment: a review. Front. Microbio. **3**. doi:10.3389/fmicb.2012.00069

Glibert, P. M., and G. M. Berg. 2009. Nitrogen form, fate and phytoplankton composition, p. 183–189. *In* Experimental ecosystems and scale: Tools for understanding and managing coastal ecosystems. Springer New York, NY.

Glibert, P. M., F. P. Wilkerson, R. C. Dugdale, and others. 2016. Pluses and minuses of ammonium and nitrate uptake and assimilation by phytoplankton and implications for productivity and community composition, with emphasis on nitrogen-enriched conditions: Pluses and minuses of NH4+ *and* NO3−. Limnol. Oceanogr. **61**: 165–197. doi:10.1002/lno.10203

Gokhale, M. V., and N. S. Chavan. 2002. Germination and growth performance of Xylocarpus granatum.

Gradoville, M. R., H. Farnelid, A. E. White, and others. 2020. Latitudinal constraints on the abundance and activity of the cyanobacterium UCYN-A and other marine diazotrophs in the North Pacific. Limnol Oceanogr **65**: 1858–1875. doi:10.1002/lno.11423

Greer, L., and P. K. Swart. 2006. Decadal cyclicity of regional mid-Holocene precipitation: Evidence from Dominican coral proxies. Paleoceanography **21**: 1–17. doi:10.1029/2005PA001166

Gruber, K., B. Puffer, and B. Kräutler. 2011. Vitamin B12-derivatives—enzyme cofactors and ligands of proteins and nucleic acids. Chem. Soc. Rev. **40**: 4346. doi:10.1039/c1cs15118e

Guenther, F., B. Aichner, R. Siegwolf, B. Xu, T. Yao, and G. Gleixner. 2013. A synthesis of hydrogen isotope variability and its hydrological significance at the Qinghai-Tibetan Plateau. Quaternary International **313–314**: 3–16. doi:10.1016/j.quaint.2013.07.013

Gulick, A. M. 2017. Nonribosomal peptide synthetase biosynthetic clusters of ESKAPE pathogens. Nat. Prod. Rep. **34**: 981–1009. doi:10.1039/C7NP00029D

Gunawan, S., R. Darmawan, M. Nanda, A. D. Setiawan, and H. Fansuri. 2013. Proximate composition of Xylocarpus moluccensis seeds and their oils. Industrial Crops and Products **41**: 107–112. doi:10.1016/j.indcrop.2012.04.010

Guy, R. D., P. G. Warne, and D. M. Reid. 1989. Stable Carbon Isotope Ratio as an Index of Water-Use Efficiency in C3 Halophytes—Possible Relationship to Strategies for Osmotic Adjustment, p. 55–75. *In* P.W. Rundel, J.R. Ehleringer, and K.A. Nagy [eds.], Stable Isotopes in Ecological Research. Springer New York.

Haft, D. H. 2003. The TIGRFAMs database of protein families. Nucleic Acids Research **31**: 371–373. doi:10.1093/nar/gkg128

Hantke, K., G. Nicholson, W. Rabsch, and G. Winkelmann. 2003. Salmochelins, siderophores of *Salmonella enterica* and uropathogenic *Escherichia coli* strains, are recognized by the outer membrane receptor IroN. Proc. Natl. Acad. Sci. U.S.A. **100**: 3677–3682. doi:10.1073/pnas.0737682100

Hassler, C. S., and V. Schoemann. 2009. Bioavailability of organically bound Fe to model phytoplankton of the Southern Ocean. Biogeosciences **6**: 2281–2296.

Hassler, C. S., V. Schoemann, M. Boye, A. Tagliabue, M. Rozmarynowycz, and R. M. L. McKay. 2012. Iron bioavailability in the Southern Ocean. Oceanography and Marine Biology: An Annual Review **50**: 1–64.

Hawco, N. J., M. M. McIlvin, R. M. Bundy, and others. 2020. Minimal cobalt metabolism in the marine cyanobacterium *Prochlorococcus*. Proc. Natl. Acad. Sci. U.S.A. **117**: 15740–15747. doi:10.1073/pnas.2001393117

Hawco, N. J., D. C. Ohnemus, J. A. Resing, B. S. Twining, and M. A. Saito. 2016. A dissolved cobalt plume in the oxygen minimum zone of the eastern tropical South Pacific. Biogeosciences **13**: 5697–5717. doi:10.5194/bg-13-5697-2016

He, D., S. N. Ladd, J. P. Sachs, and R. Jaffé. 2017. Inverse relationship between salinity and2H/1H fractionation in leaf wax n-alkanes from Florida mangroves. Organic Geochemistry **110**: 1–12. doi:10.1016/j.orggeochem.2017.04.007

Heal, K. R., B. P. Durham, A. K. Boysen, and others. 2021. Marine Community Metabolomes Carry Fingerprints of Phytoplankton Community Composition. mSystems **6**: 532627 bytes. doi:10.5061/DRYAD.BRV15DV8S

Heal, K. R., N. A. Kellogg, L. T. Carlson, R. M. Lionheart, and A. E. Ingalls. 2019. Metabolic Consequences of Cobalamin Scarcity in the Diatom Thalassiosira pseudonana as Revealed Through Metabolomics. Protist **170**: 328–348. doi:10.1016/j.protis.2019.05.004

Heal, K. R., A. E. Maloney, A. E. Ingalls, and R. M. Bundy. 2022. Diverse arsenic-containing lipids in the surface ocean. Limnol Oceanogr Letters **7**: 43–51. doi:10.1002/lol2.10216

Heal, K. R., W. Qin, S. A. Amin, A. H. Devol, J. W. Moffett, E. V. Armbrust, D. A. Stahl, and A. E. Ingalls. 2018. Accumulation of NO_2 -cobalamin in nutrient-stressed ammonia-oxidizing archaea and in the oxygen deficient zone of the eastern tropical North Pacific. Environmental Microbiology Reports **10**: 453–457. doi:10.1111/1758-2229.12664

Heal, K. R., W. Qin, F. Ribalet, and others. 2017. Two distinct pools of B_{12} analogs reveal community interdependencies in the ocean. Proc. Natl. Acad. Sci. U.S.A. **114**: 364–369. doi:10.1073/pnas.1608462114

Heinzelmann, S. M., D. Chivall, D. M'Boule, D. Sinke-Schoen, L. Villanueva, J. S. S. Damsté, S. Schouten, and M. T. J. Van der Meer. 2015a. Comparison of the effect of salinity on the D/H ratio of fatty acids of heterotrophic and photoautotrophic microorganisms. FEMS Microbiology Letters **362**: 1–6. doi:10.1093/femsle/fnv065

Heinzelmann, S. M., L. Villanueva, D. Sinke-Schoen, J. S. Sinninghe Damst??, S. Schouten, and M. T. J. van der Meer. 2015b. Impact of metabolism and growth phase on the hydrogen isotopic composition of microbial fatty acids. Frontiers in Microbiology **6**: 1–11. doi:10.3389/fmicb.2015.00408

Helliwell, K. E., A. D. Lawrence, A. Holzer, and others. 2016. Cyanobacteria and Eukaryotic Algae Use Different Chemical Variants of Vitamin B12. Current Biology **26**: 999–1008. doi:10.1016/j.cub.2016.02.041

Helliwell, K. E., G. L. Wheeler, K. C. Leptos, R. E. Goldstein, and A. G. Smith. 2011. Insights into the Evolution of Vitamin B12 Auxotrophy from Sequenced Algal Genomes. Molecular Biology and Evolution **28**: 2921–2933. doi:10.1093/molbev/msr124

Herndl, G., H. Agogué, F. Baltar, T. Reinthaler, E. Sintes, and M. Varela. 2008. Regulation of aquatic microbial processes: the 'microbial loop' of the sunlit surface waters and the dark ocean dissected. Aquat. Microb. Ecol. **53**: 59–68. doi:10.3354/ame01225

Hider, R. C., and X. Kong. 2010. Chemistry and biology of siderophores. Nat. Prod. Rep. **27**: 637. doi:10.1039/b906679a

Hogle, S. L. 2019. MARMICRODB database for taxonomic classification of (marine) metagenomes (1.00) [Data set].doi:10.5281/zenodo.3520509

Holinsworth, B., and J. D. Martin. 2009. Siderophore production by marine-derived fungi. Biometals **22**: 625–632. doi:10.1007/s10534-009-9239-y

Hopkinson, B. M., and K. A. Barbeau. 2012. Iron transporters in marine prokaryotic genomes and metagenomes: Iron transporters in marine prokaryotes. Environmental Microbiology **14**: 114–128. doi:10.1111/j.1462-2920.2011.02539.x

Huang, Y., B. Shuman, Y. Wang, and T. Webb. 2004. Hydrogen isotope ratios of individual lipids in lake sediments as novel tracers of climatic and environmental change: A surface sediment test. Journal of Paleolimnology **31**: 363–375. doi:10.1023/B:JOPL.0000021855.80535.13

Hunter, K. A., and P. W. Boyd. 2007. Iron-binding ligands and their role in the ocean biogeochemistry of iron. Environ. Chem. **4**: 221. doi:10.1071/EN07012

Hutchins, D. A., A. E. Witter, A. Butler, and G. W. Luther. 1999. Competition among marine phytoplankton for different chelated iron species. Nature **400**: 858–861. doi:10.1038/23680

Jennerjahn, T. C., and V. Ittekkot. 2002. Relevance of mangroves for the production and deposition of organic matter along tropical continental margins. Naturwissenschaften **89**: 23–30. doi:10.1007/s00114-001-0283-x

Jiang, Q., D. Roche, T. A. Monaco, and S. Durham. 2006. Gas exchange, chlorophyll fluorescence parameters and carbon isotope discrimination of 14 barley genetic lines in response to salinity. Field Crops Research **96**: 269–278. doi:10.1016/j.fcr.2005.07.010

Joglar, V., A. Prieto, E. Barber-Lluch, M. Hernández-Ruiz, E. Fernández, and E. Teira. 2020. Spatial and temporal variability in the response of phytoplankton and prokaryotes to B-vitamin amendments in an upwelling system. Biogeosciences **17**: 2807–2823. doi:10.5194/bg-17-2807-2020

Johnson, K. S., R. M. Gordon, and K. H. Coale. 1997. What controls dissolved iron concentrations in the world ocean? Marine Chemistry **57**: 137–161. doi:10.1016/S0304-4203(97)00043-1

Juranek, L. W., A. E. White, M. Dugenne, and others. 2020. The Importance of the Phytoplankton “Middle Class” to Ocean Net Community Production. Global Biogeochem. Cycles **34**. doi:10.1029/2020GB006702

Kahmen, A., T. E. Dawson, A. Vieth, and D. Sachse. 2011a. Leaf wax n-alkane δD values are determined early in the ontogeny of Populus trichocarpa leaves when grown under controlled environmental conditions. Plant, Cell and Environment **34**: 1639–1651. doi:10.1111/j.1365-3040.2011.02360.x

Kahmen, A., B. Hoffmann, E. Schefuß, S. K. Arndt, L. A. Cernusak, J. B. West, and D. Sachse. 2013. Leaf water deuterium enrichment shapes leaf wax n-alkane δD values of

angiosperm plants II: Observational evidence and global implications. Geochimica et Cosmochimica Acta **111**: 50–63. doi:10.1016/j.gca.2012.09.004

Kahmen, A., D. Sachse, S. K. Arndt, K. P. Tu, H. Farrington, P. M. Vitousek, and T. E. Dawson. 2011b. Cellulose δ ^{18} O is an index of leaf-to-air vapor pressure difference (VPD) in tropical plants. Proceedings of the National Academy of Sciences **108**: 1981–1986. doi:10.1073/pnas.1018906108

Kasai, M., K. Koide, and Y. Ichikawa. 2012. Effect of Pot Size on Various Characteristics Related to Photosynthetic Matter Production in Soybean Plants. International Journal of Agronomy **2012**: 1–7. doi:10.1155/2012/751731

Keeling, P. J., F. Burki, H. M. Wilcox, and others. 2014. The Marine Microbial Eukaryote Transcriptome Sequencing Project (MMETSP): Illuminating the Functional Diversity of Eukaryotic Life in the Oceans through Transcriptome Sequencing R.G. Roberts [ed.]. PLoS Biol **12**: e1001889. doi:10.1371/journal.pbio.1001889

Kem, M. P., H. K. Zane, S. D. Springer, J. M. Gauglitz, and A. Butler. 2014. Amphiphilic siderophore production by oil-associating microbes. Metallomics **6**: 1150–1155. doi:10.1039/C4MT00047A

King, A. L., S. A. Sañudo-Wilhelmy, K. Leblanc, D. A. Hutchins, and F. Fu. 2011. CO2 and vitamin B12 interactions determine bioactive trace metal requirements of a subarctic Pacific diatom. ISME J **5**: 1388–1396. doi:10.1038/ismej.2010.211

Koch, B. P., J. Harder, R. J. Lara, and G. Kattner. 2005. The effect of selective microbial degradation on the composition of mangrove derived pentacyclic triterpenols in surface sediments. Organic Geochemistry **36**: 273–285. doi:10.1016/j.orggeochem.2004.07.019

Koch, F., T. K. Hattenrath-Lehmann, J. A. Goleski, S. Sañudo-Wilhelmy, N. S. Fisher, and C. J. Gobler. 2012. Vitamin B1 and B12 Uptake and Cycling by Plankton Communities in Coastal Ecosystems. Front. Microbio. **3**. doi:10.3389/fmicb.2012.00363

Konecky, B. L., J. M. Russell, J. R. Rodysill, M. Vuille, S. Bijaksana, and Y. Huang. 2013. Intensification of southwestern Indonesian rainfall over the past millennium. Geophysical Research Letters **40**: 386–391. doi:10.1029/2012GL054331

Kraemer, S. M., A. Butler, P. Borer, and J. Cervini-Silva. 2005. Siderophores and the Dissolution of Iron-Bearing Minerals in Marine Systems. Reviews in Mineralogy and Geochemistry **59**: 53–84. doi:10.2138/rmg.2005.59.4

Kramer, J., Ö. Özkaya, and R. Kümmerli. 2020. Bacterial siderophores in community and host interactions. Nat Rev Microbiol **18**: 152–163. doi:10.1038/s41579-019-0284-4

Krauss, K. W., and J. A. Allen. 2003. Influences of salinity and shade on seedling photosynthesis and growth of two mangrove species, Rhizophora mangle and Bruguiera sexangula, introduced to Hawaii. Aquatic Botany **77**: 311–324. doi:10.1016/j.aquabot.2003.08.004

Krewulak, K. D., and H. J. Vogel. 2008. Structural biology of bacterial iron uptake. Biochimica et Biophysica Acta (BBA) - Biomembranes **1778**: 1781–1804. doi:10.1016/j.bbamem.2007.07.026

Kügler, S., R. E. Cooper, J. Boessneck, K. Küsel, and T. Wichard. 2020. Rhizobactin B is the preferred siderophore by a novel Pseudomonas isolate to obtain iron from dissolved organic matter in peatlands. Biometals **33**: 415–433. doi:10.1007/s10534-020-00258-w

Ladd, N. S., and J. P. Sachs. 2015a. Influence of salinity on hydrogen isotope fractionation in Rhizophora mangroves from Micronesia. Geochimica et Cosmochimica Acta **168**: 206–221. doi:10.1016/j.gca.2015.07.004

Ladd, S. N., D. B. Nelson, C. J. Schubert, and N. Dubois. 2018. Lipid compound classes display diverging hydrogen isotope responses in lakes along a nutrient gradient. Geochimica et Cosmochimica Acta **237**: 103–119. doi:10.1016/j.gca.2018.06.005

Ladd, S. N., and J. P. Sachs. 2012. Inverse relationship between salinity and n-alkane δD values in the mangrove Avicennia marina. Organic Geochemistry **48**: 25–36. doi:10.1016/j.orggeochem.2012.04.009

Ladd, S. N., and J. P. Sachs. 2013. Positive correlation between salinity and n-alkane δ13C values in the mangrove Avicennia marina. Organic Geochemistry **64**: 1–8. doi:10.1016/j.orggeochem.2013.08.011

Ladd, S. N., and J. P. Sachs. 2015b. Hydrogen isotope response to changing salinity and rainfall in Australian mangroves. Plant Cell and Environment **38**: 2674–2687. doi:10.1111/pce.12579

Ladd, S. N., and J. P. Sachs. 2017. 2H/1H fractionation in lipids of the mangrove Bruguiera gymnorhiza increases with salinity in marine lakes of Palau. Geochimica et Cosmochimica Acta **204**: 300–312. doi:10.1016/j.gca.2017.01.046

Lagerström, M. E., M. P. Field, M. Séguret, L. Fischer, S. Hann, and R. M. Sherrell. 2013. Automated on-line flow-injection ICP-MS determination of trace metals (Mn, Fe, Co, Ni, Cu and Zn) in open ocean seawater: Application to the GEOTRACES program. Marine Chemistry **155**: 71–80. doi:10.1016/j.marchem.2013.06.001

Laglera, L. M., and C. M. G. van den Berg. 2009. Evidence for geochemical control of iron by humic substances in seawater. Limnol. Oceanogr. **54**: 610–619. doi:10.4319/lo.2009.54.2.0610

Lambs, L., E. Muller, and F. Fromard. 2008. Mangrove trees growing in a very saline condition but not using seawater. Rapid Commun. Mass Spectrom. **22**: 2835–2843. doi:10.1002/rcm.3676

Liang, J., J. S. Wright, X. Cui, L. Sternberg, W. Gan, and G. Lin. 2018. Leaf anatomical traits determine the ^{18} O enrichment of leaf water in coastal halophytes: Special 18O enrichment in mangrove leaf water. Plant Cell Environ **41**: 2744–2757. doi:10.1111/pce.13398

Lin, G. H., and L. Sternberg. 1992. Effect of Growth Form, Salinity, Nutrient and Sulfide on Photosynthesis, Carbon Isotope Discrimination and Growth of Red Mangrove (Rhizophora mangle L.). Functional Plant Biology **19**: 509–517. doi:10.1071/PP9920509

Lin, G., and L. Sternberg. 1993. Hydrogen isotopic fractionation by plant roots during water uptake in coastal wetland plants, p. 497–510. *In* Ehleringer, J.R., Hall, A.E., Farquhar, G.D. (Eds.), Stable Isotopes and Plant Carbon-Water Relations. Academic Press, San Diego.

Lis, H., Y. Shaked, C. Kranzler, N. Keren, and F. M. M. Morel. 2015. Iron bioavailability to phytoplankton: an empirical approach. ISME J **9**: 1003–1013. doi:10.1038/ismej.2014.199

Liu, X., and F. J. Millero. 2002. The solubility of iron in seawater. Marine Chemistry **77**: 43–54. doi:10.1016/S0304-4203(01)00074-3

Lovelock, C. E., R. Reef, and M. C. Ball. 2017. Isotopic signatures of stem water reveal differences in water sources accessed by mangrove tree species. Hydrobiologia **803**: 133–145. doi:10.1007/s10750-017-3149-8

Lu, X., K. R. Heal, A. E. Ingalls, A. C. Doxey, and J. D. Neufeld. 2020. Metagenomic and chemical characterization of soil cobalamin production. ISME J **14**: 53–66. doi:10.1038/s41396-019-0502-0

Magoc, T., and S. L. Salzberg. 2011. FLASH: fast length adjustment of short reads to improve genome assemblies. Bioinformatics **27**: 2957–2963. doi:10.1093/bioinformatics/btr507

Mahowald, N. M., D. S. Hamilton, K. R. M. Mackey, J. K. Moore, A. R. Baker, R. A. Scanza, and Y. Zhang. 2018. Aerosol trace metal leaching and impacts on marine microorganisms. Nat Commun **9**: 2614. doi:10.1038/s41467-018-04970-7

Majtan, T., F. E. Frerman, and J. P. Kraus. 2011. Effect of cobalt on Escherichia coli metabolism and metalloporphyrin formation. Biometals **24**: 335–347. doi:10.1007/s10534-010-9400-7

Maldonado, M. T., and N. M. Price. 1999. Utilization of iron bound to strong organic ligands by plankton communities in the subarctic Pacific Ocean. Deep Sea Research Part II: Topical Studies in Oceanography **46**: 2447–2473.

Maloney, A. E., A. L. C. Shinneman, K. Hemeon, and J. P. Sachs. 2016. Exploring lipid2H/1H fractionation mechanisms in response to salinity with continuous cultures of the diatom Thalassiosira pseudonana. Organic Geochemistry **101**: 154–165. doi:10.1016/j.orggeochem.2016.08.015

Marañén, E., A. Fernández, B. Mouriño-Carballido, and others. 2010. Degree of oligotrophy controls the response of microbial plankton to Saharan dust. Limnol. Oceanogr. **55**: 2339–2352. doi:10.4319/lo.2010.55.6.2339

Marín, I., S. Nunes, E. D. Sánchez-Pérez, and others. 2017. Anthropogenic versus mineral aerosols in the stimulation of microbial planktonic communities in coastal waters of the

northwestern Mediterranean Sea. Science of The Total Environment **574**: 553–568. doi:10.1016/j.scitotenv.2016.09.005

Marín-Beltrán, I., J. B. Logue, A. F. Andersson, and F. Peters. 2019. Atmospheric Deposition Impact on Bacterial Community Composition in the NW Mediterranean. Front. Microbiol. **10**: 858. doi:10.3389/fmicb.2019.00858

Martin, J. H., M. Gordon, and S. E. Fitzwater. 1991. The case for iron. Limnol. Oceanogr. **36**: 1793–1802. doi:10.4319/lo.1991.36.8.1793

Martin, K. C., D. Bruhn, C. E. Lovelock, I. C. Feller, J. R. Evans, and M. C. Ball. 2010. Nitrogen fertilization enhances water-use efficiency in a saline environment. Plant, Cell and Environment **33**: 344–357. doi:10.1111/j.1365-3040.2009.02072.x

Martinez, J. S., J. N. Carter-Franklin, E. L. Mann, J. D. Martin, M. G. Haygood, and A. Butler. 2003. Structure and membrane affinity of a suite of amphiphilic siderophores produced by a marine bacterium. Proceedings of the National Academy of Sciences **100**: 3754–3759. doi:10.1073/pnas.0637444100

Mas, A., S. Jamshidi, Y. Lagadeuc, D. Eveillard, and P. Vandenkoornhuyse. 2016. Beyond the Black Queen Hypothesis. ISME J **10**: 2085–2091. doi:10.1038/ismej.2016.22

Matsen, F. A., R. B. Kodner, and E. V. Armbrust. 2010. pplacer: linear time maximum-likelihood and Bayesian phylogenetic placement of sequences onto a fixed reference tree. BMC Bioinformatics **11**: 538. doi:10.1186/1471-2105-11-538

Mawji, E., M. Gledhill, J. A. Milton, and others. 2008. Hydroxamate Siderophores: Occurrence and Importance in the Atlantic Ocean. Environ. Sci. Technol. **42**: 8675–8680. doi:10.1021/es801884r

M’boule, D., D. Chivall, D. Sinke-Schoen, J. S. Sinninghe Damsté, S. Schouten, and M. T. J. Van der Meer. 2014. Salinity dependent hydrogen isotope fractionation in alkenones produced by coastal and open ocean haptophyte algae. Geochimica et Cosmochimica Acta **130**: 126–135. doi:10.1016/j.gca.2014.01.029

van der Meer, M. T. J., A. Benthien, K. L. French, and others. 2015. Large effect of irradiance on hydrogen isotope fractionation of alkenones in Emiliania huxleyi. Geochimica et Cosmochimica Acta **160**: 16–24. doi:10.1016/j.gca.2015.03.024

Menzel, D. W., and J. P. Spaeth. 1962. OCCURRENCE OF VITAMIN B $_{12}$ IN THE SARGASSO SEA1. Limnol. Oceanogr. **7**: 151–154. doi:10.4319/lo.1962.7.2.0151

Menzel, P., K. L. Ng, and A. Krogh. 2016. Fast and sensitive taxonomic classification for metagenomics with Kaiju. Nat Commun **7**: 11257. doi:10.1038/ncomms11257

Moeck, G. S., and J. W. Coulton. 2002. TonB-dependent iron acquisition: mechanisms of siderophore-mediated active transport: TonB-dependent iron acquisition. Molecular Microbiology **28**: 675–681. doi:10.1046/j.1365-2958.1998.00817.x

Mohamed, K. N., and M. Gledhill. 2017. Identification and Quantification of Siderophore Type Chelators in the Incubation Samples. Journal of Research Analytica **3**: 96–107.

Moore, C. M., M. M. Mills, K. R. Arrigo, and others. 2013. Processes and patterns of oceanic nutrient limitation. Nature Geosci **6**: 701–710. doi:10.1038/ngeo1765

Moore, J. K., S. C. Doney, and K. Lindsay. 2004. Upper ocean ecosystem dynamics and iron cycling in a global three-dimensional model. Global Biogeochem. Cycles **18**. doi:10.1029/2004GB002220

Morel, F. M. M., A. B. Kustka, and Y. Shaked. 2008. The role of unchelated Fe in the iron nutrition of phytoplankton. Limnol. Oceanogr. **53**: 400–404. doi:10.4319/lo.2008.53.1.0400

Morel, F. M. M., A. J. Milligan, and M. A. Saito. 2014. Marine Bioinorganic Chemistry: The Role of Trace Metals in the Oceanic Cycles of Major Nutrients, p. 123–150. *In* Treatise on Geochemistry. Elsevier.

Morel, F. M. M., and N. M. Price. 2003. The Biogeochemical Cycles of Trace Metals in the Oceans. Science **300**: 944–947. doi:10.1126/science.1083545

Morris, J. J., R. E. Lenski, and E. R. Zinser. 2012. The Black Queen Hypothesis: Evolution of Dependencies through Adaptive Gene Loss. mBio **3**. doi:10.1128/mBio.00036-12

Müller, S. I., M. Valdebenito, and K. Hantke. 2009. Salmochelin, the long-overlooked catecholate siderophore of Salmonella. Biometals **22**: 691–695. doi:10.1007/s10534-009-9217-4

Naidoo, G., and D. J. von Willert. 1995. Diurnal gas exchange characteristics and water use efficiency of three salt-secreting mangroves at low and high salinities. Hydrobiologia **295**: 13–22. doi:10.1007/BF00029106

Nef, C., C. Henry, É. Nicolau, and others. 2020. Cobalamin Scarcity Modifies Carbon Allocation and Impairs DMSP Production Through Methionine Metabolism in the Haptophyte Microalgae *Tisochrysis lutea*. Front. Mar. Sci. **7**: 569560. doi:10.3389/fmars.2020.569560

Neilands, J. B. 1981. Microbial Iron Compounds. Annu. Rev. Biochem. **50**: 715–731. doi:10.1146/annurev.bi.50.070181.003435

Nelson, D. B., and J. P. Sachs. 2014. The influence of salinity on D/H fractionation in dinosterol and brassicasterol from globally distributed saline and hypersaline lakes. Geochimica et Cosmochimica Acta **133**: 325–339. doi:10.1016/j.gca.2014.03.007

Nelson, D. B., and J. P. Sachs. 2016. Galápagos hydroclimate of the Common Era from paired microalgal and mangrove biomarker ^{2}H/^{1}H values. Proceedings of the National Academy of Sciences **113**: 3476–3481. doi:10.1073/pnas.1516271113

NeSmith, D. S., and J. R. Duval. 1998. The Effect of Container Size. horttech **8**: 495–498. doi:10.21273/HORTTECH.8.4.495

Newberry, S. L., A. Kahmen, P. Dennis, and A. Grant. 2015. n-Alkane biosynthetic hydrogen isotope fractionation is not constant throughout the growing season in the riparian tree Salix viminalis. Geochimica et Cosmochimica Acta **165**: 75–85. doi:10.1016/j.gca.2015.05.001

Niedermeyer, E. M., E. Schefuß, A. L. Sessions, S. Mulitza, G. Mollenhauer, M. Schulz, and G. Wefer. 2010. Orbital- and millennial-scale changes in the hydrologic cycle and vegetation in the western African Sahel: Insights from individual plant wax δD and δ13C. Quaternary Science Reviews **29**: 2996–3005. doi:10.1016/j.quascirev.2010.06.039

Noble, A. E., C. H. Lamborg, D. C. Ohnemus, and others. 2012. Basin-scale inputs of cobalt, iron, and manganese from the Benguela-Angola front to the South Atlantic Ocean. Limnol. Oceanogr. **57**: 989–1010. doi:10.4319/lo.2012.57.4.0989

Noble, A. E., D. C. Ohnemus, N. J. Hawco, P. J. Lam, and M. A. Saito. 2017. Coastal sources, sinks and strong organic complexation of dissolved cobalt within the US North Atlantic GEOTRACES transect GA03. Biogeosciences **14**: 2715–2739. doi:10.5194/bg-14-2715-2017

Noinaj, N., M. Guillier, T. J. Barnard, and S. K. Buchanan. 2010. TonB-Dependent Transporters: Regulation, Structure, and Function. Annu. Rev. Microbiol. **64**: 43–60. doi:10.1146/annurev.micro.112408.134247

Oliver, J. L., R. T. Barber, W. O. Smith, and H. W. Ducklow. 2004. The heterotrophic bacterial response during the Southern Ocean Iron Experiment (SOFeX). Limnol. Oceanogr. **49**: 2129–2140. doi:10.4319/lo.2004.49.6.2129

Owen, S. C., M. Lee, and C. B. Grissom. 2011. Ultra-Performance Liquid Chromatographic Separation and Mass Spectrometric Quantitation of Physiologic Cobalamins. Journal of Chromatographic Science **49**: 228–233. doi:10.1093/chrsci/49.3.228

Pahnke, K., J. P. Sachs, L. Keigwin, A. Timmermann, and S. P. Xie. 2007. Eastern tropical Pacific hydrologic changes during the past 27,000 years from D/H ratios in alkenones. Paleoceanography **22**: 1–15. doi:10.1029/2007PA001468

Pakulski, J. D., R. B. Coffin, C. A. Kelley, S. L. Holder, R. Downer, P. Aas, M. M. Lyons, and W. H. Jeffrey. 1996. Iron stimulation of Antarctic bacteria. Nature **383**: 133–134.

Palenik, B., J. Grimwood, A. Aerts, and others. 2007. The tiny eukaryote *Ostreococcus* provides genomic insights into the paradox of plankton speciation. Proc. Natl. Acad. Sci. U.S.A. **104**: 7705–7710. doi:10.1073/pnas.0611046104

Panzeca, C., A. J. Beck, K. Leblanc, G. T. Taylor, D. A. Hutchins, and S. A. Sañudo-Wilhelmy. 2008. Potential cobalt limitation of vitamin B_{12} synthesis in the North Atlantic Ocean. Global Biogeochem. Cycles **22**. doi:10.1029/2007GB003124

Panzeca, C., A. J. Beck, A. Tovar-Sanchez, J. Segovia-Zavala, G. T. Taylor, C. J. Gobler, and S. A. Sañudo-Wilhelmy. 2009. Distributions of dissolved vitamin B12 and Co in coastal and

open-ocean environments. Estuarine, Coastal and Shelf Science **85**: 223–230. doi:10.1016/j.ecss.2009.08.016

Parrello, D., A. Zegeye, C. Mustin, and P. Billard. 2016. Siderophore-Mediated Iron Dissolution from Nontronites Is Controlled by Mineral Cristallochemistry. Front. Microbiol. **7**. doi:10.3389/fmicb.2016.00423

Paytan, A., K. R. M. Mackey, Y. Chen, I. D. Lima, S. C. Doney, N. Mahowald, R. Labiosa, and A. F. Post. 2009. Toxicity of atmospheric aerosols on marine phytoplankton. Proc. Natl. Acad. Sci. U.S.A. **106**: 4601–4605. doi:10.1073/pnas.0811486106

Petrou, K., C. S. Hassler, M. A. Doblin, K. Shelly, V. Schoemann, R. van den Enden, S. Wright, and P. J. Ralph. 2011. Iron-limitation and high light stress on phytoplankton populations from the Australian Sub-Antarctic Zone (SAZ). Deep Sea Research Part II: Topical Studies in Oceanography **58**: 2200–2211. doi:10.1016/j.dsr2.2011.05.020

Pfeiffer, M., O. Timm, W. C. Dullo, and D. Garbe-Schönberg. 2006. Paired coral Sr/Ca and δ18O records from the Chagos Archipelago: Late twentieth century warming affects rainfall variability in the tropical Indian Ocean. Geology **34**: 1069–1072. doi:10.1130/G23162A.1

Pierrehumbert, R. T. 2000. Climate change and the tropical Pacific: The sleeping dragon wakes. Proceedings of the National Academy of Sciences **97**: 1355–1358. doi:10.1073/pnas.97.4.1355

Pinedo-González, P., N. J. Hawco, R. M. Bundy, and others. 2020. Anthropogenic Asian aerosols provide Fe to the North Pacific Ocean. Proc Natl Acad Sci USA **117**: 27862–27868. doi:10.1073/pnas.2010315117

Polissar, P. J., and K. H. Freeman. 2010. Effects of aridity and vegetation on plant-wax δD in modern lake sediments. Geochimica et Cosmochimica Acta **74**: 5785–5797. doi:10.1016/j.gca.2010.06.018

Polovina, J. J., E. Howell, D. R. Kobayashi, and M. P. Seki. 2001. The transition zone chlorophyll front, a dynamic global feature defining migration and forage habitat for marine resources. Progress in Oceanography **49**: 469–483. doi:10.1016/S0079-6611(01)00036-2

Pomeroy, L., P. leB. Williams, F. Azam, and J. Hobbie. 2007. The Microbial Loop. Oceanog. **20**: 28–33. doi:10.5670/oceanog.2007.45

Poorter, H., J. Bühler, D. van Dusschoten, J. Climent, and J. A. Postma. 2012. Pot size matters: a meta-analysis of the effects of rooting volume on plant growth. Functional Plant Biol. **39**: 839. doi:10.1071/FP12049

Popp, M., F. Larher, and P. Weigel. 1985. Osmotic adaption in Australian mangroves, p. 247–253. *In* W.G. Beeftink, J. Rozema, and A.H.L. Huiskes [eds.], Ecology of coastal vegetation. Springer Netherlands.

Price, N. M., B. A. Ahner, and F. M. M. Morel. 1994. The equatorial Pacific Ocean: Grazer-controlled phytoplankton populations in an iron-limited ecosystem1. Limnol. Oceanogr. **39**: 520–534. doi:10.4319/lo.1994.39.3.0520

Price, N. M., and F. M. M. Morel. 1990. Cadmium and cobalt substitution for zinc in a marine diatom. Nature **344**: 658–660. doi:10.1038/344658a0

Pulido-Villena, E., A.-C. Baudoux, I. Obernosterer, and others. 2014. Microbial food web dynamics in response to a Saharan dust event: results from a mesocosm study in the

oligotrophic Mediterranean Sea. Biogeosciences **11**: 5607–5619. doi:10.5194/bg-11-5607-2014

Rabinowitz, D. 1978. Mortality and Initial Propagule Size in Mangrove Seedlings in Panama. Journal of Ecology **66**: 45–51.

Raven, J. A., M. C. W. Evans, and R. E. Korb. 1999. The role of trace metals in photosynthetic electron transport in O2-evolving organisms. Photosynthesis Research **60**: 111–150. doi:10.1023/a:1006282714942

Reef, R., and C. E. Lovelock. 2015. Regulation of water balance in Mangroves. Annals of Botany **115**: 385–395. doi:10.1093/aob/mcu174

Rice, P., I. Longden, and A. Bleasby. 2000. EMBOSS: The European Molecular Biology Open Software Suite. Trends in Genetics **16**: 276–277.

Richey, J. N., and J. P. Sachs. 2016. Precipitation changes in the western tropical Pacific over the past millennium. Geology **44**: 671–674. doi:10.1130/G37822.1

Richon, C., and A. Tagliabue. 2019. Insights Into the Major Processes Driving the Global Distribution of Copper in the Ocean From a Global Model. Global Biogeochem. Cycles **33**: 1594–1610. doi:10.1029/2019GB006280

Rioux, C. R., and R. J. Kadner. 1989. Vitamin B12 transport in Escherichia coli K12 does not require the btuE gene of the btuCED operon. Molec. Gen. Genet. **217**: 301–308. doi:10.1007/BF02464897

Risi, C., S. Bony, and F. Vimeux. 2008. Influence of convective processes on the isotopic composition ($\delta^{18}O$ and δD) of precipitation and water vapor in the tropics: 2. Physical interpretation of the amount effect. Journal of Geophysical Research Atmospheres **113**: 1–12. doi:10.1029/2008JD009943

Rivelli, A. R., R. A. James, R. Munns, and A. G. Condon. 2002. Effect of salinity on water relations and growth of wheat genotypes with contrasting sodium uptake. Functional Plant Biology **29**: 1065–1074. doi:10.1071/PP01154

Roden, G. 1991. Roden 1991 Subarctic-Subtropical Transition Zone of the North Pacific.pdf. NOAA technical report 105. 105 NOAA.

Rodionov, D. A., M. S. Gelfand, J. D. Todd, A. R. J. Curson, and A. W. B. Johnston. 2006. Computational Reconstruction of Iron- and Manganese-Responsive Transcriptional Networks in a-Proteobacteria. PLoS Computational Biology **2**: 1568–1585.

Rodriguez, I. B., and T.-Y. Ho. 2015. Influence of Co and B12 on the growth and nitrogen fixation of Trichodesmium. Front. Microbiol. **6**. doi:10.3389/fmicb.2015.00623

Ronan, J. L., N. Kadi, S. A. McMahon, J. H. Naismith, L. M. Alkhalaf, and G. L. Challis. 2018. Desferrioxamine biosynthesis: diverse hydroxamate assembly by substrate-tolerant acyl transferase DesC. Phil. Trans. R. Soc. B **373**: 20170068. doi:10.1098/rstb.2017.0068

Roth, J., J. Lawrence, and T. Bobik. 1996. COBALAMIN (COENZYME B_{12}): Synthesis and Biological Significance. Annu. Rev. Microbiol. **50**: 137–181. doi:10.1146/annurev.micro.50.1.137

Rue, E. L., and K. W. Bruland. 1995. Complexation of iron(III) by natural organic ligands in the Central North Pacific as determined by a new competitive ligand equilibration/adsorptive cathodic stripping voltammetric method. Marine Chemistry **50**: 117–138. doi:10.1016/0304-4203(95)00031-L

Ruttkies, C., E. L. Schymanski, S. Wolf, J. Hollender, and S. Neumann. 2016. MetFrag relaunched: incorporating strategies beyond in silico fragmentation. J Cheminform **8**: 3. doi:10.1186/s13321-016-0115-9

Sachs, J. P., and O. E. Kawka. 2015. The influence of growth rate on 2H/1H fractionation in continuous cultures of the coccolithophorid Emiliania huxleyi and the diatom Thalassiosira pseudonana. PLoS ONE **10**: 1–27. doi:10.1371/journal.pone.0141643

Sachs, J. P., A. E. Maloney, and J. Gregersen. 2017. Effect of light on 2H/1H fractionation in lipids from continuous cultures of the diatom *Thalassiosira pseudonana*. Geochimica et Cosmochimica Acta **209**: 204–215. doi:10.1016/j.gca.2017.04.008

Sachs, J. P., A. E. Maloney, J. Gregersen, and C. Paschall. 2016. Effect of salinity on2H/1H fractionation in lipids from continuous cultures of the coccolithophorid Emiliania huxleyi. Geochimica et Cosmochimica Acta **189**: 96–109. doi:10.1016/j.gca.2016.05.041

Sachs, J. P., D. Sachse, R. H. Smittenberg, Z. Zhang, D. S. Battisti, and S. Golubic. 2009. Southward movement of the Pacific intertropical convergence zone AD 1400-1850. Nature Geoscience **2**: 519–525. doi:10.1038/ngeo554

Sachs, J. P., and V. F. Schwab. 2011. Hydrogen isotopes in dinosterol from the Chesapeake Bay estuary. Geochimica et Cosmochimica Acta **75**: 444–459. doi:10.1016/j.gca.2010.10.013

Sachs, J. P., R. Stein, A. E. Maloney, M. Wolhowe, K. Fahl, and S. Nam. 2018. An Arctic Ocean paleosalinity proxy from δ2H of palmitic acid provides evidence for deglacial Mackenzie River flood events. Quaternary Science Reviews **198**: 76–90. doi:10.1016/j.quascirev.2018.08.025

Sachse, D., I. Billault, G. J. Bowen, and others. 2012. Molecular Paleohydrology: Interpreting the Hydrogen-Isotopic Composition of Lipid Biomarkers from Photosynthesizing Organisms. Annual Review of Earth and Planetary Sciences **40**: 221–249. doi:10.1146/annurev-earth-042711-105535

Sachse, D., A. Kahmen, and G. Gleixner. 2009. Significant seasonal variation in the hydrogen isotopic composition of leaf-wax lipids for two deciduous tree ecosystems (Fagus sylvativa and Acer pseudoplatanus). Organic Geochemistry **40**: 732–742. doi:10.1016/j.orggeochem.2009.02.008

Sachse, D., J. Radke, and G. Gleixner. 2004. Hydrogen isotope ratios of recent lacustrine sedimentary n-alkanes record modern climate variability. Geochimica et Cosmochimica Acta **68**: 4877–4889. doi:10.1016/j.gca.2004.06.004

Sachse, D., and J. P. Sachs. 2008. Inverse relationship between D/H fractionation in cyanobacterial lipids and salinity in Christmas Island saline ponds. Geochimica et Cosmochimica Acta **72**: 793–806. doi:10.1016/j.gca.2007.11.022

Saito, M. A. 2021. Dissolved Cobalt and Labile Cobalt from Leg 1 (Seattle, WA to Hilo, HI) of the US GEOTRACES Pacific Meridional Transect (PMT) cruise (GP15, RR1814) on R/V Roger Revelle from September to October 2018.doi:10.26008/1912/bco-dmo.818383.2

Saito, M. A., and J. W. Moffett. 2001. Complexation of cobalt by natural organic ligands in the Sargasso Sea as determined by a new high-sensitivity electrochemical cobalt speciation method suitable for open ocean work. Marine Chemistry **75**: 49–68. doi:10.1016/S0304-4203(01)00025-1

Saito, M. A., J. W. Moffett, S. W. Chisholm, and J. B. Waterbury. 2002. Cobalt limitation and uptake in *Prochlorococcus*. Limnol. Oceanogr. **47**: 1629–1636. doi:10.4319/lo.2002.47.6.1629

Saito, M. A., J. W. Moffett, and G. R. DiTullio. 2004. Cobalt and nickel in the Peru upwelling region: A major flux of labile cobalt utilized as a micronutrient. Global Biogeochem. Cycles **18**. doi:10.1029/2003GB002216

Saito, M. A., G. Rocap, and J. W. Moffett. 2005. Production of cobalt binding ligands in a *Synechococcus* feature at the Costa Rica upwelling dome. Limnol. Oceanogr. **50**: 279–290. doi:10.4319/lo.2005.50.1.0279

Sandy, M., and A. Butler. 2009. Microbial Iron Acquisition: Marine and Terrestrial Siderophores. Chem. Rev. **109**: 4580–4595. doi:10.1021/cr9002787

Santini, N. S., R. Reef, D. A. Lockington, and C. E. Lovelock. 2015. The use of fresh and saline water sources by the mangrove *Avicennia marina*. Hydrobiologia **745**: 59–68. doi:10.1007/s10750-014-2091-2

Satinsky, B. M., S. M. Gifford, B. C. Crump, and M. A. Moran. 2013. Use of Internal Standards for Quantitative Metatranscriptome and Metagenome Analysis, p. 237–250. *In* Methods in Enzymology. Elsevier.

Sauer, P. E., T. I. Eglinton, J. M. Hayes, A. Schimmelmann, and A. L. Sessions. 2001. Compound-specific D/H ratios of lipid biomarkers from sediments as a proxy for environmental and climatic conditions. Geochimica et Cosmochimica Acta **65**: 213–222. doi:10.1016/S0016-7037(00)00520-2

Schalk, I. J., and L. Guillon. 2013. Fate of ferrisiderophores after import across bacterial outer membranes: different iron release strategies are observed in the cytoplasm or periplasm depending on the siderophore pathways. Amino Acids **44**: 1267–1277. doi:10.1007/s00726-013-1468-2

Schefuß, E., S. Schouten, and R. R. Schneider. 2005. Climatic controls on central African hydrology during the past 20,000 years. Nature **437**: 1003–1006. doi:10.1038/nature03945

Schmidt, H.-L., R. A. Werner, and W. Eisenreich. 2003. Systematics of 2H patterns in natural compounds and its importance for the elucidation of biosynthetic pathways. Phytochemistry Reviews **2**: 61–85. doi:10.1023/B:PHYT.0000004185.92648.ae

Schneider, Z., and A. Stroiński. 1987. Chemistry of Cobalamin and Related Compounds, p. 17–92. *In* Comprehensive B12: Chemistry, Biochemistry, Nutrition, Ecology, Medicine. DE GRUYTER.

Schouten, S., J. Ossebaar, K. Schreiber, M. V. M. Kienhuis, G. Langer, A. Benthien, and J. Bijma. 2006. The effect of temperature, salinity and growth rate on the stable hydrogen isotopic composition of long chain alkenones produced by *Emiliania huxleyi* and *Gephyrocapsa oceanica*. Biogeosciences **3**: 113–119. doi:10.5194/bg-3-113-2006

Sekerci, Y., and S. Petrovskii. 2015. Mathematical Modelling of Plankton–Oxygen Dynamics Under the Climate Change. Bull Math Biol **77**: 2325–2353. doi:10.1007/s11538-015-0126-0

Shaked, Y., K. N. Buck, T. Mellett, and Maria. T. Maldonado. 2020. Insights into the bioavailability of oceanic dissolved Fe from phytoplankton uptake kinetics. ISME J **14**: 1182–1193. doi:10.1038/s41396-020-0597-3

Shaked, Y., and H. Lis. 2012. Disassembling Iron Availability to Phytoplankton. Front. Microbio. **3**. doi:10.3389/fmicb.2012.00123

Shaked, Y., B. S. Twining, A. Tagliabue, and M. T. Maldonado. 2021. Probing the Bioavailability of Dissolved Iron to Marine Eukaryotic Phytoplankton Using In Situ Single Cell Iron Quotas. Global Biogeochemical Cycles **35**. doi:10.1029/2021GB006979

Shelton, A. N., E. C. Seth, K. C. Mok, A. W. Han, S. N. Jackson, D. R. Haft, and M. E. Taga. 2019. Uneven distribution of cobamide biosynthesis and dependence in bacteria predicted by comparative genomics. ISME J **13**: 789–804. doi:10.1038/s41396-018-0304-9

Shultis, D. D., M. D. Purdy, C. N. Banchs, and M. C. Wiener. 2006. Outer Membrane Active Transport: Structure of the BtuB:TonB Complex. Science **312**: 1396–1399. doi:10.1126/science.1127694

Siegel, D. A., K. O. Buesseler, S. C. Doney, S. F. Sailley, M. J. Behrenfeld, and P. W. Boyd. 2014. Global assessment of ocean carbon export by combining satellite observations and food-web models. Global Biogeochem. Cycles **28**: 181–196. doi:10.1002/2013GB004743

Smith, F. A., and K. H. Freeman. 2006. Influence of physiology and climate on δD of leaf wax n-alkanes from C3 and C4 grasses. Geochimica et Cosmochimica Acta **70**: 1172–1187. doi:10.1016/j.gca.2005.11.006

Smith, T. J. 1987. Seed Predation in Relation to Tree Dominance and Distribution in Mangrove Forests. Ecology **68**: 266–273. doi:10.2307/1939257

Smittenberg, R. H., C. Saenger, M. N. Dawson, and J. P. Sachs. 2011. Compound-specific D/H ratios of the marine lakes of Palau as proxies for West Pacific Warm Pool hydrologic variability. Quaternary Science Reviews **30**: 921–933. doi:10.1016/j.quascirev.2011.01.012

Sobrado, M. A. 1999. Leaf photosynthesis of the mangrove Avicennia germinans as affected by NaCl. Photosynthetica **36**: 547–555. doi:10.1023/A:1007092004582

Sobrado, M. A. 2000. Relation of water transport to leaf gas exchange properties in three mangrove species. Trees **14**: 258–262. doi:10.1007/s004680050011

Song, X., M. M. Barbour, G. D. Farquhar, D. R. Vann, and B. R. Helliker. 2013. Transpiration rate relates to within- and across-species variations in effective path length in a leaf water model of oxygen isotope enrichment: Transpiration-related variation in Péclet path length. Plant Cell Environ **36**: 1338–1351. doi:10.1111/pce.12063

Stamatakis, A. 2014. RAxML version 8: a tool for phylogenetic analysis and post-analysis of large phylogenies. Bioinformatics **30**: 1312–1313. doi:10.1093/bioinformatics/btu033

Steppe, K., M. W. Vandegehuchte, B. A. E. Van de Wal, P. Hoste, A. Guyot, C. E. Lovelock, and D. A. Lockington. 2018. Direct uptake of canopy rainwater causes turgor-driven growth spurts in the mangrove *Avicennia marina*. Tree Physiology 1–13. doi:10.1093/treephys/tpy024

Sternberg, L. D. S. L., and P. K. Swart. 1987. Utilization of Freshwater and Ocean Water by Coastal Plants of Southern Florida. Ecology **68**: 1898–1905.

Suffridge, C., L. Cutter, and S. A. Sañudo-Wilhelmy. 2017. A New Analytical Method for Direct Measurement of Particulate and Dissolved B-vitamins and Their Congeners in Seawater. Front. Mar. Sci. **4**. doi:10.3389/fmars.2017.00011

Sumner, L. W., A. Amberg, D. Barrett, and others. 2007. Proposed minimum reporting standards for chemical analysis: Chemical Analysis Working Group (CAWG) Metabolomics Standards Initiative (MSI). Metabolomics **3**: 211–221. doi:10.1007/s11306-007-0082-2

Sun, Q., C. Miao, Q. Duan, H. Ashouri, S. Sorooshian, and K.-L. Hsu. 2017. A review of global precipitation datasets: data sources, estimation, and intercomparisons. Reviews of Geophysics 79–107. doi:10.1002/2017RG000574

Sunda, W. G. 1989. Trace Metal Interactions with Marine Phytoplankton. Biological Oceanography **6**: 411–442. doi:10.1080/01965581.1988.10749543

Sunda, W. G., and S. A. Huntsman. 1995. Cobalt and zinc interreplacement in marine phytoplankton: Biological and geochemical implications. Limnol. Oceanogr. **40**: 1404–1417. doi:10.4319/lo.1995.40.8.1404

Sutak, R., J.-M. Camadro, and E. Lesuisse. 2020. Iron Uptake Mechanisms in Marine Phytoplankton. Front. Microbiol. **11**: 566691. doi:10.3389/fmicb.2020.566691

Tagliabue, A., O. Aumont, R. DeAth, and others. 2016. How well do global ocean biogeochemistry models simulate dissolved iron distributions?: GLOBAL IRON MODELS. Global Biogeochem. Cycles **30**: 149–174. doi:10.1002/2015GB005289

Tagliabue, A., A. R. Bowie, P. W. Boyd, K. N. Buck, K. S. Johnson, and M. A. Saito. 2017. The integral role of iron in ocean biogeochemistry. Nature **543**: 51–59. doi:10.1038/nature21058

Tagliabue, A., N. J. Hawco, R. M. Bundy, W. M. Landing, A. Milne, P. L. Morton, and M. A. Saito. 2018. The Role of External Inputs and Internal Cycling in Shaping the Global Ocean Cobalt Distribution: Insights From the First Cobalt Biogeochemical Model. Global Biogeochem. Cycles **32**: 594–616. doi:10.1002/2017GB005830

Tang, K., N. Jiao, K. Liu, Y. Zhang, and S. Li. 2012. Distribution and Functions of TonB-Dependent Transporters in Marine Bacteria and Environments: Implications for Dissolved Organic Matter Utilization D.L. Kirchman [ed.]. PLoS ONE **7**: e41204. doi:10.1371/journal.pone.0041204

Taylor, G. T., and C. W. Sullivan. 2008. Vitamin B $_{12}$ and cobalt cycling among diatoms and bacteria in Antarctic sea ice microbial communities. Limnol. Oceanogr. **53**: 1862–1877. doi:10.4319/lo.2008.53.5.1862

Thieken, A., and G. Winkelmann. 1992. Rhizoferrin: A complexone type siderophore of the mocorales and entomophthorales (Zygomycetes). FEMS Microbiology Letters **94**: 37–41. doi:10.1111/j.1574-6968.1992.tb05285.x

Tierney, J. E., J. M. Russell, Y. Huang, J. S. S. Damsté, E. C. Hopmans, and A. S. Cohen. 2008. Northern Hemisphere Controls on During the Past 60 , 000 Years. 252–255. doi:10.1126/science.1160485

Tipple, B. J., M. A. Berke, C. E. Doman, S. Khachaturyan, and J. R. Ehleringer. 2013. Leaf-wax n-alkanes record the plant-water environment at leaf flush. Proceedings of the National Academy of Sciences **110**: 2659–2664. doi:10.1073/pnas.1213875110

Tipple, B. J., and M. Pagani. 2013. Environmental control on eastern broadleaf forest species' leaf wax distributions and d/h ratios. Geochimica et Cosmochimica Acta **111**: 64–77. doi:10.1016/j.gca.2012.10.042

Tortell, P. D., M. T. Maldonado, J. Granger, and N. M. Price. 1999. Marine bacteria and biogeochemical cycling of iron in the oceans. FEMS Microbiology Ecology **29**: 1–11. doi:10.1111/j.1574-6941.1999.tb00593.x

Tortell, P. D., M. T. Maldonado, and N. M. Price. 1996. The role of heterotrophic bacteria in iron-limited ocean ecosystems. Nature **383**: 330–332. doi:10.1038/383330a0

Toulza, E., A. Tagliabue, S. Blain, and G. Piganeau. 2012. Analysis of the Global Ocean Sampling (GOS) Project for Trends in Iron Uptake by Surface Ocean Microbes F. Rodriguez-Valera [ed.]. PLoS ONE **7**: e30931. doi:10.1371/journal.pone.0030931

Tsednee, M., Y.-C. Huang, Y.-R. Chen, and K.-C. Yeh. 2016. Identification of metal species by ESI-MS/MS through release of free metals from the corresponding metal-ligand complexes. Sci Rep **6**: 26785. doi:10.1038/srep26785

Twining, B. S., and S. B. Baines. 2013. The Trace Metal Composition of Marine Phytoplankton. Annu. Rev. Mar. Sci. **5**: 191–215. doi:10.1146/annurev-marine-121211-172322

Van Wambeke, F., S. Bonnet, T. Moutin, P. Raimbault, G. Alarcon, and C. Guieu. 2008. Factors limiting heterotrophic bacterial production in the southern Pacific Ocean. Biogeosciences 833–845. doi:10.5194/bg-5-833-2008

Velasquez, I. B., E. Ibisanmi, E. W. Maas, P. W. Boyd, S. Nodder, and S. G. Sander. 2016. Ferrioxamine Siderophores Detected amongst Iron Binding Ligands Produced during the Remineralization of Marine Particles. Front. Mar. Sci. **3**. doi:10.3389/fmars.2016.00172

Versteegh, G. J. M., E. Schefuß, L. Dupont, F. Marret, J. S. Sinninghe Damsté, and J. H. F. Jansen. 2004. Taraxerol and Rhizophora pollen as proxies for tracking past mangrove ecosystems. Geochimica et Cosmochimica Acta **68**: 411–422. doi:10.1016/S0016-7037(03)00456-3

Villegas-Mendoza, J., R. Cajal-Medrano, and H. Maske. 2019. B12 production by marine microbial communities and *Dinoroseobacter shibae* continuous cultures under different growth and respiration rates. Aquat. Microb. Ecol. **83**: 251–262. doi:10.3354/ame01921

Vindeirinho, J. M., H. M. V. M. Soares, and E. V. Soares. 2021. Modulation of Siderophore Production by Pseudomonas fluorescens Through the Manipulation of the Culture Medium Composition. Appl Biochem Biotechnol **193**: 607–618. doi:10.1007/s12010-020-03349-z

Vink, S., E. A. Boyle, C. I. Measures, and J. Yuan. 2000. Automated high resolution determination of the trace elements iron and aluminium in the surface ocean using a towed fish coupled to flow injection analysis. Deep-Sea Research Part I: Oceanographic Research Papers **47**: 1141–1156. doi:10.1016/S0967-0637(99)00074-6

Vovides, A. G., J. Vogt, A. Kollert, U. Berger, U. Grueters, R. Peters, A. L. Lara-Domínguez, and J. López-Portillo. 2014. Morphological plasticity in mangrove trees: salinity-related changes in the allometry of *Avicennia germinans*. Trees - Structure and Function **28**: 1413–1425. doi:10.1007/s00468-014-1044-8

Vraspir, J. M., and A. Butler. 2009. Chemistry of Marine Ligands and Siderophores. Annu. Rev. Mar. Sci. **1**: 43–63. doi:10.1146/annurev.marine.010908.163712

Wagener, T., E. Pulido-Villena, and C. Guieu. 2008. Dust iron dissolution in seawater: Results from a one-year time-series in the Mediterranean Sea. Geophys. Res. Lett. **35**: L16601. doi:10.1029/2008GL034581

Waisel, Y., A. Eshel, and M. Agami. 1986. Salt balance of leaves of the mangrove Avicennia marina. Physiologia Plantarum **67**: 67–72. doi:10.1111/j.1399-3054.1986.tb01264.x

Wang, W., Z. Qiu, H. Tan, and L. Cao. 2014. Siderophore production by actinobacteria. Biometals **27**: 623–631. doi:10.1007/s10534-014-9739-2

Watts, R. E., M. Totsika, V. L. Challinor, A. N. Mabbett, G. C. Ulett, J. J. D. Voss, and M. A. Schembri. 2012. Contribution of Siderophore Systems to Growth and Urinary Tract Colonization of Asymptomatic Bacteriuria Escherichia coli. Infection and Immunity **80**: 333–344. doi:10.1128/IAI.05594-11

Weaver, R., D. Kirchman, and D. Hutchins. 2003. Utilization of iron/organic ligand complexes by marine bacterioplankton. Aquat. Microb. Ecol. **31**: 227–239. doi:10.3354/ame031227

Wei, L., D. A. Lockington, S. C. Poh, M. Gasparon, and C. E. Lovelock. 2013. Water use patterns of estuarine vegetation in a tidal creek system. Oecologia **172**: 485–494. doi:10.1007/s00442-012-2495-5

Westrich, J. R., A. M. Ebling, W. M. Landing, J. L. Joyner, K. M. Kemp, D. W. Griffin, and E. K. Lipp. 2016. Saharan dust nutrients promote *Vibrio* bloom formation in marine surface waters. Proc Natl Acad Sci USA **113**: 5964–5969. doi:10.1073/pnas.1518080113

Winton, V. H. L., G. B. Dunbar, N. A. N. Bertler, M.-A. Millet, B. Delmonte, C. B. Atkins, J. M. Chewings, and P. Andersson. 2014. The contribution of aeolian sand and dust to iron fertilization of phytoplankton blooms in southwestern Ross Sea, Antarctica: Fe-fertilization by dust in SW Ross Sea. Global Biogeochem. Cycles **28**: 423–436. doi:10.1002/2013GB004574

Witter, A. E., D. A. Hutchins, A. Butler, and G. W. Luther. 2000. Determination of conditional stability constants and kinetic constants for strong model Fe-binding ligands in seawater. Marine Chemistry **69**: 1–17. doi:10.1016/S0304-4203(99)00087-0

Wohl, E., A. Barros, N. Brunsell, and others. 2012. The hydrology of the humid tropics. Nature Climate Change **2**: 655–662. doi:10.1038/nclimate1556

Wolfe-Simon, F., D. Grzebyk, O. Schofield, and P. G. Falkowski. 2005. The role and evolution of superoxide dismutases in algae. Journal of Phycology **41**: 453–465. doi:10.1111/j.1529-8817.2005.00086.x

Wolhowe, M. D., F. G. Prahl, I. Probert, and M. Maldonado. 2009. Growth phase dependent hydrogen isotopic fractionation in alkenone-producing haptophytes. Biogeosciences **6**: 1681–1694. doi:10.5194/bg-6-1681-2009

Wu, J., and G. W. Luther. 1995. Complexation of Fe(III) by natural organic ligands in the Northwest Atlantic Ocean by a competitive ligand equilibration method and a kinetic approach. Marine Chemistry **50**: 159–177. doi:doi.org/10.1016/0304-4203(95)00033-N

Yang, H., M. Pagani, D. E. G. Briggs, M. A. Equiza, R. Jagels, Q. Leng, and B. A. Lepage. 2009. Carbon and hydrogen isotope fractionation under continuous light: implications for paleoenvironmental interpretations of the High Arctic during Paleogene warming. Oecologia **160**: 461–470. doi:10.1007/s00442-009-1321-1

Yee, D., and F. M. M. Morel. 1996. In vivo substitution of zinc by cobalt in carbonic anhydrase of a marine diatom. Limnol. Oceanogr. **41**: 573–577. doi:10.4319/lo.1996.41.3.0573

Zhang, X., O. Baars, and F. M. M. Morel. 2019. Genetic, structural, and functional diversity of low and high-affinity siderophores in strains of nitrogen fixing *Azotobacter chroococcum*. Metallomics **11**: 201–212. doi:10.1039/C8MT00236C

Zhang, X., F. W. Zwiers, G. C. Hegerl, F. H. Lambert, N. P. Gillett, S. Solomon, P. A. Stott, and T. Nozawa. 2007. Detection of human influence on twentieth-century precipitation trends. Nature **448**: 461–465. doi:10.1038/nature06025

Zhang, Y., D. A. Rodionov, M. S. Gelfand, and V. N. Gladyshev. 2009a. Comparative genomic analyses of nickel, cobalt and vitamin B12 utilization. BMC Genomics **10**: 78. doi:10.1186/1471-2164-10-78

Zhang, Z., G. Leduc, and J. P. Sachs. 2014. El Niño evolution during the Holocene revealed by a biomarker rain gauge in the Galápagos Islands. Earth and Planetary Science Letters **404**: 420–434. doi:10.1016/j.epsl.2014.07.013

Zhang, Z., and J. P. Sachs. 2007. Hydrogen isotope fractionation in freshwater algae: I. Variations among lipids and species. Organic Geochemistry **38**: 582–608. doi:10.1016/j.orggeochem.2006.12.004

Zhang, Z., J. P. Sachs, and A. Marchetti. 2009b. Hydrogen isotope fractionation in freshwater and marine algae: II. Temperature and nitrogen limited growth rate effects. Organic Geochemistry **40**: 428–439. doi:10.1016/j.orggeochem.2008.11.002

Zhou, Y., K. Grice, Y. Chikaraishi, H. Stuart-Williams, G. D. Farquhar, and N. Ohkouchi. 2011. Temperature effect on leaf water deuterium enrichment and isotopic fractionation during leaf lipid biosynthesis: Results from controlled growth of C3 and C4 land plants. Phytochemistry **72**: 207–213. doi:10.1016/j.phytochem.2010.10.022

APPENDIX A: IRON INCUBATION EXPERIMENTS IN THE NORTH PACIFIC

A.1 INTRODUCTION

Iron is an essential nutrient for ocean microbes, but its concentrations are limiting for primary production in many areas of the ocean (Morel and Price 2003; Twining and Baines 2013). Both large scale iron fertilization experiments and in-situ incubations from High-Nutrient Low-Chlorophyll (HNLC) areas repeatedly suggest that iron limits phytoplankton growth and primary productivity particularly in these regions (Martin et al. 1991; de Baar 2005; Boyd et al. 2007; Bertrand et al. 2011). Most dissolved iron in the ocean is complexed to organic iron-binding ligands. These organic ligands are classified into several classes by their binding affinity to iron (Vraspir and Butler 2009; Gledhill and Buck 2012), and the strength of these ligands affects the fraction of bioavailable iron to the microbial community (Vraspir and Butler 2009). For instance, phytoplankton can access porphyrin- or saccharide-bound iron more easily than siderophore-bound iron (Hutchins et al. 1999; Hassler and Schoemann 2009; Shaked and Lis 2012; Lis et al. 2015). This is because phytoplankton acquire iron primarily via the reductive iron uptake pathway rather than the siderophore uptake pathway, and generally lack specific ferrisiderophore transporters (Shaked and Lis 2012; Lis et al. 2015).

Phytoplankton have been the focus of most studies on iron bioavailability and microbial growth to date. However, primary production is closely linked to heterotrophic bacterial remineralization by a process referred to as the “microbial loop”. Heterotrophic bacteria consume about half of the organic matter produced via primary production, and compete with

phytoplankton for inorganic nutrients required for respiration and growth, and recycle organic nutrients and make them available to phytoplankton (Pomeroy et al. 2007; Herndl et al. 2008). Therefore, investigations on the effect of iron availability on microbial populations other than phytoplankton could improve our understanding on the fate of primary productivity and global carbon cycling. Although heterotrophic bacteria have high iron demands relative to phytoplankton (Tortell et al. 1996), multiple studies report contradicting results on whether they experience iron limitation. Some mesoscale iron enrichment experiments in the subarctic, equatorial and southern Pacific oceans reported there was no conclusive evidence for iron limitation of heterotrophic bacteria, but that DOC may be a co-limiting factor (Cochlan 2001; Oliver et al. 2004; Van Wambeke et al. 2008), while other experiments in the coastal Southern Ocean and the subarctic Pacific suggested that iron additions directly lead to increased bacterial production (Pakulski et al. 1996; Adly et al. 2015). There are fewer studies that look into the response of heterotrophic bacteria to iron-bound ligand additions, but incubations from the Southern Ocean, Sargasso Sea and California upwelling region suggest that ligand types are not directly related to prokaryote abundances or ligand-bound iron uptake rates, and that factors such as other limiting nutrients or community composition may be controlling the prokaryotic community responses (Weaver et al. 2003; Blanco-Ameijeiras et al. 2020). This study was designed to assess whether discrete microbial groups (photoplankton, picoeukaryotes, cyanobacteria and heterotrophic bacteria) respond differently to different forms of iron additions.

A.2 METHODS

A.2.1 Incubation setup

All containers used for the experiments were trace metal cleaned, by being soaked in 10% Citranox, 10% nitric acid and 10% hydrochloric acid for one week each, rinsed 5 times with Mili-Q and double-bagged in ziplocs in a clean room.

Iron stocks were prepared in a clean lab in 15 mL acid-cleaned polypropylene tubes. We aimed to add 1 nM of each iron treatment (or 4 nmol) to each of our incubation bottles. For the $FeCl_3$ treatment, $FeCl_3$ was dissolved in 2% nitric acid at a final concentration of 40,000 nM, and 0.1 mL of this stock solution was added. For the ferrioxamine treatment, ferrioxamine stock was prepared by initially preparing a 4,000 nM desferrioxamine B (DFB) stock in 10 mL Mili-Q, then adding 800 µL of 50 µM $^{57}Fe/^{58}Fe$ spike and leaving overnight to equilibrate, and 1 mL of this spiked solution was added. For the dust treatment, 0.84g of Arizona test dust (32,600 ppm Fe per g dust) was added to 10 mL Mili-Q and shaken by hand to make a primary dust stock of 40.01 µM, assuming a solubility of 8.2 % in Mili-Q (determined separately from a Berger leach). 1000 µL of the primary dust stock was diluted in 10 mL of Mili-Q for a final concentration of 4000 nM, and 1 mL of this secondary dust stock was added. For the particulate iron treatment, 2 liters of *in-situ* seawater from the towfish were filtered through an in-line filtration system onto 0.2 µm Supor filters. The filters were put in a -80°C freezer for 20 minutes, thawed and resuspended on 50 mL filtered seawater, which were divided into two 25 mL aliquots that were added to each replicate. All incubations started around 10 am except the particulate iron treatment, which were taken out from the incubator briefly at 1 pm to add the filtrate.

Seawater for the incubation experiments was collected at 3 different latitudes along 158°W (station S1 (24.5°N), station N1 (41.5°N) and N2 (42.3°N)) on the R/V Kilo Moana during the Gradients 3.0 cruise (April 9-30, 2019) using the towfish. Seawater at stations N1 and N2 was filtered through a 100 μm mesh nitex pre-filter before the start of incubations. Seawater was put into 10 acid-cleaned 4 L HDPE bottles in a trace metal clean van. The 10 bottles were divided into control and four treatments in duplicates and were incubated on a shipboard incubator at temperatures identical to where waters were initially collected from. On day 0, samples for chlorophyll *a*, nutrients, flow cytometry, dissolved metals and dissolved siderophores were taken directly from water collected by the towfish. On day 2, samples for chlorophyll *a*, nutrients, flow cytometry and dissolved metals were taken from each treatment bottle. On day 4, the incubation was terminated, and samples for chlorophyll *a*, nutrients, flow cytometry, dissolved metals, particulate labile metals (1 L) and dissolved siderophores were taken from each treatment bottle.

A.2.2 Sample analyses

For chlorophyll analysis, 30 mL of samples were filtered through glass fiber filters, then the filters were submerged in 90% acetone, covered with foil, put in a -20°C freezer for about 24 hours, and ran on the fluorometer. For flow cytometry analysis, 2 mL of samples were fixed with glutaraldehyde (at a final concentration of 0.25%) and flash frozen at -80°C, and later analyzed with a BD Influx cell sorter.

60 mL of water was subsampled for nutrient analysis samples into low-density polyethylene (LDPE) bottles and stored at -20°C. These samples were analyzed by the Marine Chemistry Laboratory at University of Washington for nitrate (NO_3), nitrite (NO_2), ammonium (NH_4) and

phosphate (PO_4) using protocols from UNESCO (1994). The detection limits for each analyte were 0.288 μM, 0.011 μM, 0.047 μM and 0.014 μM respectively.

60 mL of samples for dissolved metal analysis were subsampled into acid-cleaned LDPE bottles and stored in -20°C freezer. These samples were thawed, acidified to pH of ~ 2 using concentrated nitric acid in a trace metal clean laboratory, and were analyzed by the Marine Trace Element Laboratory at University of Southern California. Samples were first preconcentrated by the seaFAST-pico system (Lagerström et al. 2013), eluted in 10 % nitric acid, and analyzed on a Thermo Fisher Element 2 High Resolution ICP-MS over three days. The lowest seaFAST blanks for dissolved iron over these days varied between 0.43-0.73 nM.

2.5-5 L of water was pumped onto solid phase extraction columns for dissolved siderophore analysis. These samples were processed and analyzed in the same way described in Chapter 2 of this dissertation.

A.3 Results and Discussion

A.3.1 Overview of results

Dissolved iron concentrations at the start of the incubation were 1.2-1.4 nM (Figure A.1), but there was no direct evidence of iron limitation in any of the stations, as both chlorophyll and flow cytometry cell abundances increased in the control as well as in different Fe treatments (Figure A.2, A.3). Chlorophyll concentrations and cell abundances did not show large differences between different iron treatments. Between the stations, chlorophyll concentrations, *Synechococcus* and picoeukaryote abundances increased the most over the duration of the incubations at station S1, followed by stations N1 and N2. However, based on nutrient

measurements, it may be possible that microbial growth at stations S1 and N1 was each influenced by regenerated nitrate and potentially high ammonium (Figure A.4).

A.3.2 Cell abundances

Generally, we did not see large differences in responses of different microbial groups to each iron treatment at all stations. It may be possible that microbes were not completely relying on the newly added iron, since there was 1.2-1.4 nM of dissolved iron already available to the *in situ* community at the start of each incubation (Figure A.1; see section A.3.4). We also initially planned to add 1 nM of iron to each treatment as large scale iron fertilization experiments have suggested that high iron amendments can make large diatoms to quickly dominate the microbial community and obscure any fine-scale community responses (de Baar 2005). However, multiple studies have found that even 1 nM iron additions can enhance phytoplankton iron uptake rates, biomass and community composition (Hassler and Schoemann 2009; Bertrand et al. 2011; Petrou et al. 2011), which may affect iron uptake or the growth of smaller cells. We also noted that up to 3 nM of iron may have been added into some treatment bottles (Figure A.1; see section A.3.4), but it is unclear if there were enough excess ligands in those waters that could bind to the added iron to prevent it from precipitating or adsorbing to the bottles' inner surfaces.

Chlorophyll *a* increased most in either $FeCl_3$ treatments (stations S1 and N1) or dust and pFe treatments (station N2), and least in the ferrioxamine treatments at all stations (Figure A.2). This result generally agrees with earlier observations, which found that inorganic iron ($FeCl_3$) is the most available form of iron to phytoplankton (Morel et al. 2008), or that dust-derived iron may support phytoplankton growth (Winton et al. 2014). Iron complexed to ferrioxamines (or other

siderophores) may also be accessible to some phytoplankton, although to a much lesser degree than inorganic iron (Shaked and Lis 2012).

Bacterial abundances increased the most in ferrioxamine treatments and in one pFe treatment at station S1, or in dust treatments at station N1 and N2 (Figure A.3). While ferrioxamine B is a type of siderophore used by heterotrophic bacteria to facilitate iron uptake, its uptake may be limited to specific microbial groups, and different community composition between the subtropical gyre (station S1) and northern waters (stations N1 and N2) may have resulted in the ferrioxamine addition best stimulating bacterial growth at station S1. Meanwhile, dust deposition has been shown to stimulate heterotrophic bacterial growth in both microcosm and in-situ experiments. For instance, Westrich et al. (2016) observed a rapid increase in the Vibrio population within 24 hours of dust deposition. However, it should be noted that dust can also supply a significant amount of macronutrients (N and P), DOC or other trace metals (Pulido-Villena et al. 2014; Mahowald et al. 2018; Djaoudi et al. 2020). We did not see any strong evidence that N, P or other trace metals were supplied at particularly high concentrations in our dust treatments (Figure A.1, A.4; see sections A.3.3 and A.3.4), but we do not have measurements of DOC. As heterotrophic bacterial growth is directly related to DOC supply (Eiler et al. 2003), it may be possible that either DOC supply from dust or from neighboring microbes could have affected heterotrophic bacteria cell abundances.

Prochlorococcus abundances were initially very low at stations N1 and N2 and high at station S1, but did not change or decrease over the course of incubations (Figure A.3), which likely reflects the difficulty with sustaining *Prochlorococcus* in incubation bottles (Marín et al. 2017). *Synechococcus* abundances were slightly higher in dust and pFe treatments (stations S1 and N1) or dust at station N2 (Figure A.3). There have been contradictory reports on whether

dust additions enhance or repress *Synechococcus* growth (Paytan et al. 2009; Marañén et al. 2010; Marín et al. 2017; Marín-Beltrán et al. 2019). However, declines in *Synechococcus* populations after dust additions are usually attributed to toxic effects caused by excess supply of copper (Paytan et al. 2009; Marañén et al. 2010), and our dissolved copper data suggests that we did not add high amounts of copper to our dust treatments.

Picoeukaryotes had the most variable response to different Fe additions between stations, as their abundances showed the highest increase in $FeCl_3$ and one dust treatment at station S1, or in ferrioxamine and pFe treatments at station N1 (Figure A.3). While picoeukaryotes have been found to respond to Saharan dust additions (Giovagnetti et al. 2013), it is unclear if they can access siderophore-bound iron, as two species of prasinophytes (green algae) were found to lack ferric reductase activity, which is necessary to release iron from siderophores or other ligands by reducing iron (Sutak et al. 2020).

A.3.3 Nutrient uptake rates

Both total N (nitrate and nitrite) and NH_4 concentrations at station S1 were higher on day 4 than day 0 by 0.65-1.87 μM and 0-0.23 μM, respectively (Figure A.4). It may be possible that these are regenerated nitrogen, since waters collected at this station were not pre-filtered through a 100 μm mesh. If this was the case, cell growth observed at station S1 may have been fueled by both iron and regenerated nitrogen.

There was no regeneration of total N or NH_4 at stations N1 and N2 (where waters were pre-filtered through 100 μm meshes) (Figure A.4). Station N1 and N2 had similar nitrate concentrations at the start of the incubation (6.23 and 6.29 μM respectively), and these concentrations also agree with nutrient measurements from CTD casts (6.43 and 6.23 μM

respectively). At both stations N1 and N2, NO_3 uptake rates were slightly higher in $FeCl_3$ and dust than the two other treatments (Figure A.5). As nitrate uptake has higher iron requirements than ammonium uptake (Maldonado and Price 1999; Raven et al. 1999), and iron limitation can result in reduced nitrate uptake rates (Price et al. 1994), it may be possible that $FeCl_3$ and dust-derived iron were more efficient in alleviating iron stress of the whole community than ferrioxamine-bound or particulate iron.

Unlike nitrate, ammonium concentrations at the start of the incubation at stations N1 and N2 were very different (Figure A.4). While NH_4 concentrations at station N2 from our bottles agreed well with measurements from CTD casts (0.17 and 0.11 μM respectively), NH_4 concentration at station N1 from our bottles (5.33 μM) were not only much higher than what was measured from CTD water samples (0.17 μM) at this location, but also higher than measurements from any other stations (< 0.3 μM). As ammonium measurements from other samples from station N1 at day 2 and 4 were much lower (0-0.28 μM), it is unclear if our one nutrient sample bottle from day 0 was contaminated with ammonium, or if the water we sampled (which was ~12 hours after the CTD deployment) randomly had very high ammonium, but the excess ammonium was consumed quickly. If the latter is what happened, it may potentially explain why we observed similar increases in chlorophyll *a* between stations N1 and N2 but larger increases in small cell abundances at station N1 relative to station N2. Ammonium is generally preferred over nitrate by organisms, since nitrogen in ammonium is already reduced (Dortch 1990), but diatoms in particular have been found to prefer nitrate over ammonium even when ammonium is abundant (> 10 μM) (Glibert et al. 2016). Mesocosm experiments also suggested that diatoms and cyanobacteria biomasses were each positively correlated to nitrate and ammonium uptake rates (Glibert and Berg 2009).Therefore, if ammonium was actually more abundant at station N1 than

at station N2, it may be possible that small cell growth at S1 was further stimulated with additional ammonium supply, while phytoplankton growth was not as much influenced by high ammonium.

Similar to nitrate concentrations, phosphate concentration at station N2 (0.66 μM) agreed well with that from the CTDs (0.70 μM) but concentration at station N1 (1.35 μM) was two-fold higher than the CTD measurement (0.65 μM) (Figure A.4). While there were very little differences in phosphate uptake rates between treatments at both stations, phosphate uptake rates at station N2 were 5-6 times lower relative to rates at station N1.

A.3.4 Dissolved iron

Dissolved iron concentrations in the samples were relatively low (< 5 nM) in most samples (average concentrations 1.73 ± 0.92 nM excluding outliers), but there were 7 samples from different locations or treatments that had very high dissolved iron concentrations (5.3 to 179.0 nM) (Figure A.1). To evaluate where the contamination in these samples may have originated, we looked at dissolved nickel concentrations, as nickel is an element that is much less contamination-prone than other trace metals. Because dissolved nickel concentrations were mostly constant between all samples within each incubation experiment location, we suspect that these samples were likely contaminated with iron during sample processing or analysis rather than during sample collection. We also note that the 6 ferrioxamine treatments had 2.0 ± 1.0 nM dissolved ^{56}Fe, which was up to 2.2 nM higher than ^{56}Fe concentrations in the controls. However, as we only supplied ^{57}Fe and ^{58}Fe to the ferrioxamine treatment bottles, it is unclear how additional ^{56}Fe also got introduced to these bottles.

Excluding three instances where samples from either the start or end of the incubation experiments were potentially contaminated, dissolved iron concentrations decreased by 0.5-3.3 nM over the course of 4 days in most treatments. There were no large differences in iron uptake between each treatment, and there was often high variability between replicates (Figure A.1). Any effects of iron species on iron uptake rate may have been overwhelmed by other factors including supply of other nutrients and community composition as observed from incubations in the Sargasso Sea and California upwelling region (Weaver et al. 2003). There are also treatments in which dissolved iron concentrations at day 4 (final) are higher than those at day 0 (initial): both ferrioxamine treatments at station N1, both dust treatments at station N2 and one particulate Fe treatment at stations S1 and N1 each. It may be interesting to further investigate whether the increases in dissolved iron over time could have been directly caused by the treatments (e.g. whether a portion of the dust or particulate iron that was added at the start of the incubations was in the particulate pool but became mobilized into the dissolved phase over time by microbes).

We also calculated the bioavailability of each iron species using the bioavailability proxy ($K_{in\text{-}app}$ / S.A.) from Shaked et al. (2021) to assess whether different forms of iron were preferred as an iron source for specific microbial groups. This calculation was only applied to microbial populations measured by flow cytometry at stations N1 and N2, as we could not determine how much impact regenerated nitrate had on cell growth over the duration of the experiment at station S1 (see sections A.3.2 and A.3.3), or the exact growth rate of phytoplankton. Iron quotas of heterotrophic bacteria, cyanobacteria and picoeukaryotes were taken from Boyd et al. (2015), and cell surface areas of heterotrophic bacteria, cyanobacteria and picoeukaryotes were calculated assuming that each cell is a perfect sphere with a cell radius of 1 µm (bacteria) or 10 µm (picoeukaryotes). While the $K_{in\text{-}app}$ / S.A. values of heterotrophic bacteria were lower by an

order of magnitude than those of picoeukaryotes and *Synechococcus,* the bioavailability of each iron treatment for each microbial group had similar trends, as differences in ambient iron concentrations (or additional iron amendments) between treatments had a larger effect on the bioavailability proxy than differences in growth rate and iron quota of each microbial group (Figure A.6). Ferrioxamine treatments were found to be least bioavailable to all microbial populations generally, and the uptake rate constants ($K_{in\text{-}app}$) of ferrioxamine B by *Synechococcus* (2-9 x 10^{-13} L $cell^{-1}$ hr^{-1}) were on similar order with previous observations from Lis et al. (2015). Future experiments may benefit from exclusively using isotope-labelled iron amendments and measuring intracellular iron concentrations and iron uptake rates in order to assess out whether the microbial communities are capable of recycling iron faster when supplied with iron species that are relatively less accessible.

A.3.5 Dissolved siderophores

Multiple types of siderophores were identified from different incubation experiments or treatment bottles, with no clear patterns with latitude or treatment. This may reflect the high variability of siderophore composition or the fast turnover of siderophores, and further investigation into the timescale of siderophore production and uptake may be useful. However, there was one consistent pattern that stood out with regards to all ferrioxamine treatments.

We identified two ^{57}Fe peaks from the LC-ICP-MS traces of ^{57}Fe in all $^{57}Fe/^{58}Fe$-DFB treatments across the three incubation experiment locations. Data from the LC-ESI-MS confirmed that the first peak (0.22-0.38 nM) and the second peak (24-32 pM) each corresponded to ferrioxamine B and E (Table A.1). Ferrioxamine A and ferrioxamine D were also found from the ESI-MS data, although the concentrations of these two compounds were too low to be

quantified on the ICP-MS. We confirmed that these ferrioxamines were not included in the initial DFB salt used to make the stock solution, by running DFB salt dissolved in Milli-Q (identical to the stock solution used for the incubation experiments) and in UV-oxidized seawater on the ESI-MS and only found ferrioxamine B (> 90% in iron-free form and < 10% in iron-bound form) in these solutions. In addition, these ferrioxamines, either in iron-free or iron-bound form, were not found in most of the t = 0 samples, except at 24.5°N where ^{56}Fe-bound ferrioxamine E was identified. However, even at this location, the chances of ^{57}Fe-ferrioxamine E that we identified on Day 4 coming from the exchange of ^{57}Fe with ^{56}Fe-bound ferrioxamine E are likely low given that the timescale of metal exchange in siderophores is on the order of days to weeks (Boiteau and Repeta 2022). Instead, we suggest that the addition of ^{57}Fe/^{58}Fe-DFB may have stimulated microbial groups that are capable of synthesizing iron-free ferrioxamines, which in turn quickly complexed to available ^{57}Fe, presumably from dead cells that had taken up ^{57}Fe/^{58}Fe-DFB.

Ferrioxamine B and E are built from a combination of two smaller units, HAC (N-hydroxy-N-acetylcadaverine) and HSC (N-hydroxy-N-succinylcadaverine) (Ronan et al. 2018). The exact biosynthesis pathways of ferrioxamine A and D have not been identified so far, but given the high similarity between the chemical structures of ferrioxamines, these two compounds are likely also synthesized using structurally similar subunits or genes. Therefore, it may have been possible that microbes equipped with ferrioxamine biosynthetic gene clusters were more quickly responding to ferrioxamine additions than others that cannot produce or use ferrioxamines. It may also be interesting to evaluate whether the “new” ferrioxamines were produced from the “old” ferrioxamines in the future, as it is currently unclear what happens to siderophores once they get incorporated back into cells after chelating to iron, but if the iron-free ferrioxamines

transported back into the cytoplasm are broken down to the subunits, it could lower the metabolic cost of producing ferrioxamine molecules from scratch.

A.4 Conclusions

There were minor differences in cell abundances between different iron treatments, but all iron species tested in these experiments seemed to be accessible to some degree to each population and did not stimulate or inhibit growth of any single microbial group in particular. Measures of iron uptake rates or residence time of dissolved iron may provide more insight on whether these microbial groups are capable of recycling iron more or less efficiently depending on how much iron is accessible from their surroundings. Additional taxonomic analysis may also help to look into any small-scale changes in community composition or abundance and provide more insight on whether specific iron species can stimulate some taxonomic groups better than others.

A.5 Figures and Tables

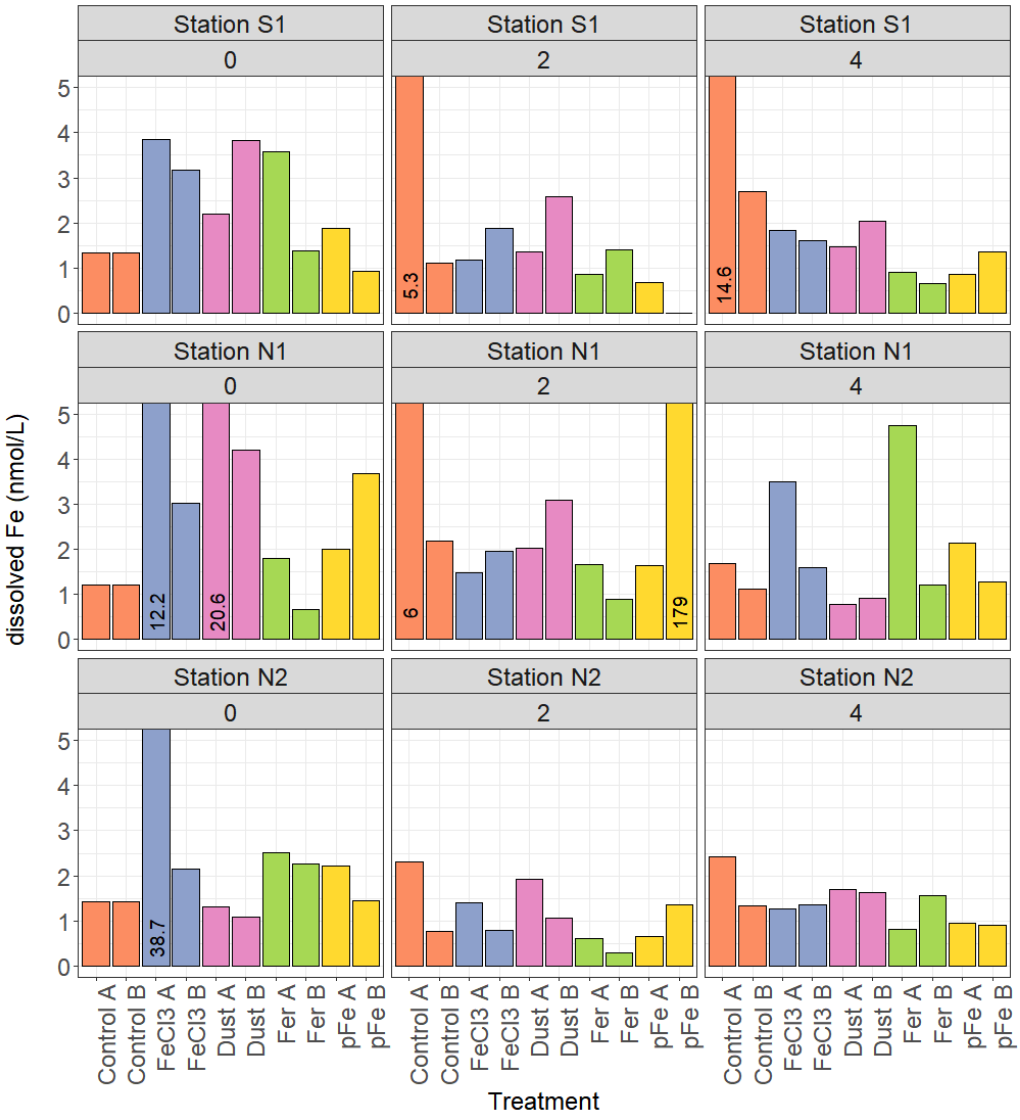

Figure A.1 Dissolved iron concentrations measured at day 0, 2, 4 from each incubation experiment. Replicates of same treatments are plotted using same colors. Numeric values of concentrations from 7 samples that exceeded 5 nM are also shown.

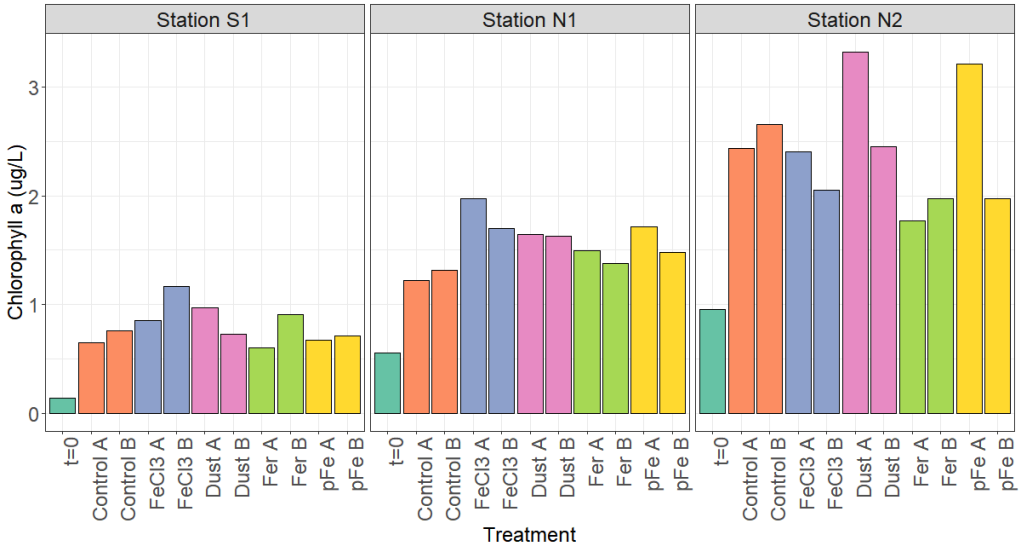

Figure A.2 Chlorophyll *a* concentrations measured at day 0 (t=0 treatment) and 4 (all other treatments) from each incubation experiment. Replicates of same treatments are plotted using same colors.

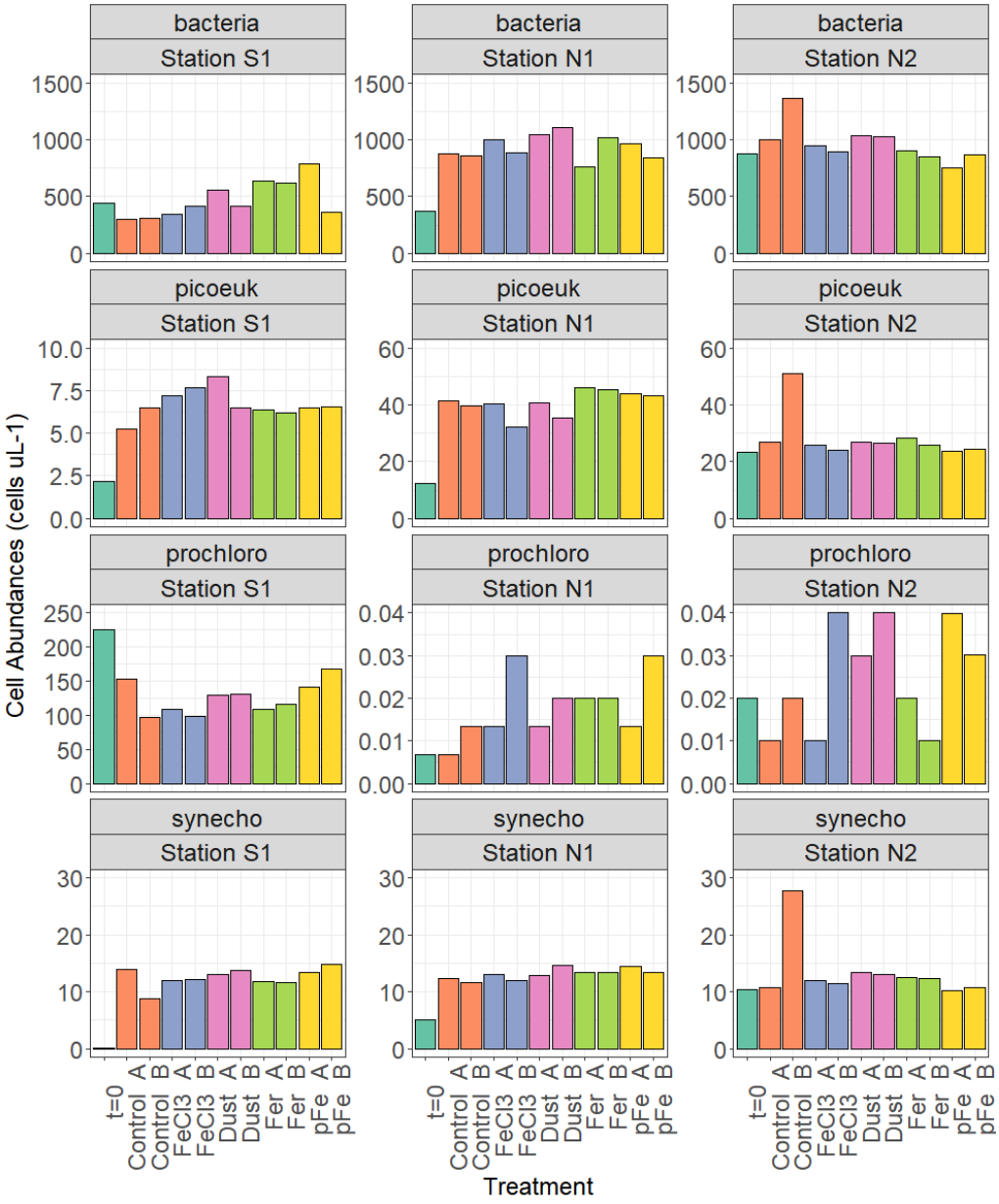

Figure A.3 Cell abundances measured by flow cytometry at day 0 (t=0 treatment) and 4 (all other treatments) from each incubation experiment. “bacteria”, “picoeuk”, “prochloro” and “synecho” each refers to heterotrophic bacteria, picoeukaryotes, *Prochlorococcus* and *Synechococcus* cell abundances. Replicates of same treatments are plotted using same colors.

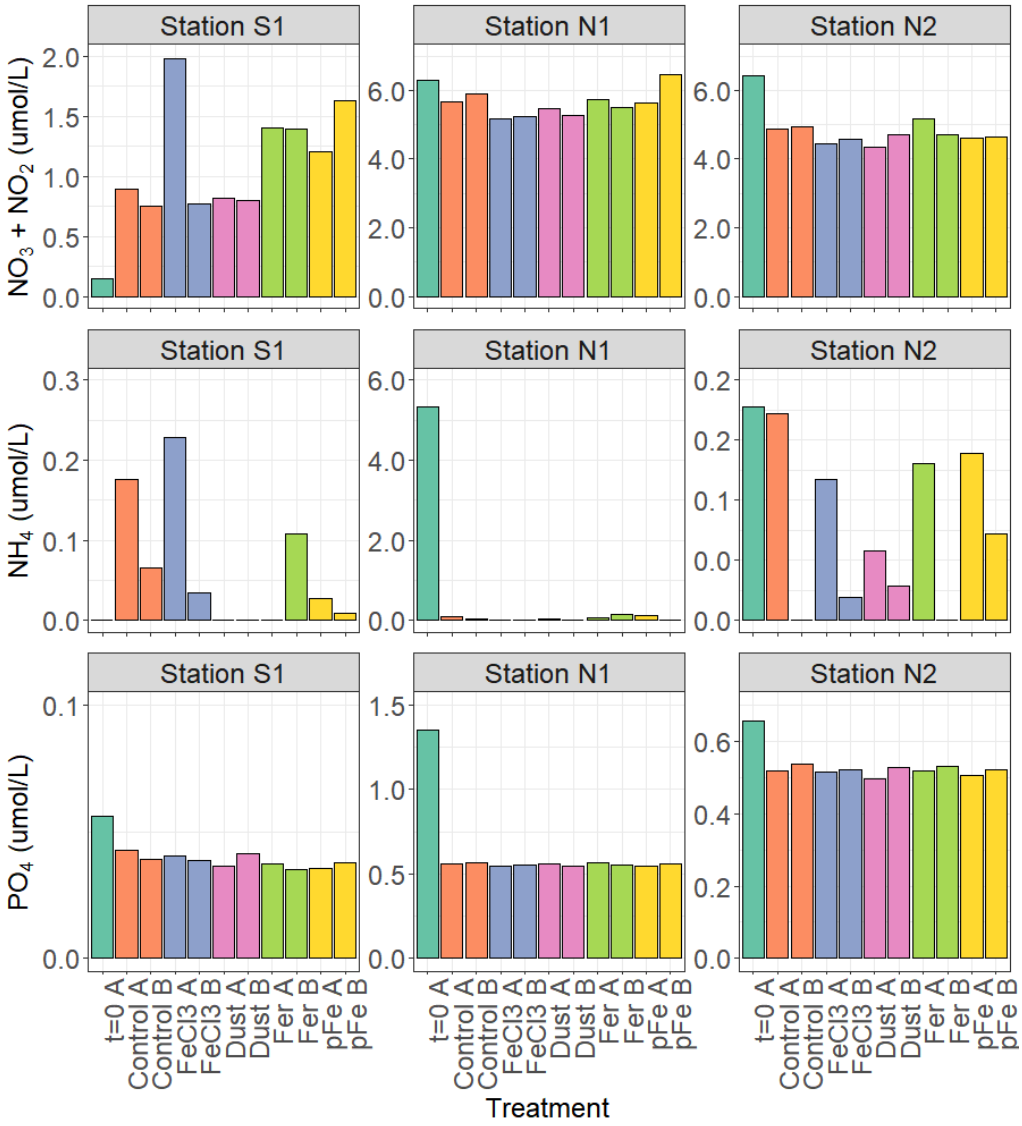

Figure A.4 Nutrient concentrations measured at day 0 (t=0 treatment) and 4 (all other treatments) from each incubation experiment. Replicates of same treatments are plotted using same colors.

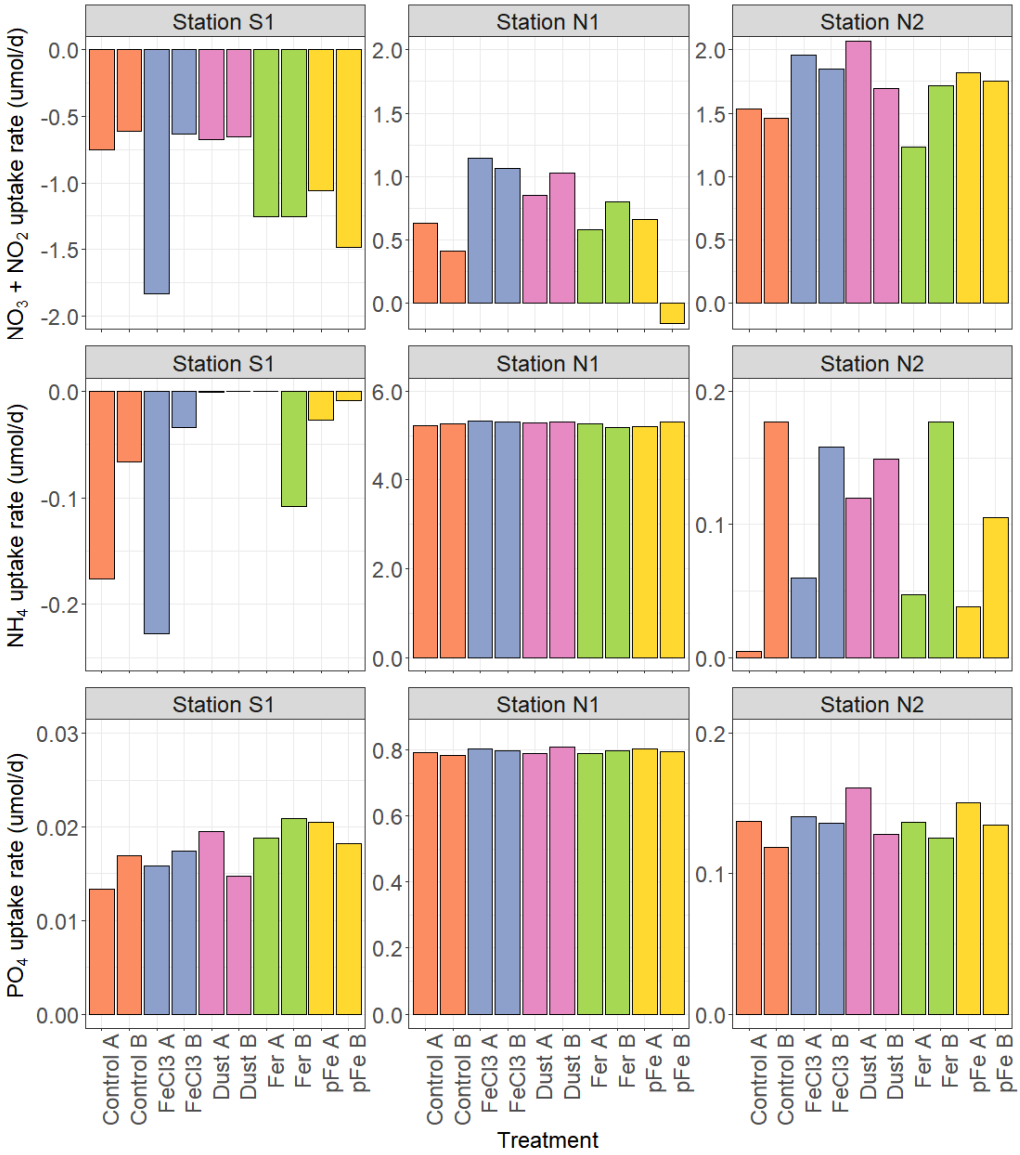

Figure A.5 Nutrient uptake rates between the start (day 0) and end (day 4) from each incubation experiment. Replicates of same treatments are plotted using same colors.

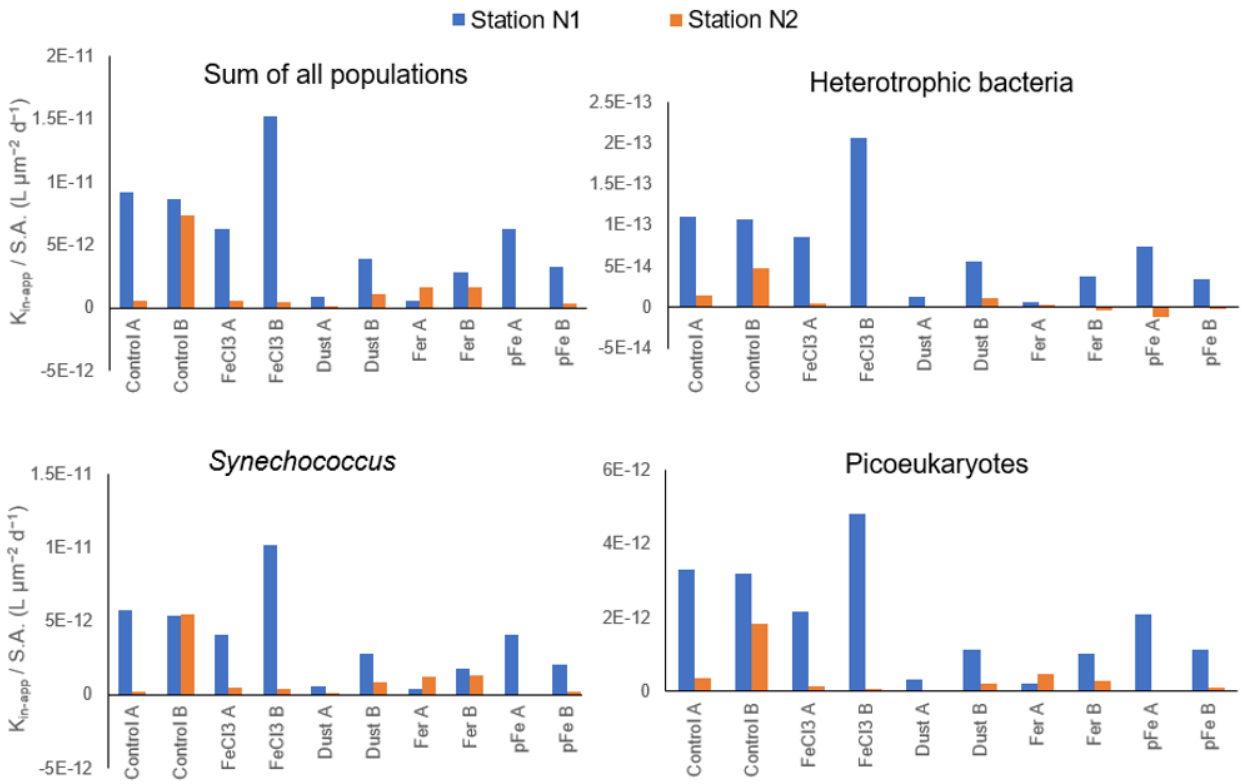

Figure A.6 Estimates of iron bioavailability proxy ($K_{in\text{-}app}$ / S.A.) for each treatment from incubations experiments at stations N1 (blue) and N2 (orange).

Table A.1 Concentrations of $^{57}Fe/^{58}Fe$-ferrioxamine B and E in ferrioxamine treatments in units of nmol/L estimated from LC-ICP-MS. Because ^{58}Fe-ferrioxamines could not be directly quantified due to isobaric interferences with ^{58}Ni, the concentrations in the table were calculated by quantifying ^{57}Fe-ferrioxamines first and multiplying those values by 2, assuming that ^{57}Fe- and ^{58}Fe-ferrioxamine concentrations are identical.

Station	S1		N1		N2	
Replicate	A	B	A	B	A	B
Ferrioxamine B	0.221	0.380	0.377	0.354	0.345	0.328
Ferrioxamine E	0.032	0.028	0.027	0.026	0.030	0.024